

Colorless Coherent Passive Optical Network Enabled by Frequency Comb Source

Zur Erlangung des akademischen Grades eines

**DOKTORS DER INGENIEURWISSENSCHAFTEN
(Dr.-Ing.)**

von der KIT-Fakultät für
Elektrotechnik und Informationstechnik
des Karlsruher Instituts für Technologie (KIT)

angenommene

DISSERTATION

von

Md Mosaddek Hossain Adib, M.Sc.

geb. in Barishal, Bangladesh

Tag der mündlichen Prüfung:

Hauptreferent:

Korreferent:

25. September 2025

Prof. Dr.-Ing. Sebastian Randel

Prof. Roberto Gaudino

Kurzfassung

Weltweit existieren derzeit etwa 1,6 Milliarden breitbandige Festnetzanschlüsse, von denen über 90% auf dem Konzept der Passiven Optischen Netze (PON) basieren, aufgrund der Dienstgüte und Kosteneffizienz dieser Netzwerke. PONs wurden ursprünglich entwickelt, um eine effiziente und wirtschaftliche Breitbandanbindung von Haushalten mittels einer Punkt-zu-Multipunkt-Topologie (P2MP) bereitzustellen. Seither haben sich die Datenraten, angetrieben durch die gewachsenen Anforderungen seitens der Netzbetreiber sowie durch Standardisierungsbemühungen von Organisationen wie der International Telecommunication Union (ITU) und dem Institute of Electrical and Electronics Engineers (IEEE), von einigen hundert Megabit pro Sekunde auf heute mehrere zehn Gigabit pro Sekunde vervielfacht. Kürzlich hat die ITU einen 50-Gigabit-fähigen PON-Standard verabschiedet, was die Frage aufwirft, wie die nächsten Generation der PON-Technologie aussehen wird.

In Zukunft sollen PONs eine Vielzahl von Anwendungen unterstützen, von der Anbindung privater Haushalte hin zur Anbindung von Unternehmensnetzwerken und sowohl nicht-zeitkritische als auch latenzsensible Dienste umfassend. Die Bereitstellung dieses gemischten Datenverkehrs über ein einziges optisches Verteilnetz (engl. Optical Distribution Network, ODN) führt zu sehr hohen Anforderungen an das Netzwerk. Erwartete Anforderungen umfassen Datenraten zwischen 100 und 200 Gbit/s, Reichweiten von 20 bis 40 km sowie eine Leistungsübertragungsbilanz von ≥ 32 dB, um eine Anbindung von 64 oder mehr Kunden zu ermöglichen. In diesem Kontext wird der Einsatz von Inphasen- und Quadraturmodulation (IQ) und kohärenter Detektion zu einer attraktiven Option, da sie im Vergleich zur Intensitätsmodulation mit Direktempfang eine

verbesserte Empfindlichkeit am Empfänger liefert, eine digitale Kompensation der chromatischen Dispersion erlaubt und eine erhöhte Zuverlässigkeit bietet.

Es ist wichtig zu beachten, dass die Komponenten der kohärenten Technologie, die ursprünglich für Weitverkehrs- und Metro-Glasfasernetze entwickelt wurden, an die Anforderungen der optischen Zugangsnetze angepasst werden müssen. Diese Arbeit beschäftigt sich mit verschiedenen Ansätzen zur Systemvereinfachung, insbesondere durch den Einsatz unkalibrierter Laser, um die Komplexität auf der Seite der optischen Netzwerkabschlüsse (engl. Optical Network Unit, ONU) zu reduzieren. Es werden neuartige digitale Signalverarbeitungstechniken (engl. digital signal processing, DSP) vorgestellt und neue kohärente PON-Architekturen untersucht, unter Berücksichtigung von Methoden wie Zeitmultiplex, Zeit-Wellenlängen-Multiplex und Subträgermultiplex sowie unter Verwendung von Frequenzkammquellen im optischen Leitungsabschluss (engl. optical line terminal, OLT). Der Schwerpunkt der Arbeit liegt auf experimentellen Untersuchungen und Demonstrationen der Datenübertragung unter Laborbedingungen, welche es erlauben die Einsatzfähigkeit von Frequenzkammquellen im OLT und von unkalibrierten Lasern im ONU zu bewerten. Die Ergebnisse dieser Arbeit wurden in den Fachzeitschriften *Journal of Lightwave Technology*, *Optics Express* und *Journal of Optical Communications and Networking* veröffentlicht [1–3].

Kapitel I führt in das Thema der optischen Zugangsnetze ein und hebt die Einschränkungen aktueller PON-Systeme hervor, um die Relevanz dieser Arbeit zu verdeutlichen.

Kapitel II gibt einen Überblick über bestehende PON-Standards und beschreibt die zukünftigen Anforderungen und Herausforderungen. Es werden außerdem Strategien vorgestellt um bereits im Massenmarkt vorhandene Technologien an die PON-Anforderungen anzupassen und nutzbar zu machen. Weiterhin wird ein vereinfachtes Modell für kohärente PONs vorgestellt.

Kapitel III beschreibt eine farblose kohärente Zeitmultiplex-PON-Architektur (engl. time division multiplexing, TDM-PON), die eine Frequenzkammquelle

auf der OLT-Seite und kostengünstige Lasern mit verteilter Rückkopplung (engl., distributed feedback, DFB-Laser) auf der ONU-Seite ausnutzt. Da die Emissionswellenlänge von DFB-Lasern aufgrund von Fertigungstoleranzen typischerweise deutlichen Schwankungen unterworfen ist, nutzt die vorgeschlagene Architektur einen auf Quantum-Dash-Mode-Locked-Laserdioden (MLLD) basierenden Frequenzkamm im OLT. Dadurch entfällt die Notwendigkeit vollständig kalibrierter, wellenlängenstabiler Laser auf der ONU-Seite. Experimentelle Ergebnisse zeigen, dass die Laserwellenlängen im ONU in einem Bereich von ± 4 nm variieren können, ohne die Qualität der Datenübertragung signifikant zu beeinträchtigen. Es werden DSP-Techniken eingeführt, einschließlich eines Multiple-Input-Multiple-Output-(MIMO)-Entzerrers mit Maximum-Ratio-Combining, bei dem die Signale ihrem Signal-zu-Rausch-Verhältnis entsprechend gewichtet werden. In der Labordemonstration wurde eine aggregierte Datenrate von 96 Gbit/s erreicht, was die Relevanz und Realisierbarkeit des Konzepts unterstreicht.

Kapitel IV behandelt ein kohärentes Zeit- und Wellenlängenmultiplex-PON (eng. time- and wavelength-division multiplexed, TWDM-PON) mit thermisch abgestimmten DFB-Lasern in der ONU. Durch das Deinterleaving des Frequenzkamms im OLT kann die Gesamtkapazität auf 200 Gbit/s in Up- und Downstream-Richtung erhöht werden. Es wird eine Burst-Mode-DSP-Technik vorgestellt, basierend auf einer leichten Erweiterung der konventionellen kohärenten DSP-Kette. Das System toleriert Wellenlängenabweichungen des ONU-Lasers von ± 2 nm und unterstützt verschiedene Datentypen und Dienstanforderungen.

Kapitel V fasst die Ergebnisse des BMBF-geförderten Projekts KIGLIS zusammen. In diesem Projekt beschäftigten sich verschiedene Konsortialpartner mit technischen Herausforderungen in optischen Zugangsnetzen für smarte und nachhaltig konzipierte Städte. Wie in [3] beschrieben, sind insbesondere die Abschnitte zu Glasfaserinfrastruktur und subträgerbasierten kohärenten PONs für diese Arbeit von Relevanz. Erstmals wird ein skalierbares kohärentes PON demonstriert, das Zeit-, Wellenlängen- und Subträgermultiplex kombiniert, um Flexibilität in drei Domänen zu erreichen. In einem experimentellen Aufbau wird ein 200 Gbit/s-PON mit zwei Wellenlängenkanälen gezeigt, jeweils mit acht

digitalen Subträgern bei je 12,5 Gbit/s. Dieses Konzept ermöglicht eine flexible Datenratenzuweisung und unterstützt sowohl virtuelle Punkt-zu-Punkt- (PTP) als auch P2MP für konvergente Dienste unter Nutzung der Subträgergranularität.

Abschließend gibt *Kapitel VI* eine Zusammenfassung der Arbeit und einen Ausblick auf zukünftige kohärente PON-Systeme.

Globally, there are currently 1.6 billion fixed broadband subscribers, with over 90% utilizing passive optical network (PON) technology due to its quality of service and cost-effectiveness. PONs were initially designed to provide efficient and economical broadband connectivity to residential customers using a point-to-multipoint (P2MP) topology. Since then, the PON's peak data rates have evolved from a few hundred megabits to tens of gigabits today, an evolution driven by the growing demands from network operators and documented by the standardization efforts in various organizations such as the International Telecommunication Union (ITU) and the Institute of Electrical and Electronics Engineers (IEEE). Recently, the ITU standardized a 50-gigabit-capable PON, raising questions about requirements and technology options for next-generation PON.

Future PONs are expected to support a wide range of applications ranging from residential to enterprise networks, and from non-time-sensitive to latency-critical services. Transmission of mixed data traffic from diverse applications over a single optical distribution network (ODN) presents significant challenges to the next-generation PON design, which must meet high data rates, low-latency, and reduced power consumption. Anticipated requirements include service rates of 100 to 200 Gbit/s, support for maximum distances between 20 and 40 km, and ODN loss budgets of ≥ 32 dB to accommodate split ratios of 1:64 or more. As a result, in-phase and quadrature (IQ) modulation with coherent detection becomes an attractive solution due to its superior receiver sensitivity, digital chromatic dispersion compensation capability, and flexibility compared with intensity modulation and direct detection.

It is important to note that coherent technologies, originally developed for long-haul and metro optical networks, therefore require PON-specific adaptation to achieve successful implementation in access networks. This thesis addresses various system simplification strategies to reduce complexity on the optical network unit (ONU) side, in particular the use of an uncalibrated laser. It presents novel digital signal processing (DSP) techniques and explores new coherent PON

transceiver architectures using frequency comb lasers in the optical line terminal (OLT), including time-division multiplexing (TDM), time and wavelength-division multiplexing (TWDM), as well as time, wavelength and subcarrier-based frequency-division multiplexing (TWFDm). The focus is on lab-based data transmission experiments that investigate the feasibility of comb sources in the OLT and uncalibrated lasers in the ONU. The outcomes of this work have been published in the *Journal of Lightwave Technology*, *Optics Express*, and the *Journal of Optical Communications and Networking* [1–3].

Chapter I introduces the general topic of optical access networks and highlights the limitations of current PON systems to motivate the need for this work.

Chapter II summarizes legacy PON standards and outlines future requirements and challenges. It also reviews strategies for technology adaptation from high-volume market segments and introduces a simplified model for coherent PON.

Chapter III presents a colorless coherent time-division multiplexed PON (TDM-PON) architecture based on a frequency comb laser at the OLT and low-cost distributed feedback (DFB) lasers at the ONU. Experimental results show that ONU laser wavelengths can vary by ± 4 nm without significant performance penalties. Advanced DSP techniques are introduced, including a multiple-input multiple-output (MIMO) equalizer using maximum ratio combining and spectral stitching. The lab demonstration achieves an aggregate data rate of 96 Gbit/s, confirming the viability of the approach.

Chapter IV demonstrates a coherent time- and wavelength-division multiplexed (TWDM) PON using thermally tuned DFB lasers at the ONU. By deinterleaving the frequency comb at the OLT, the system increases the network capacity to 200 Gbit/s in both upstream and downstream directions. The study introduces burst-mode DSP using a minor extension of conventional coherent DSP chains. The system tolerates ONU wavelength variations of ± 2 nm and supports diverse traffic patterns and service requirements.

Chapter V summarizes results from the BMBF-funded project KIGLIS. In this project, various consortium partners addressed technical challenges in optical

access networks for smart and sustainable cities. As detailed in [3], the sections related to fiber-optic network technologies and subcarrier-based coherent PONs are particularly relevant to this thesis. A scalable coherent PON is demonstrated for the first time using time-, wavelength-, and subcarrier-division multiplexing to achieve flexibility across three domains: time, optical wavelength, and subcarrier. We demonstrate a 200 Gbit/s PON with two wavelength channels, each carrying eight digital subcarriers at 12.5 Gbit/s. This approach enables flexible data rate allocation and supports both virtual point-to-point (PTP) and P2MP connectivity for converged services, leveraging the granularity of digital subcarriers.

Finally, *Chapter VI* summarizes the work and provides an outlook on future directions for coherent PON systems.

Achievements of the present work

In this thesis, a novel coherent passive optical network (PON) architecture aimed at reducing complexity on the user side, along with advanced digital signal processing (DSP) schemes for both downstream and burst-mode upstream transmission, is presented. The main achievements of this work are summarized below.

First Demonstration of Colorless Coherent TDM-PON: Low-cost, uncalibrated lasers suffer from emission wavelength ambiguity, while coherent receivers require frequency-stable sources. To address this challenge, we demonstrate a colorless coherent time-division multiplexed (TDM) PON system using a frequency comb laser-based transceiver at the optical line terminal (OLT) and an uncalibrated laser-based transceiver design at the optical network unit (ONU). This approach eliminates the need for precise laser calibration. The results of this work have been published in the *Journal of Lightwave Technology* [1].

Maximum Ratio Combining and Spectrum Stitching Using MIMO Equalization: Depending on the receiver bandwidth, multiple replicas of the transmitted signal may be captured in the TDM-PON system. To take advantage of this redundancy, we introduce an advanced DSP technique based on signal tripling and maximum ratio combining using a 6×2 multiple-input multiple-output (MIMO) equalizer, increasing the receiver sensitivity by 3 dB. For limited-bandwidth receivers, we propose a spectrum stitching method using a 4×2 MIMO equalizer, which enables effective reconstruction of partial signal copies from different comb lines. This approach achieves performance comparable to that of conventional DSP. These results are also included in the previously mentioned publication [1].

First Demonstration of Burst-Mode Coherent TWDM-PON Utilizing a Frequency Comb: We demonstrate a coherent time- and wavelength-division multiplexed (TWDM) PON using a mode-locked laser diode (MLLD)-based frequency comb at the OLT and a thermally tunable distributed feedback (DFB) laser at the ONU. This system achieves a total capacity of 200 Gbit/s while accommodating ONU laser wavelength variations of ± 2 nm (± 250 GHz). Additionally, we demonstrate burst-mode upstream transmission and corresponding burst-mode DSP in this coherent TWDM-PON context. The results of this work have been published in *Optics Express* [2].

First Demonstration of Coherent Time-, Wavelength-, and Frequency (via, Subcarrier) -Division Multiplexed PON: This thesis presents the first system architecture for a coherent PON that supports flexible resource allocation across all three possible domains: time, optical wavelength, and frequency/subcarrier. A 200 Gbit/s coherent time-, wavelength-, and subcarrier-based frequency-division multiplexed (TWFDMA) PON is demonstrated using two wavelength channels, each carrying eight digital subcarriers at 12.5 Gbit/s. This work has been published in the *Journal of Optical Communications and Networking* [3].

List of Publications

Journal articles

- [1] M. M. H. Adib, C. Füllner, J. N. Kemal, P. Marin-Palomo, A. Ramdane, C. Koos, W. Freude, and S. Randel, “Colorless Coherent TDM-PON Based on a Frequency-Comb Laser,” *J. Lightwave Technol.*, vol. 40, no. 13, pp. 4287–4299, Jul 2022.
- [2] M. M. H. Adib, C. Füllner, H. Peng, C. Koos, W. Freude, and S. Randel, “Coherent time- and wavelength-division multiplexed point-to-multipoint optical access network using low-cost DFB lasers enabled by a frequency comb,” *Opt. Express*, vol. 32, no. 22, pp. 38 516–38 530, Oct 2024.
- [3] M. M. H. Adib, P. Matalla, C. Füllner, S. Li, E. Giacomidis, C. Raack, U. Menne, M. Straub, T. Saier, C. Schweikert, S. Orf, M. Gontscharow, T. Käfer, M. Färber, A. Richter, R. Bonk, and S. Randel, “Optical-access networks for smart sustainable cities: from network architecture to fiber deployment,” *J. Opt. Commun. Netw.*, vol. 17, no. 3, pp. 221–232, Mar 2025.
- [4] C. Füllner, M. M. H. Adib, S. Wolf, J. N. Kemal, W. Freude, C. Koos, and S. Randel, “Complexity analysis of the kramers–kronig receiver,” *Journal of Lightwave Technology*, vol. 37, no. 17, pp. 4295–4307, 2019.
- [5] T. Harter, S. Ummethala, M. Blaicher, S. Muehlbrandt, S. Wolf, M. Weber, M. M. H. Adib, J. N. Kemal, M. Merboldt, F. Boes *et al.*, “Wireless thz link with optoelectronic transmitter and receiver,” *Optica*, vol. 6, no. 8, pp. 1063–1070, 2019.

Conference contributions

- [6] M. M. H. Adib, C. Füllner, M. Straub, L. Breyne, D.-v. Veen, and R. Bonk, “240 Gbit/s Bidirectional Coherent PON Using Uncalibrated ONU Lasers and Blind Coarse Alignment,” in *European Conference on Optical Communication (ECOC)*, 2025, paper accepted.
- [7] M. M. H. Adib, C. Füllner, S. Das, M. Straub, L. Breyne, D.-v. Veen, and R. Bonk, “224 Gbit/s Coherent PON Downstream Using a Wavelength-Uncalibrated LO and Blind Locking During ONU Startup,” in *Optical Fiber Communication Conference (OFC)*, 2025, paper Tu2I.6.
- [8] M. M. H. Adib, C. Fuellner, V. Houtsma, D. v. Veen, R. Bonk, and J. Maes, “Challenges to overcome for coherent systems to enter the TDM-PON market,” in *IEEE Photonics Society Summer Topicals Meeting Series*, 2025, paper ME2.1.
- [9] S. Das, M. M. H. Adib, M. Straub, and R. Bonk, “TDM-PON Supporting IEEE-802.11CB Based Deterministic Networking for Reliability in Industrial TSN Networks,” in *Advanced Photonics Congress (APC)*, 2025, paper NeM4C.3.
- [10] C. Füllner, V. Houtsma, M. M. H. Adib, and J. Maes, “Towards 100G and 200G PON – Has the Time for Coherent Come?” in *Advanced Photonics Congress (APC)*, 2025, paper SpW2F.2.
- [11] J. Maes, C. Füllner, M. M. H. Adib, and V. Houtsma, “The Road Towards 100G 200G Passive Optical Network,” in *International Conference on Transparent Optical Networks (ICTON)*, 2025, paper Mo.C3.2.
- [12] V. Houtsma, D. Van-Veen, R. Borkowski, K. Vijayan, C. Füllner, M. M. H. Adib, and J. Maes, “Next Generation Very High-Speed PONs which Loss Budgets Can be Supported by IM-DD and Coherent,” in *OptoElectronics and Communications Conference (OECC)*, 2025, paper MB1-1.

- [13] M. M. H. Adib, “Reality check for coherent PON: The elephant race between single-carrier and multi-carrier,” in *Optical Fiber Communication Conference (OFC)*, 2024, workshop: Coherent Optics for Next Generation 100G/200G PON: Single-Carrier or Multi-Carrier?
- [14] M. M. H. Adib, C. Fuellner, and R. Bonk, “Power budget analysis of 200 Gbit/s coherent PON downstream taking into account OLT requirements and ONT simplifications,” in *European Conference on Optical Communication (ECOC)*, 2024, pp. 124–127.
- [15] M. M. H. Adib, C. Füllner, and S. Randel, “Coherent PON technologies for 100G PON and beyond,” in *Photonics Days Berlin-Brandenburg*, 2022, session on Smart Photonic Technologies and Networks for Smart Cities.
- [16] M. M. H. Adib, C. Füllner, C. Koos, W. Freude, and S. Randel, “Subcarrier-Based Coherent PON Architecture for a Converged Fiber Infrastructure in Smart Cities,” in *Advanced Photonics Congress (APC)-Photonic Networks and Devices*, 2022, paper NeM3D.2.
- [17] M. M. H. Adib, C. Füllner, and S. Randel, “Comparison of Coarse Frequency-Offset Estimation Algorithms for Coherent Passive Optical Networks,” in *Photonic Networks; 22th ITG Symposium*, 2021.
- [18] M. M. H. Adib, C. Füllner, A. Schwarzenberger, C. Koos, W. Freude, and S. Randel, “Analysis of Burst Mode Reception in 100 Gbit/s Coherent Passive Optical Networks,” in *Advanced Photonics Congress (APC)-Photonic Networks and Devices*, 2021, paper NeM1C.3.
- [19] M. Mahmud, J. Kemal, M. Adib, C. Füllner, A. Schindler, P. Runge, M. Schell, W. Freude, C. Koos, and S. Randel, “Optic-electronic-optic interferometer: A first experimental demonstration,” in *Conference on Lasers and Electro-Optics (CLEO)*, 2020, paper SF1L.1.
- [20] M. M. H. Adib, P. Marin-Palomo, J. N. Kemal, C. Füllner, S. Mahmud, A. Ramdane, C. Koos, W. Freude, and S. Randel, “Coherent TWDM-PON

downstream architecture based on a chip-scale QD-MLLD,” in *Advanced Photonics Congress (APC)-Photonic Networks and Devices*, 2020, paper NeTu2B.5.

- [21] M. M. H. Adib, J. N. Kemal, C. Füllner, M. S. Mahmud, A. Ramdane, C. Koos, W. Freude, and S. Randel, “Colorless coherent passive optical network using a frequency comb local oscillator,” in *Optical Fiber Communication Conference (OFC)*, March 2019, paper Th3F.4.
- [22] M. M. H. Adib, M. S. Mahmud, J. N. Kemal, P. Marin-Palomo, C. Füllner, A. Ramdane, C. Koos, W. Freude, and S. Randel, “24 GBd DP-QPSK upstream and downstream operation of a colourless coherent PON using an MLLD-based frequency comb,” in *European Conference on Optical Communication (ECOC)*, September 2019, paper M1F.2.
- [23] M. M. H. Adib, D. Pileri, C. Füllner, W. Freude, C. Koos, and S. Randel, “Optical Filter Requirements for DWDM Transmission Systems with Kramers-Kronig Receivers,” in *European Conference on Optical Communication (ECOC)*, 2018, paper We2.34.
- [24] M. M. H. Adib, C. Füllner, W. Freude, C. Koos, and S. Randel, “Colorless Coherent TWDM-PON Architecture Based on a Frequency-Comb Local Oscillator,” in *Bell Labs Student Day, Stuttgart, Germany*, 2018.
- [25] T. Harter, M. M. H. Adib, S. Wolf, S. Muehlbrandt, M. Weber, M. Blaicher, F. Boes, H. Massler, A. Tessmann, S. Nellen *et al.*, “Wireless multi-subcarrier thz communications using mixing in a photoconductor for coherent reception,” in *IEEE Photonics Conference (IPC)*, 2017, paper 147–148.
- [26] M. I. Khalil, M. M. H. Adib, A. M. Chowdhury, M. S. Faruk, and G.-K. Chang, “Least radial distance based carrier phase recovery for 16-qam coherent optical systems,” in *OptoElectronics and Communications Conference (OECC)*, 2013, paper TuPR.14.

- [27] M. M. H. Adib, M. I. Khalil, A. M. Chowdhury, and G.-K. Chang, “Non-decision aided lms algorithm for joint blind equalization and carrier phase estimation in optical coherent receiver,” in *Conference on Lasers and Electro-Optics (CLEO)*, 2013, paper JTu4A.95.
- [28] M. M. H. Adib, T. U. Mullick, M. I. Khalil, A. M. Chowdhury, G.-K. Chang, and N. Amin, “Optical absorption enhancement in slanted micro-hole c-si for photovoltaic applications,” in *Asia Communications and Photonics Conference (ACP)*, 2012, paper ATh2F.3.

Contents

Kurzfassung	i
Preface	v
Achievements of the present work	ix
List of Publications	xi
Journal articles	xi
Conference contributions	xii
1 Introduction	1
2 Fundamentals on Optical Access Network	5
2.1 Communication System	5
2.1.1 Passive Optical Networks	6
2.1.2 Legacy PONs	7
2.1.3 Very-High-Speed PON and challenges	10
2.1.4 Technology Adaption in PON	12
2.1.5 PON Coexistence	13
2.2 Coherent PON: IQ-modulation and coherent detection	16
2.2.1 Laser Sources	16
2.2.2 Coherent PON Downstream	20
2.2.3 Coherent PON Upstream	23
3 Colorless Coherent TDM-PON	27
3.1 Introduction	29
3.2 Colorless Coherent TDM-PON Architecture	31

3.3	Theoretical System Model	32
3.3.1	Colorless Coherent Downstream	33
3.3.2	Colorless Coherent Upstream	35
3.4	DSP for Colorless Coherent Reception	38
3.4.1	DSP Scheme-I (with 2×2 MIMO)	42
3.4.2	DSP Scheme-II (with 6×2 MIMO)	43
3.4.3	DSP Scheme-III (with 4×2 MIMO)	44
3.5	Experimental Setups	45
3.6	Experimental Results	50
3.6.1	Downstream Colorless Coherent PON	50
3.6.2	Upstream Colorless Coherent PON	55
3.7	Summary	58
4	Coherent TWDM-PON	61
4.1	Introduction	62
4.2	Coherent TWDM-PON using a frequency comb source as OLT laser	65
4.2.1	Coherent TWDM-PON architecture	65
4.2.2	Solution to the wavelength-alignment challenge	67
4.3	Experimental setups and results	69
4.3.1	Frequency comb source	69
4.3.2	Downstream experiments with two groups of comb lines	70
4.3.3	Upstream operation with a frequenting comb source as an LO	75
4.4	Summary	82
5	Subcarrier Based Coherent PON for Smart Sustainable City	85
5.1	Introduction	87
5.2	Vision of a Smart Sustainable City	89
5.3	Fiber-Optic Network Technologies	91
5.3.1	Passive Optical Networks	91
5.3.2	IM/DD 100 Gbit/s PON	92

5.3.3	200 Gbit/s Coherent Subcarrier PON	97
5.3.4	Dense Network Monitoring	109
5.4	Network Resource Allocation	110
5.5	Fiber Network Deployment	113
5.6	Remote Assistance	120
5.7	Conclusion	122
6	Summary	125
6.1	Summary	125
6.2	Outlook	127
	Acronyms and symbols	129
	Bibliography	137

1 Introduction

Over the past few decades, society and governance have undergone unprecedented transformations due to the widespread adoption of digital communication and computational technologies. This transformation has been possible because modern societies have a tendency of accepting and adopting new technologies in various aspects of life, including mobility, manufacturing, social organization, security, law, education, and healthcare. Therefore, digital technologies have been addressing existing challenges and creating new opportunities across all sectors. Note that these paradigm shifts have been made possible primarily through continuous advancements in different sectors, in particular communication technology and more specifically optical communication, as well as in integrated-circuit and computing technologies. Currently, we are witnessing a new paradigm shift driven by the widespread adaption of artificial intelligence (AI) into nearly every aspect of modern life. This development has been enabled by recent breakthroughs in generative AI, powered by transformer models [29]. Over the last century, we have seen a few major societal transformations driven by the industrial revolution and, more recently, by the digital revolution. Looking ahead, it is foreseeable that the advancement of AI will continue throughout this decade and into the coming decades and may define a new era of AI-driven society. It is important to notice that the core of the digital infrastructure as well as the new AI services is optical fiber communication. As digital and AI-driven technologies continue to scale, data traffic will significantly increase not only within data centers, where most computation and logical analysis occurs, but also across the core, metro, and access networks [30]. Each of these network segments has its own unique technical challenges and requirements, defined by diverse service demands, reliability expectations, and cost structures [31]. This

thesis focuses specifically on the physical layer challenges in future optical access networks, with particular emphasis on point-to-multipoint (P2MP) topologies based passive optical networks (PONs).

PONs are inherently end-user-centric and were initially developed to provide broadband connectivity to residential users [32, 33]. Traditional PONs employ intensity modulation and direct detection (IM-DD) [34–50] and typically support data rates ranging from a few gigabit to tens of gigabits [51, 52]. As mentioned in the previous paragraph, to cope with next-generation service requirements, PONs might need to support data rates beyond hundreds of gigabits [52–54]. Furthermore, future PONs will require flexible and granular bandwidth allocation while also supporting converged services which aggregate residential, business, enterprise, and mobile transport onto a common fiber infrastructure [55–57]. Therefore, the exploration of new technologies, including higher-order modulation formats and coherent detection, is important for the evolution of PONs [58]. It is worth noting that coherent optical systems are not new; they have evolved over the past three decades and have been primarily optimized for long-distance communication, where performance is the primary concern [31]. In contrast, PONs serve the last-mile segment, where cost efficiency and system simplicity are the main concerns [59]. Moreover, PONs operate as shared media networks. In the downstream, PON employs a point-to-multipoint topology with time-division multiplexing (TDM), while in the upstream, it uses a multipoint-to-point configuration with time-division multiple access (TDMA). On the other hand, coherent technologies are primarily designed and developed for point-to-point communication [31, 59, 60]. This fundamental difference in priorities and architectural requirements introduces unique challenges for adopting coherent technologies in PONs. Therefore, reducing complexity and tailoring coherent technologies to fit the specific needs of PONs is crucial.

A coherent transceiver is composed of several subsystems. In a broader sense, it can be categorized into three groups: optical components, electrical components, and electrical-to-optical or optical-to-electrical transducer components [61, 62]. Among these, the laser is one of the most critical components in a coherent

system [63]. It requires a narrow linewidth and high frequency stability due to the inherent wavelength alignment requirement in coherent PONs [64, 65]. However, such lasers may not be well-suited for low-cost PON systems [66, 67] unless there is significant technological iteration or disruptive innovation in laser or coherent receiver design. This thesis proposes a PON architecture that employs a frequency comb source at the optical line terminal (OLT), which eliminates the need for tightly-aligned wavelength-stabilized lasers at the optical network units (ONUs). Additionally, this thesis introduces unique digital signal-processing (DSP) techniques based on maximum ratio combining to improve the receiver sensitivity and allow colorless coherent reception.

Looking forward, future PONs may need to support multiple services simultaneously due to service convergence, each with varying requirements for data rate, latency, reliability, and power consumption. Coherent reception, combined with time- and wavelength-division multiplexing (TWDM), is one possible approach to enable this type of flexibility in the access domain [68]. However, current TWDM-PON standards [69] do not support sufficiently high data rates or offer scalability to meet future demands, and they are not easily compatible with coherent systems. This thesis introduces a novel method that involves deinterleaving frequency comb lines and using them as light sources for multiple OLTs, scaling total PON capacity to beyond 100 gigabits in both upstream and downstream directions. This coherent TWDM-PON architecture is scalable and may be well-suited to meet the demands of future deployments.

As the communication industry moves toward maximizing efficiency across all domains, there is a growing demand for more flexible and granular PON systems [70]. Future networks might also require PONs capable of converging multiple services (e.g., with data rates ranging from a few gigabits to hundreds of gigabits), along with dynamic bandwidth segmentation and intelligent allocation at the physical layer to meet diverse service requirements [71, 72]. This thesis introduces a system architecture that combines TWDM with frequency-division multiple access using narrow-band subcarriers, which may offer novel flexible data rate allocation across three domains (i.e., time, subcarrier/frequency, and

optical wavelength), thereby making the PON more versatile for different use cases and enabling more sustainable network designs.

2 Fundamentals on Optical Access Network

This chapter provides fundamental information on optical access networks in general and an explanation of the need for coherent passive optical networks, to provide a clearer understanding of the experimental investigations presented in this thesis. Section 2.1 provides a introduction to optical networks, including legacy PON technologies and related strategies for adapting component technologies, and the requirements and challenges for future very-high-speed PON systems. This section also introduces the wavelength plans used in various PON standards and discusses coexistence techniques over multiple generations. In Section 2.2, we outline a simplified model of a coherent PON, focusing on dual-polarization in-phase and quadrature modulation and coherent detection using a single-line laser source.

2.1 Communication System

Modern optical communication systems comprise a range of integrated subsystems, including encoders, decoders, modulators, driver-amplifiers, transimpedance-amplifiers, lasers, photodetectors, etc. [62, 73, 74]. The optical communication networks typically carry data traffic from various sources, such as voice, internet, sensors, intelligent machines, autonomous vehicles, and smart infrastructure. This information is digitized, encapsulated with source and destination identifiers (commonly referred to as source, destination, and routing headers in a communication data frame), and multiplexed for transmission over a shared optical

channel. Each functional task is systematically managed by a dedicated transmission convergence (TC) layer within the communication protocol. As a result, modern communication systems are divided into different specialized sub-fields, including security, networking, monitoring, intelligent routing, and physical layer. Note that this thesis addresses the challenges in the optical physical layer. Furthermore, optical communication systems can be broadly categorized into three types: long-haul systems, which span several thousand kilometers; metro systems, covering distances of a few hundred kilometers; and access networks, which typically operate over shorter distances, ranging from a few kilometers to several tens of kilometers [31, 75]. More specifically, this thesis addresses the physical layer challenges of future optical access networks.

2.1.1 Passive Optical Networks

Optical access networks (OANs) typically connect end users and cover the last mile of the globally connected optical network [76, 77]. There are different types of OANs, depending on the data rate, services, and operational modes, e.g., unidirectional or bidirectional. Therefore, OANs are further classified based on their architecture into point-to-point (P2P) systems, which typically use one fiber per direction, and point-to-multipoint (P2MP) systems, which are typically bidirectional (BiDi), i.e., one fiber for both direction. Generally speaking, such P2MP-BiDi systems exploit the statistical nature of the data traffic by employing time division multiplexing, which leads to a bursty signal behavior in a multipoint-to-point (M2P) scenario [78, 79]. Therefore, typical P2MP systems improve system throughput by adopting dynamic bandwidth allocation (DBA), which offers statistical multiplexing gain [80]. In this thesis, we are primarily focusing on P2MP-based OANs. Furthermore, P2MP networks are broadly categorized into two types, depending on whether active or passive components are deployed within the optical distribution network (ODN). Active optical networks (AONs) use active components such as an outdoor switch and sometimes optical

amplifiers. In contrast, passive optical networks (PONs) are based on optical passive splitters. Thus, PONs provide cost-effective and efficient fiber connectivity via shared ODN to diverse applications and services such as homes, buildings, and small- to mid-sized enterprises. In this work, we are addressing the technical challenges for next-generation very-high-speed PON (VHSP) systems.

A generic schematic of a PON is shown in Fig. 2.1. On the left side, the optical line terminal (OLT) is depicted, typically located in the central office. Note that in a central office, a few to several hundreds of OLTs are typically co-located to minimize operational costs. Those OLTs are connected to the core network through metro and long-haul optical links as illustrated by the colored ring. On the right side, optical network units (ONUs) are located, typically providing broadband connectivity to various applications or services such as internet access, digital subscriber line (DSL), Wi-Fi, local area networks, etc. As explained in the previous paragraph, these ONUs are connected to the OLT via a passive-splitter-based ODN. The fiber distance between the OLT and the ONUs ranges from 0 to 20 km in most PONs [59, 81], which typically depends on the ODN architecture. It is important to note that the physical placement of the optical passive splitter in ODN is not specified in the PON standards, allowing flexibility in the deployment. However, the standards do define a few key physical layer parameters, such as maximum and minimum optical launch power, minimum and maximum received optical power, maximum fiber length, and the dynamic range in the ODN [44, 46, 49]. This level of abstraction allows the network operators and service providers to tailor deployment strategies according to the geography, network operation, and requirements.

2.1.2 Legacy PONs

The first generation of PON was standardized in the mid-1990s, known as asynchronous transfer mode PON (APON) [34]. APON leveraged asynchronous transfer mode (ATM) technology to serve multiple users simultaneously over an optical fiber plant. This bidirectional APON offered significant advantages

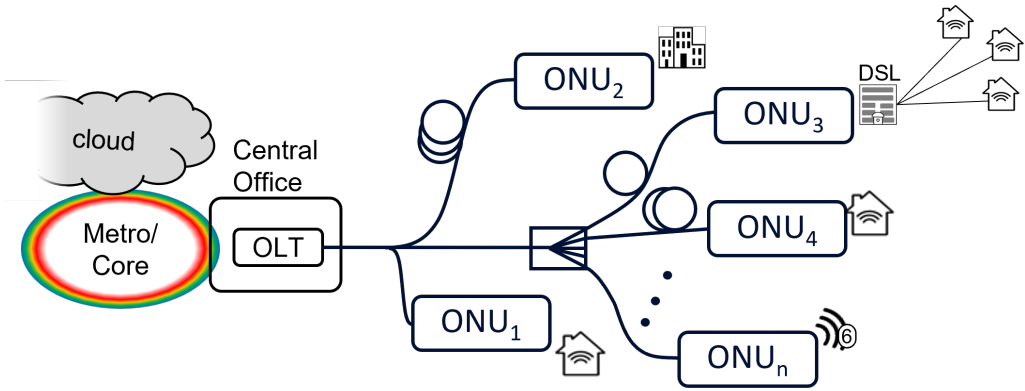


Figure 2.1: Passive optical networks traditionally provide broadband access to residential customers.

over traditional copper-based networks. Next, broadband PON (BPON) was introduced in the early 2000s [36–40], which offers a few advancements over APON. However, as service requirements and data demands continued to grow, further development of PON technology became necessary. In response, system vendors and service providers collaborated under the umbrella organization of the International Telecommunication Union (ITU) to standardize gigabit-capable PON (GPON), which offered data rates of 2.5 Gbit/s downstream and 1.25 Gbit/s upstream [82]. In parallel, the Institute of Electrical and Electronics Engineers (IEEE) standardized Ethernet PON (EPON), which provided symmetrical data rates of 1 Gbit/s for both downstream and upstream traffic [83]. As of today, GPON remains the most widely deployed PON technology due to its reliability, cost-effectiveness, and capability to deliver broadband services at sufficient data rates for most applications to date.

In the late 2000s, various new applications began to emerge and gradually became mainstream, such as ultra-high-speed internet, 4K video streaming, online gaming, cloud computing, and the Internet of Things (IoT). To address the requirements of such high-bandwidth applications, the ITU standardized the 10 gigabit-capable PON in the late 2000s, which is also known as XG-PON [41–43]. Later, the ITU released a second version of this standard, which supports symmetric data rates (known as XGS-PON) for both upstream and downstream traffic [44, 45].

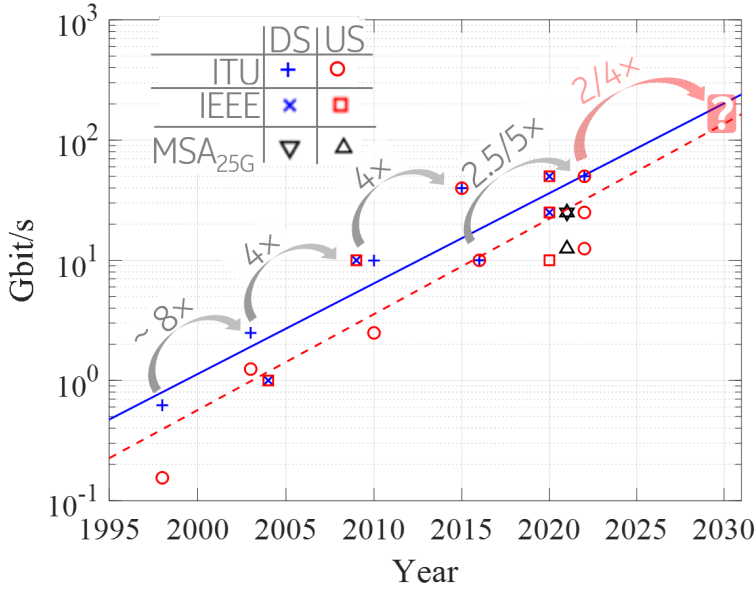


Figure 2.2: The upstream and downstream line rate of different ITU and IEEE PON standard over time.

Based on recent OLT and ONU module shipment information, XGS-PON is becoming an increasingly mainstream access technology [59, 60, 84].

Recently, two high-speed PON standards have been finalized. The first, developed through a multi-source agreement (MSA), supports a data rate of up to 25 Gbit/s and is known as 25G MSA PON [46]. It is designed for premium enterprise services, which require high reliability and low latency. To date, 25G PON is the highest data rate PON technology commercially available. The second is the result of the ITU's high-speed PON (HSP) project and supports a data rate of 50 Gbit/s, known as 50G PON [47–50]. It is the highest data rate PON standard to date. Figure 2.2 summarizes the upstream and downstream line rates of various ITU and IEEE PON standards over time. Generally, standardization bodies typically finalize a new standard every five to ten years, with each generation achieving at least a fourfold increase in peak rate. As a result, we can expect a new PON standard to be finalized by the end of this decade, as indicated by a red question mark in Fig. 2.2. Furthermore, the fitted curves illustrate that the peak data rate

is expected to increase by a factor of two to four compared to the current 50G PON standard [85]. Here, blue and red-dashed lines represent the downstream and upstream rates, respectively.

2.1.3 Very-High-Speed PON and challenges

Currently, the ITU's Study Group 15 (SG15) Subgroup Question 2 (Q2) is considering different technology options as part of the very-high-speed PON (VHSP) supplement project, G.sup.VHSP [86]. The VHSP system generation is expected to come with a diverse set of bandwidth, reliability, cost, and power consumption requirements, aiming to provide optical connectivity to different classes of services and applications. The target line rates for the VHSP are in the range of 100 to 200 Gbit/s, which are being analyzed in the G.sup.VHSP project by considering different application requirements, operator demands, component availability, and cost structure [52, 60, 77, 84]. Until now, intensity modulation and direct detection (IM/DD) has been the technology of choice for all legacy PON standards due to its cost advantage and simple optical front end. Designing a >100 Gbit/s PON using IM/DD techniques will be more challenging, especially one that can bridge the 20-40 km optical link and has a 30 dB or more ODN loss budget [59]. Therefore, the introduction of coherent transceivers is a potential solution for VHSP. Furthermore, the trend to maximize efficiency and flexibility across the optical access system calls for scalable, elastic, and granular features that can host diverse services like residential, business, enterprise, and mobile transport onto a common ODN.

Therefore, coherent PONs based on DP-IQM and coherent reception are considered with high expectations for improving receiver sensitivity and overall system performance [53, 71, 87–89]. Figure 2.3 illustrates a potential VHSP system, which supports a few novel applications. Typically, coherent transceivers are equipped with calibrated, narrow-linewidth tunable lasers [65], whose output is internally split to serve both as the transmit light source and the local oscillator (LO). However, this transceiver design exhibits limited performance in

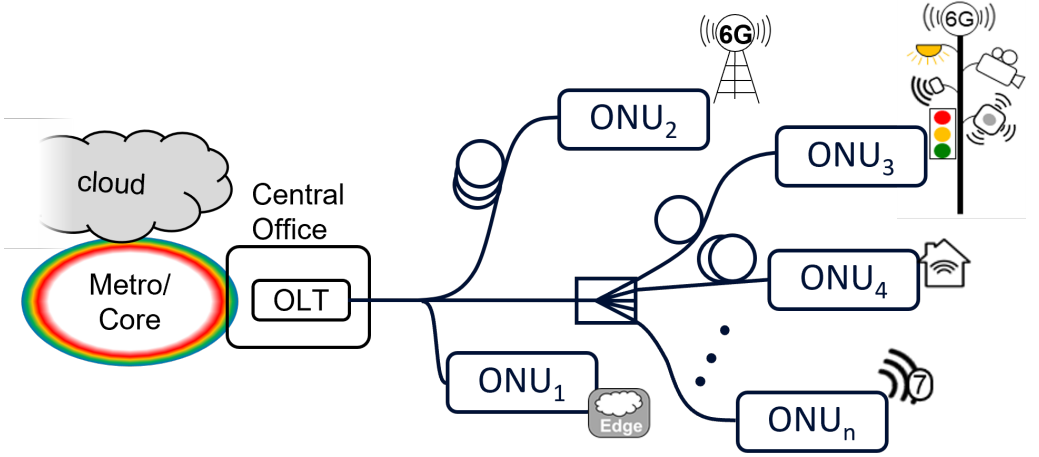


Figure 2.3: The next generation PON is expected to support different classes of end-user.

bidirectional scenarios due to distributed Rayleigh backscattering (DRBS) [90]. Consequently, a dual-laser transceiver design might be required for bidirectional coherent PONs. Alternative solutions to the DRBS issue have also been proposed. One approach, discussed by H. Rohde et al. in [91], uses different sub-bands for upstream and downstream. Another solution, presented by S. Shibita et al. in [92], demonstrates a digital reflection interference cancellation scheme.

Furthermore, coherent technology presents a challenging cost structure for access network applications [85, 93]. Broadly speaking, a coherent transceiver consists of four main sub-blocks: the optical front end, digital signal processor, driver electronics, and laser. Among these, the laser is one of the most expensive components, accounting for roughly one-fourth of the total transceiver cost [94]. Note that coherent transceivers, developed for metro or long-haul communication, typically employ narrow-linewidth, fully tunable, and frequency-stable lasers. Those lasers may not meet the cost targets for optical access networks. Therefore, a simpler laser, such as a distributed feedback (DFB) laser, offers advantages over an external cavity laser (ECL) in terms of chip size, design, and packaging complexity. Additionally, using an uncalibrated laser can further reduce testing and calibration requirements. Therefore, it is more beneficial for ONUs to employ uncalibrated DFB lasers from a cost perspective. However, uncalibrated lasers

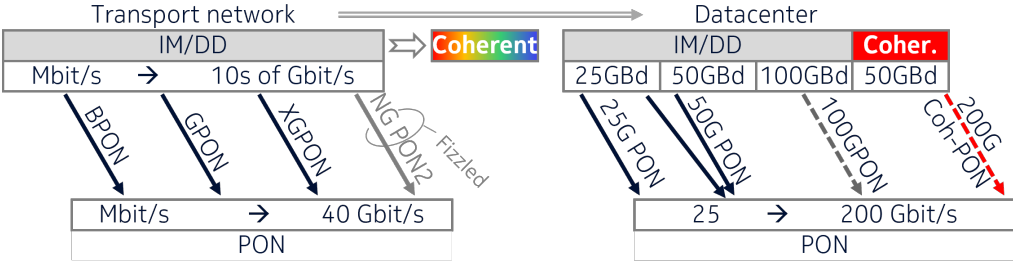


Figure 2.4: PON reuses the components from high-volume market [14]

introduce additional challenges in designing a coherent ONU, as the exact emission wavelength cannot be guaranteed due to fabrication tolerances. This results in wavelength uncertainty. This thesis introduces potential solutions to address the wavelength alignment issue with minimal additional complexity on the ONU side.

2.1.4 Technology Adaption in PON

The anticipated average selling price of a cost-optimized coherent transceiver (e.g., 100G ZR) for short-reach applications is expected to be at least one order of magnitude higher than 50G PON transceivers at the end of this decade [60, 95]. Therefore, it is essential to carefully evaluate the trade-offs between component availability, complexity, and performance for next generation coherent PON. In research, various types of coherent receivers are under consideration for coherent PON, ranging from single-photodiode-based Kramers-Kronig receivers to full coherent receivers. These can be broadly categorized into two groups: non-standard simplified coherent receivers and full coherent receivers.

To date, all PON generations have reused components from volume markets (e.g., transport or data center) to achieve cost advantages by minimizing non-recurring engineering (NRE) costs. Figure 2.4 summarizes the adaptation process of component technologies from different ecosystems for PON. As shown, B-PON to XGS-PON adopted IM/DD component technologies from transport networks. The next generation PON2 (NG-PON2) [68] was not commercially successful

because the 40G transport market did not materialize as expected, and later transport networks adopted 100G coherent technology. The lesson learned from NG-PON2 is that new technologies for PON need to mature in a volume market to drive down the cost of transceivers before adopting them for PON. This is why newer system generations of PON, such as 25G and 50G PON, leverage component technologies from the 25 GBd and 50 GBd data center ecosystems [60].

Ongoing coherent PON research emphasizes the simplification of transceiver architecture [53, 67, 96]. As an example, 80% of the cost of a silicon photonics (SiPh) datacom transceiver comes from packaging, testing, and assembly [97]. In [97], it is mentioned that the receiver die accounts for only 1.2% of the total cost, whereas the transmitter die accounts for 10.2% without laser. Therefore, it can be extrapolated from this study that simplifying the receiver will not yield significant cost benefits for coherent PON. Furthermore, based on various standardization activities, there will be no volume market for simplified coherent transceivers in the near future. Therefore, it can be anticipated that the NRE cost will be much higher for simplified coherent transceivers compared to standard coherent transceivers. In contrast, data centers might employ a fully coherent optical front end in the second half of this decade [60, 77]. We can expect a mass market for such coherent transceivers for 10 km and longer applications in the near future. Considering all these facts, we are considering a fully coherent receiver and DP-IQM for coherent PON in this thesis. As mentioned before, further cost and complexity reductions are required to bring down the transceiver cost to the PON market range. Details regarding the cost and complexity of coherent ONUs, as well as the strategy of shifting complexity to the OLT side, are discussed later in chapters 3 and 4.

2.1.5 PON Coexistence

PONs are inherently end-user-centric optical access technologies. Consequently, a gradual and seamless migration from one PON generation to the next is crucial

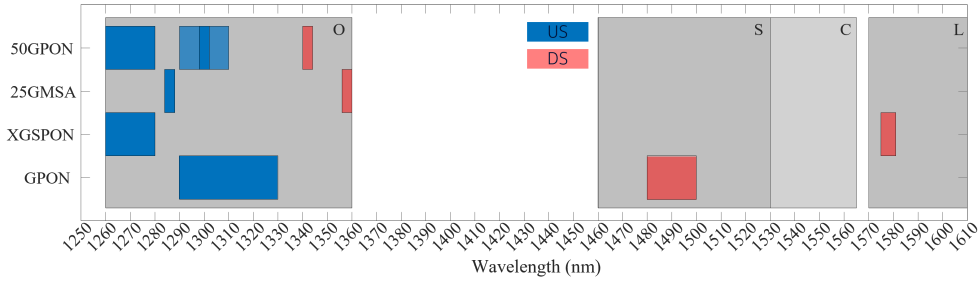


Figure 2.5: Wavelength plans of different standardized ITU-PONs. The gray shaded regions represent different optical bands. DS: downstream, US: upstream.

for network operators and service providers. Each PON standard defines specific operational wavelength bands for downstream and upstream transmission in such a way that they minimize the Raman effect as well as distributed Rayleigh backscattering, which allows for smooth PON evolution. Figure 2.5 summarizes the wavelength plans for various ITU-standardized PONs and 25G-MSA PON. In the figure, red boxes indicate the downstream wavelength windows, while blue boxes represent the upstream windows. As shown, G-PON operates in the 1480-1500 nm band for downstream and in the 1290-1330 nm band for upstream [82]. XGS-PON shifts the downstream allocation to 1575-1581 nm and upstream to 1260-1280 nm, thereby allowing coexistence with G-PON. Note that the XGS-PON's downstream band is carefully chosen to avoid Raman depletion to the G-PON upstream, which is also done for all following PON generations [44]. The 25G-MSA utilizes the 1356-1360 nm band for downstream and 1284-1288 nm for upstream [46]. In comparison, 50G-PON adopts a downstream window of 1340-1344 nm, while its upstream transmission is either at 1260-1280 nm or 1290-1310 nm bands [49]. Note that this dual allocation provides deployment flexibility, allowing coexistence with either G-PON or XGS-PON, as well as 25G-MSA PON. Additionally, a narrow upstream band around 1298-1302 nm is also standardized to support coexistence with all three legacy PON standards [47–50]. It is important to notice that both 25G-PON and 50G-PON operate entirely within the O-band for upstream and downstream transmission

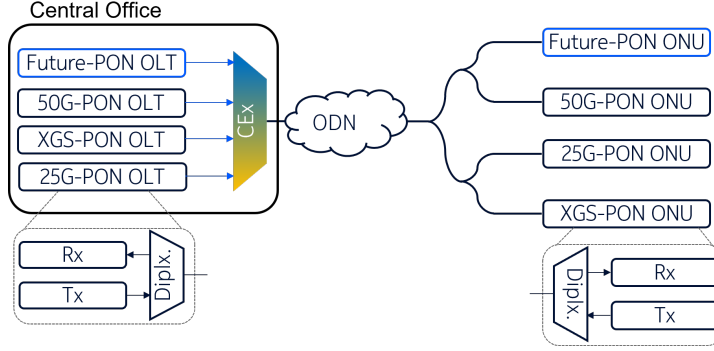


Figure 2.6: Coexistence strategies for different PON systems. CEx: coexistence element.

to deal with the increased chromatic dispersion. Furthermore, this will be even more critical for IM/DD-based VHSP, which might need to support >100 Gbit/s.

Like earlier PON generations, the VHSP must coexist with multiple previous standards, such as 50G-PON, 25G-MSA, and XGS-PON [98, 99]. Furthermore, compatibility with GPON is also highly desirable since it is the most highly deployed PON system to date. The expected coexistence architecture is illustrated in Fig. 2.6. In this setup, CEx refers to a wavelength-division multiplexing filter, also known as the coexistence element in PON. It separates the upstream and downstream signals according to each transceiver's requirements [98, 99]. Furthermore, each PON transceiver employs an additional diplexer (Diplex) to separate the upstream and downstream signals inside the transceiver module. Note that in a PON system where multiple PON technologies coexist (e.g., GPON, XGS-PON, 25G-PON, 50G-PON, and future VHSP), the combination of high aggregate optical power and closely spaced wavelengths in the O-band can lead to nonlinear effects such as four-wave mixing, cross-phase modulation, and Raman depletion. Furthermore, the high peak power and spectral purity required to achieve a high SNR may induce Stimulated Brillouin Scattering, affecting launch power and causing back-reflection. These phenomena can result in crosstalk, power imbalance, and phase noise, degrading signal integrity, particularly for higher-speed channels. Effective mitigation requires careful power management and optimized wavelength spacing. As shown in Fig. 2.5, the O-band is densely

populated compared with other optical communication bands, such as the C-band. Furthermore, the commercially available coherent optical systems are mostly designed for C-band operation. Therefore, the C-band is a technically viable optical band for coherent PON systems. It will allow the reuse of component technologies from the mature coherent market.

2.2 Coherent PON: IQ-modulation and coherent detection

In this section, we briefly introduce different types of single-line and multi-line laser sources that can be used in a coherent PON system. Next, we discuss a simplified model for the downstream and upstream operation using a single-line laser. The system model utilizing a multi-line laser is discussed in chapter 3.

2.2.1 Laser Sources

Coherent PON transceivers might require two lasers, one in the transmitter as the light source and the second in the receiver as a local oscillator. There are various options available for laser technology, ranging from low-cost, uncalibrated DFB lasers to fully calibrated tunable lasers, such as ECL. Different types of laser sources can be utilized in different parts of the PON system to address PON-specific challenges and needs. Details about this strategy will be discussed in the introductory section of chapter 3. Here, we introduce simplified models for single-line and frequency-comb sources.

2.2.1.1 Single-line source

We first consider a single-line laser emitting optical power P_L at optical frequency f_L . For convenience, we neglect amplitude noise, since it does not represent a dominant impairment in coherent PON scenario, and we describe the phase

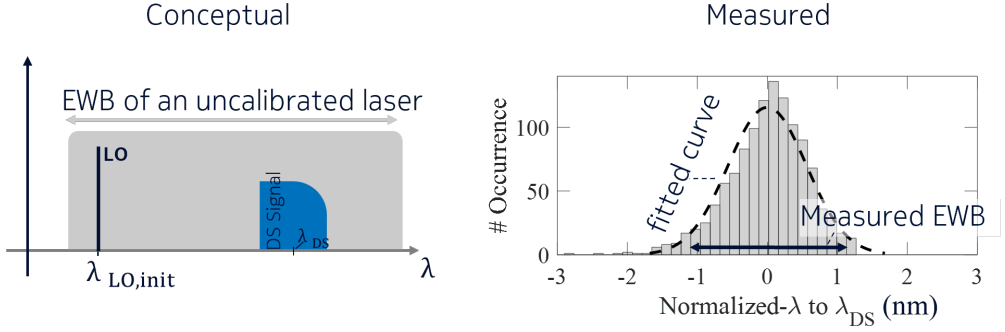


Figure 2.7: *Left:* Conceptual illustration of wavelength ambiguity arising from the use of an uncalibrated laser. *Right:* Emission wavelength range (EWR) of over 1000 uncalibrated DFB lasers at certain temperature and bias current. Normalized by the transmit laser wavelength [7]

evolution due to phase noise and frequency drift by $\phi_L(t)$. The optical field can be expressed as

$$\underline{E}_L(t) = \sqrt{P_L} e^{j[2\pi f_L t + \phi_L(t)]}. \quad (2.1)$$

Phase noise and frequency drift are influenced by several factors, including the laser design, laser type, manufacturing process, and the calibration accuracy. As mentioned before, the laser is one of the most expensive components in a transceiver and accounts for up to one-fourth of the total cost. Therefore, a relatively simple laser structure, such as a DFB laser, is more favorable for ONUs compared with more complex alternatives like ECLs. Note that the cost-optimized uncalibrated DFB lasers may emit over a broad emission wavelength range (EWR) due to fabrication tolerances. Furthermore, such lasers without temperature control are susceptible to wavelength shifts due to ambient temperature. The left plot of Fig. 2.7 illustrates the issue of emission wavelength uncertainty of an uncalibrated DFB laser. As shown in this plot, the wavelength alignment cannot be guaranteed using an uncalibrated laser. A statistical analysis of the emission wavelengths of over 1,000 DFB lasers is presented in the right plot of Fig. 2.7 [7]. Here, we can see that the EWR can span approximately ± 2 nm, which is very high with respect to the accuracy required for coherent reception. Therefore, this

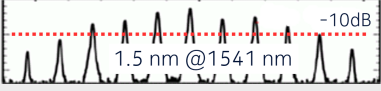

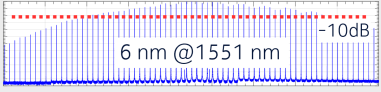
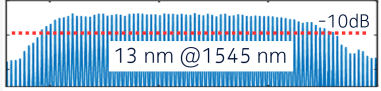
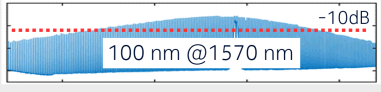
Comb generator	Free-Spectral Range (FSR)	Spectrum (Width @ center wavelength)	Reference
Electro-optic modulator (EOM)	25 GHz		C. Weimann et al., Opt. Express, 22, (2014)
Gain-switched laser diode	12.5 GHz		J. Pfeifle et al., Opt. Express, 23, (2015)
Erbium glass oscillator (ERGO)	12.5 GHz		A. Schliesser et al., Nature Photonics, 6, (2012)
Mode-locked laser diode (MLLD)	25 GHz		J. Kemal et al., OFC, Th5C., 3 (2017)
Nonlinear microresonator	100 GHz		P. Marin-Palomo et al., Nature, 546, (2017)

Figure 2.8: A summary of different frequency comb source.

wavelength variability must be carefully considered in the coherent PON system design, especially for applications requiring tight wavelength alignment, such as subcarrier-based coherent PON.

2.2.1.2 Multi-line source

The simplest way to generate a multi-line source is by combining multiple single-line lasers. For a source with $2N + 1$ laser lines, the optical field can thus be described as

$$\underline{E}_L(t) = \sum_{n=-N}^N \sqrt{P_L^{(n)}} e^{j[2\pi f_L^{(n)}t + \phi_L^{(n)}(t)]}. \quad (2.2)$$

where $P_L^{(n)}$, $f_L^{(n)}$, and $\phi_L^{(n)}$ describe the optical power, the frequency, and the phase evolution of the n -th laser line.

2.2.1.3 Frequency comb source

We refer to a multi-line source as a frequency comb source where the spectral lines have a nominally constant frequency spacing Δf_{FSR} , known as the free-spectral range (FSR), such that $f_L^{(n)} = f_L + n\Delta f_{\text{FSR}}$ and

$$\underline{E}_L(t) = \sum_{n=-N}^N \sqrt{P_L^{(n)}} e^{j[2\pi n\Delta f_{\text{FSR}}t + \phi_L^{(n)}(t)]} e^{j2\pi f_L t}. \quad (2.3)$$

2.2.1.4 Coherent frequency comb source

If we assume that the spectral lines of the frequency comb follow the same phase evolution $\phi_L(t)$ eventually with a constant phase offset $\Delta\phi_L^{(n)}$ for the n -th line, we call the multi-line laser a coherent frequency comb source. In this case, the optical field can be written as

$$\underline{E}_L(t) = \sum_{n=-N}^N \sqrt{P_L^{(n)}} e^{j[2\pi n\Delta f_{\text{FSR}}t + \Delta\phi_L^{(n)}]} e^{j[2\pi f_L t + \phi_L(t)]}. \quad (2.4)$$

If the phase offsets $\Delta\phi_L^{(n)}$ are all equal for all lines, the coherent frequency comb source is referred to as transform-limited. An example is a mode-locked laser, which generates a transform-limited frequency comb. Subsequent optical components might then lead to non-equal phase offsets $\Delta\phi_L^{(n)}$, e.g., due to chromatic dispersion. A summary of various frequency comb sources, ranging from electro-optic combs to nonlinear microresonator-based combs, is presented in Fig. 2.8. As illustrated, electro-optic modulator-based combs are constrained by the electrical bandwidth of the modulator, which ultimately limits the achievable FSR. Similarly, the FSR of gain-switched laser diodes and erbium-glass oscillator (ERGO)-based combs is also limited, although it can be adjusted through specific laser design and system optimization. Mode-locked laser diode (MLLD)-based comb sources offer a compact footprint and exhibit a flatter spectral profile

compared with other technologies, making them suitable for integration, potentially compatible with communication systems. In contrast, microresonator-based combs provide extremely broad bandwidth and high FSR, which are advantageous for high-capacity applications. However, they require very high optical power to enable the nonlinear interaction inside the microresonator and pose significant integration challenges. Note that, frequency comb sources are commercially available as benchtop instruments for laboratory applications. However, their adoption in optical communication systems remains limited due to challenges related to complexity, stability, and chip-level integration within optical integrated circuits required for telecom-grade deployment.

2.2.2 Coherent PON Downstream

Figure 2.9 shows a simplified model for the downstream (DS) operation. In this model, we are considering conventional coherent receiver architecture based on a single-line laser. The DS-relevant quantities are marked by $[\cdot]^\downarrow$. As shown in Fig. 2.9, the output of the single-line laser, as explained in Eq. (2.1), is launched into a DP-IQM. Insets ① and ② show schematics of the power spectra at the input and output of the DP-IQM, respectively. Here, we consider the data modulation with four real-valued signals $S_1(t)$, $S_2(t)$, $S_3(t)$ and $S_4(t)$ which are combined to two complex valued signals:

$$\underline{S}_x(t) = S_1(t) + j S_2(t) \quad (2.5)$$

$$\underline{S}_y(t) = S_3(t) + j S_4(t) \quad (2.6)$$

Here, the real and imaginary parts represent the in-phase and quadrature components, and the subscripts ‘x’ and ‘y’ represent two orthogonal states of polarization. For simplicity, the downstream signals are indicated by $\underline{S}_{x,y}^\downarrow(t)$, which is

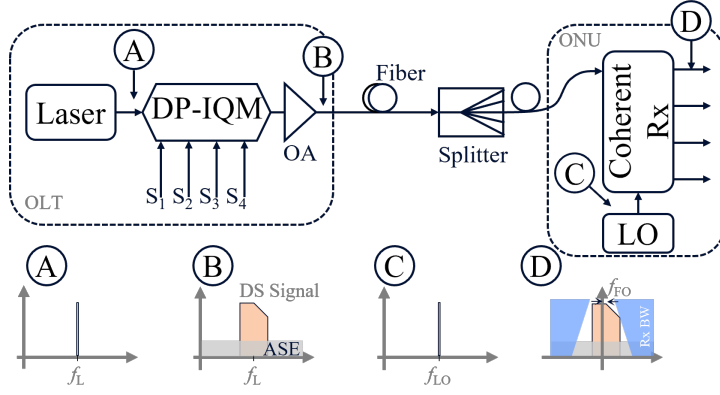


Figure 2.9: Downstream schematic of a coherent PON. At the OLT, a DP-IQM is employed to generate the downstream signal. This modulated signal is then amplified using an optical amplifier (OA) to ensure sufficient power for transmission over the fiber link. Inset (A) illustrates the optical power spectrum of the unmodulated continuous-wave laser source, while Inset (B) shows the spectrum of the modulated transmit signal. In this spectrum, the amplified spontaneous emission (ASE) noise introduced by the optical amplifier is indicated by the gray shaded region. At the ONU, a polarization-diverse coherent receiver (RX) is used to detect the incoming downstream signal. Another single-line laser uses as a local oscillator (LO) laser. Inset (C) displays the optical spectrum of the LO, with an example frequency offset from the carrier. Inset (D) illustrates the baseband spectrum of the complex-valued received signal, showing the effect of the frequency offset f_{OF} . The blue shaded areas in this inset represent the electrical bandwidth limitations of the receiver.

modulated onto the laser signal $\underline{E}_{L,x,y}(t)$. In this model, we consider a linearized modulation characteristic resulting in:

$$\underline{E}_{Tx,x}(t) = \underline{S}_x(t)\underline{E}_{L,x}(t) \xrightarrow{FT} \tilde{\underline{E}}_{Tx,x}(f) = \tilde{\underline{S}}_x(f) * \tilde{\underline{E}}_{L,x}(f) \quad (2.7)$$

$$\underline{E}_{Tx,y}(t) = \underline{S}_y(t)\underline{E}_{L,y}(t) \xrightarrow{FT} \tilde{\underline{E}}_{Tx,y}(f) = \tilde{\underline{S}}_y(f) * \tilde{\underline{E}}_{L,y}(f) \quad (2.8)$$

Here, the transmit signals represent both in time and frequency domain, the symbol ‘ \sim ’ denotes the Fourier transformed signal. Additionally, the Fourier transform and the convolution operation are represented by \xrightarrow{FT} and $*$, respectively. The subscripts Tx,x and Tx,y distinguish the two orthogonal polarizations. In the frequency domain, the modulation corresponds to a convolution of the complex baseband signal with the complex amplitude of the laser. The combined X

and Y polarization downstream signals refer as $\underline{E}_{\text{Sig},x,y}^\downarrow(t)$. Next, the optical power of the modulated downstream signal $\underline{E}_{\text{Sig},x,y}^\downarrow(t)$ is boosted by using an optical amplifier with a gain $G_A^\downarrow > 1$. Note that the OA typically adds amplified spontaneous emission (ASE) noise, denoted by $\underline{E}_{\text{ASE},x,y}^\downarrow(t)$. Typically, an optical communication system employs an optical filter to limit the noise bandwidth. The combined effect of the OA bandwidth and optional filter is described by the optical impulse response $\underline{h}_o^\downarrow(t)$. The amplified DS signal $\underline{E}_{x,y}^\downarrow(t)$ at point ③ in Fig. 2.9 can thus be expressed as:

$$\underline{E}_{x,y}^\downarrow(t) = \left[\sqrt{G_A^\downarrow} \underline{E}_{\text{Sig},x,y}^\downarrow(t) + \underline{E}_{\text{ASE},x,y}^\downarrow(t) \right] * \underline{h}_o^\downarrow(t). \quad (2.9)$$

The complex noise term $\underline{E}_{\text{ASE},x,y}^\downarrow(t)$ is modeled as zero-mean, circularly symmetric additive white Gaussian noise (AWGN). If the transmit signal is amplified beyond a certain power threshold, fiber nonlinearities may arise, introducing distortions that are significantly more difficult to compensate. However, in the absence of optical amplification, the transmit signal can be expressed as:

$$\underline{E}_{x,y}^\downarrow(t) = \sqrt{G_{\text{Tx}}^\downarrow} \underline{E}_{\text{Sig},x,y}^\downarrow(t). \quad (2.10)$$

Here, G_{Tx}^\downarrow represents the transmitter insertion loss (therefore, $G_{\text{Tx}}^\downarrow < 1$). At the i th ONU, a single-line laser is used as the local oscillator, along with a polarization-diverse coherent receiver. The ODN loss is denoted by $G_{\text{ODN}}^{(i)} < 1$. The corresponding fiber impulse responses connect the un-primed polarizations and the primed received polarizations, $\underline{h}_{x'x}^{(i)}(t)$, $\underline{h}_{x'y}^{(i)}(t)$, $\underline{h}_{y'x}^{(i)}(t)$, $\underline{h}_{y'y}^{(i)}(t)$, including the effect of chromatic dispersion (CD) and polarization rotation (PR). The optical signals $\underline{E}_{x',y'}^{\downarrow(i)}(t)$, received in the x' and y' polarizations by the coherent receiver at the i th ONU, are described by the following equations:

$$\underline{E}_{x'}^{\downarrow(i)}(t) = \sqrt{G_{\text{ODN}}^{(i)}} \left[\underline{h}_{x'x}^{(i)}(t) * \underline{E}_x^\downarrow(t) + \underline{h}_{x'y}^{(i)}(t) * \underline{E}_y^\downarrow(t) \right], \quad (2.11)$$

$$\underline{E}_{y'}^{\downarrow(i)}(t) = \sqrt{G_{\text{ODN}}^{(i)}} \left[\underline{h}_{y'x}^{(i)}(t) * \underline{E}_x^\downarrow(t) + \underline{h}_{y'y}^{(i)}(t) * \underline{E}_y^\downarrow(t) \right]. \quad (2.12)$$

A schematic of the power spectrum of the LO is shown in Fig. 2.9 inset ㉔, centered at $f_{LO}^{(i)}$ with an example frequency offset (FO) of $\Delta f_{FO}^{(i)} = f_L^{(OLT)} - f_{LO}^{(i)}$. In the ONU receiver, the LO mixes with the received downstream signal in the coherent receiver, resulting in the electrical data signals $r_{x',y'}^{(i)}(t)$. The combined effect of shot noise and thermal noise is added to the signal, which is denoted as $n_{x',y'}^{(i)}(t)$. The quantity $h_{RX}^{(i)}(t)$ for the i th ONU represents the real-valued electrical impulse response for the I and Q components in the x' - and y' -polarizations. The corresponding transfer functions are assumed to be identical. Furthermore, $R^{(i)}$ is a constant conversion factor that includes the photodiode responsivity and the gain of the electrical amplifiers for all balanced receivers. The resulting received electrical signal is:

$$r_{x',y'}^{(i)}(t) = \left[R^{(i)} \underline{E}_{LO,x',y'}^{(i)}(t) \underline{E}_{x',y'}^{\downarrow(i)}(t) + n_{x',y'}^{(i)}(t) \right] * h_{RX}^{(i)}(t) \quad (2.13)$$

Figure 2.9 inset ㉔ illustrates the power spectrum of the received complex electrical signal at the i th ONU. The blue shaded region highlights the effect of the receiver's low-pass filter characteristics. Due to cost considerations, no optical amplifier is placed inside the ONU module as shown in Fig. 2.9. As a result, the dominant noise sources are shot noise from the LO and the thermal noise from the electronics. Digital signal processing can typically compensate for impairments introduced by CD, polarization rotation, and the bandwidth limitations of both the transmitter and receiver. However, if the transmitted signal is amplified beyond a certain power threshold at the OLT, fiber nonlinearities may become significant. These are more challenging to mitigate.

2.2.3 Coherent PON Upstream

Figure 2.10 presents a simplified model of the upstream (US) operation. As in the downstream case, upstream-relevant quantities are denoted by $[\cdot]^\uparrow$. At the ONU transmitter, a single-line laser acts as the optical source, defined analogously to Eq. (2.1). Inset ㉕ of Fig. 2.10 illustrates the power spectrum of this laser at point ㉕. The upstream signal $\underline{S}_{x',y'}^\uparrow(t)$ is modulated onto the optical carrier $\underline{E}_{L,x',y'}^{(i)}(t)$

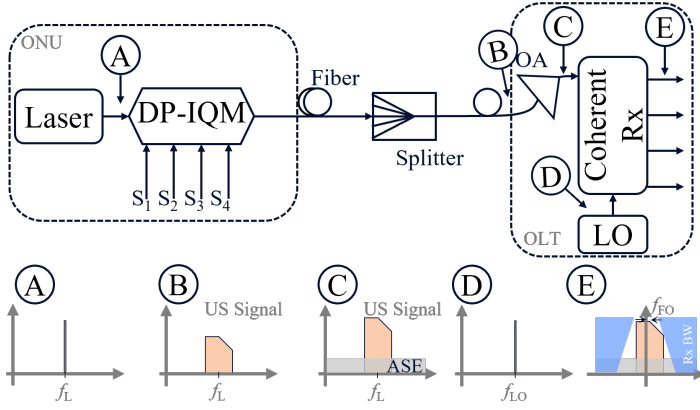


Figure 2.10: Upstream schematic of the a coherent PON. At the ONU transmitter, a single line laser is employed as the light source, followed by a DP-IQM to encode the upstream data onto the optical carrier. Inset (A) illustrates the optical spectrum of the single-line laser, while Inset (B) shows the spectrum of the upstream signal at the OLT. On the OLT side, an optical amplifier is used as a pre-amplifier to pre-amplify the incoming upstream signal prior to detection. Inset (C) depicts the optical spectrum of the amplified upstream signal with ASE noise. The OLT incorporates a coherent receiver and utilizes another single-line laser as the LO. Inset (D) depicts the optical spectrum of the LO laser. Inset (E) presents the baseband spectrum of the complex-valued received signal, where the blue shaded regions indicate the electrical bandwidth limitations of the receiver.

using a DP-IQM as in the downstream case. The resulting modulated signal $\underline{E}_{x',y'}^{\uparrow(i)}(t)$ from the i th ONU is launched into the ODN. The upstream transmit signal can be expressed as:

$$\underline{E}_{x',y'}^{\uparrow(i)}(t) = \sqrt{G_{Tx}^{\uparrow(i)}} \underline{E}_{L,x',y'}^{(i)}(t). \quad (2.14)$$

As noted previously, the DP-IQM exhibits linear modulation characteristics. The power spectrum of the upstream signal at point (B) is shown in inset (B) of Fig. 2.10. In this configuration, we assume that the ONU transmits signals in both x' -

and y' -polarizations, which are received at the OLT in x'' - and y'' -polarizations, respectively.

$$\underline{E}_{\text{Sig},x''}^{\uparrow(i)}(t) = \sqrt{G_{\text{ODN}}^{(i)}} \left[\underline{h}_{x''x'}^{(i)}(t) * \underline{E}_{x'}^{\uparrow(i)}(t) + \underline{h}_{x''y'}^{(i)}(t) * \underline{E}_{y'}^{\uparrow(i)}(t) \right], \quad (2.15)$$

$$\underline{E}_{\text{Sig},y''}^{\uparrow(i)}(t) = \sqrt{G_{\text{ODN}}^{(i)}} \left[\underline{h}_{y''x'}^{(i)}(t) * \underline{E}_{x'}^{\uparrow(i)}(t) + \underline{h}_{y''y'}^{(i)}(t) * \underline{E}_{y'}^{\uparrow(i)}(t) \right]. \quad (2.16)$$

The optical pre-amplifier with power gain $G_A^{\uparrow(i)} > 1$ adds ASE noise $\underline{E}_{\text{ASE},x'',y''}^{\uparrow(i)}(t)$ as discussed in Section 2.2.2. The optical signal to noise ratio depends on the instantaneous optical power of the upstream signal and OA gain $G_A^{\uparrow(i)}$. The pre-amplified upstream signal at the OLT reads

$$\underline{E}_{x'',y''}^{\uparrow(i)}(t) = \left[\sqrt{G_A^{\uparrow(i)}} \sum_i \underline{E}_{\text{Sig},x'',y''}^{\uparrow(i)}(t) + \underline{E}_{\text{ASE},x'',y''}^{\uparrow(i)}(t) \right] * \underline{h}_o^{\uparrow(i)}(t). \quad (2.17)$$

The power spectrum of the amplified upstream signal with ASE noise at point © is shown in inset © of Fig. 2.10. At the OLT side, we consider a second single-line laser source as the LO and a coherent receiver. Figure 2.10 inset ④ illustrates the power spectrum of the LO at position ④. Here, the quantity R is a constant conversion factor including the responsivity and the gain of the electrical amplifiers of the coherent receiver. The received electrical signal can be written as

$$\underline{r}_{x'',y''}(t) = \left[R \underline{E}_{\text{LO},x'',y''}(t) \underline{E}_{x'',y''}^{\uparrow(i)}(t) + \underline{n}_{x'',y''}(t) \right] * h_{\text{RX}}(t). \quad (2.18)$$

Figure 2.10 inset ⑤ illustrates the power spectrum of the complex received electrical signal measured at position ⑤. The shaded regions represent the effect of the low-pass characteristic of the coherent receiver. As shown in Fig. 2.10, an optical pre-amplifier at the OLT side adds ASE noise. So the upstream signal is mostly impaired by optical noise, since ASE is dominant over the combined thermal noise and shot noise in the receiver.

3 Colorless Coherent TDM-PON

This chapter explores the usability of the frequency comb laser in time-division-multiplexed (TDM) passive optical networks. This chapter is based on a paper [1], which was published in the *Journal of Lightwave Technology*. The material from the publication is reproduced here with the appropriate changes to fit the structure and notation of this thesis.

Start of Journal [1]

Copyright © Open Access Under a Creative Commons License

Colorless Coherent TDM-PON Based on a Frequency-Comb Laser

Journal of Lightwave Technology, Volume: 40, Issue: 13, pp. 4287-4299

DOI: 10.1109/JLT.2022.3164168

Md Mosaddek Hossain Adib¹, Christoph Füllner¹, Juned N. Kemal^{1,2}, Pablo Marin-Palomo^{1,3}, Abderrahim Ramdane⁴, Christian Koos¹, Wolfgang Freude¹, and Sebastian Randel¹

¹ Institute of Photonics and Quantum Electronics (IPQ), Karlsruhe Institute of Technology (KIT), Germany

² Vanguard Automation, Karlsruhe, Germany

³ Brussels Photonics (B-Phot), Vrije Universiteit Brussel, Belgium

⁴ Centre de Nanosciences et de Nanotechnologies CNRS, Université Paris-Saclay, 91220 Palaiseau cedex, France

Coherent reception becomes an interesting option when data rates in time-division-multiplexed (TDM) passive optical networks (PONs) grow beyond 50 Gbit/s. Controlling the wavelength, i.e., the optical frequency, and the phase of the laser acting as local oscillator (LO) is one of the main technical challenges in the design of coherent TDM PONs. In the optical network units (ONUs), low-cost lasers are required, which come at the expense of wavelength variations and drifts over multiple nanometers due to fabrication imperfections, and temperature variations. This contradicts the requirement of wavelength-stable LOs in coherent receivers. The use of a wavelength locker circuit and a temperature controller is considered as too complex for applications in access networks. In this work, we propose a novel colorless coherent architecture with high resilience to ONU laser wavelength drifts of up to ± 4 nm (± 0.5 THz) for future 100 Gbit/s PON. It allows the use of distributed feedback lasers at the ONU side. This is rendered possible by generating a frequency comb with carefully chosen free spectral range in a quantum-dash mode-locked laser diode at the optical line terminal. In upstream operation, the frequency comb serves as an LO, whereas the same information is modulated onto all comb lines for the case of downstream. As a result, the ONU laser can drift over the entire comb bandwidth without substantial performance penalty. We experimentally demonstrate downstream and upstream operation with an aggregated raw data rate of 96 Gbit/s, respectively. We further introduce advanced digital signal processing (DSP) methods including a coarse frequency offset compensation (CFOC) and a multiple-input multiple-output (MIMO) equalizer to improve the performance of our concept. We show that the receiver sensitivity can be increased by 3 dB for a high-bandwidth receiver when using a 6×2 MIMO equalizer scheme. A 4×2 MIMO equalizer scheme enables colorless reception even with a limited-bandwidth receiver.

3.1 Introduction

Future optical access networks need to support the simultaneous operation of distinct service classes featuring a wide range of applications ranging from tele-operation of automated vehicles to cloud storage and the internet of things [100]. Thereby, each service class comes with its own traffic pattern and requirements in terms of bandwidth, latency and cost. Passive optical networks (PONs) based on statistical time-division multiplexing (TDM) are expected to play a key role in this scenario since they allow statistical multiplexing gains through dynamic bandwidth allocation [101]. This results in an efficient use of the fiber infrastructure resulting in significant cost advantages compared to point-to-point fiber links and static wavelength-division multiplexing. While PONs operating at a shared gross bit rate of 50 Gbit/s are currently being standardized, data rates of 100 Gbit/s and beyond will be required in the future [76, 84, 102]. In order to facilitate a smooth market introduction, coexistence with legacy PONs having a loss budget in the order of 30 dB, allowing a split factor of 64 or more, is required [103–105].

Conventional PONs rely on intensity modulation and direct detection (IM/DD) [76, 105]. However, with increasing symbol rates, the drawbacks of IM/DD, namely the limited receiver sensitivity and the lack of digital chromatic-dispersion (CD) compensation capabilities become relevant. On top of that, 100 Gbit/s IM/DD systems place high demands on the analog bandwidth of the transceiver components such as photodiodes (PDs), trans-impedance amplifiers (TIAs), digital-to-analog converters (DACs), and analog-to-digital converters (ADCs) [84, 102]. Coherent receivers in combination with inphase/quadrature (I/Q) modulation and polarization-division multiplexing (PDM) are considered a promising alternative [106]. They not only allow for reduced component bandwidth by distributing the data onto all four dimensions of the optical field but they also offer improved receiver sensitivities and they allow for digital CD compensation [106–109]. However, these benefits come at the price of an increased transceiver complexity [107–110]. Several promising concepts which simplify the coherent

receiver architecture at the optical network unit (ONU) have been proposed in literature [106–114]. Furthermore, the progress in electronic-photonic integration technology promises a considerable complexity reduction of coherent receivers in the near future [115–117]. For instance, in [118, 119], a monolithically integrated coherent receiver including TIAs on silicon and an InP-based photonic integrated circuit consisting of a distributed-feedback (DFB) laser integrated with an I/Q modulator have been demonstrated. Yet, an unsolved challenge in coherent PONs is the precise wavelength matching required between the local oscillator (LO) and the transmit laser [84, 117, 120]. For that reason, tunable external-cavity lasers (ECLs) including a wavelength locker are usually employed in metro networks, long-haul networks, and in data center interconnects. However, ECLs are not an attractive option for PONs, especially for ONUs, where DFB lasers are preferred [84, 116, 117, 120]. However, due to fabrication constraints and imperfections, the wavelength of low-cost DFB lasers typically varies from batch to batch within ± 4 nm [121–123]. Moreover, if operated uncooled, their wavelength is subject to temperature-induced wavelength drifts in the order of 0.1 nm/ $^{\circ}$ C [121, 122, 124, 125]. Several approaches such as injection-locking [126] and reflective semiconductor optical amplifiers [127] have been proposed as potential solutions to this problem. In [79, 128], a fast tuning local oscillator has been demonstrated for burst-mode coherent receivers, however, low-cost fabrication of such fast-tuning lasers remains a technical hurdle [128].

In this work, we address the challenge of wavelength matching between the lasers in the optical line terminal (OLT) and in the ONUs. We propose a novel colorless coherent TDM-PON architecture that relies on a frequency comb source in the OLT and on low-cost uncooled DFB lasers in the ONUs. All lasers can be shared between up- and downstream operation, offering a trade-off between the overall system complexity and available optical power. This work is an extension of the authors work in [21], where 48 Gbit/s upstream operation was experimentally demonstrated using an Erbium glass oscillator (ERGO) as a frequency comb source with a free-spectral range (FSR) 12.5 GHz as LO. In this work, a quantum-dash (QD) mode-locked laser diode (MLLD) is used to generate the frequency

comb. Its FSR of about 25 GHz allows for higher data rates and its compactness is promising with respect to photonic-electronic integration. Initial results on that scheme have been reported in [22]. We experimentally demonstrate both up- and downstream operation, with an aggregated raw data rate of 96 Gbit/s. Furthermore, we introduce advanced digital signal processing (DSP) schemes including a coarse frequency offset compensation (CFOC), spectral shifting of signal copies combined with multiple-input multiple-output (MIMO) equalization: while a 6×2 MIMO equalizer improves the receiver sensitivity by up to 3 dB compared to a conventional 2×2 MIMO system, it requires an increased receiver bandwidth. Here, we therefore propose using a 4×2 MIMO equalizer instead which does not require an increased receiver bandwidth. For application in intra-datacenter interconnections, a related DSP scheme based on pilot-tone-assisted frequency offset compensation was recently published in [129]. With the proposed architecture, we achieve a similar receiver sensitivity as with conventional DSP, but without the need for wavelength-locked lasers.

3.2 Colorless Coherent TDM-PON Architecture

The proposed colorless coherent TDM-PON architecture is illustrated in Fig. 3.1, with the OLT on the left-hand side and the ONUs on the right-hand side. In the OLT, the output of a frequency comb source is split in order to simultaneously act as a light source for the downstream signal and as a LO for the upstream signal. A dual-polarization I/Q modulator (DP-IQM) biased at the null point allows access to all four physical dimensions in a single-mode fiber. An Erbium-doped fiber amplifier (EDFA) operated in continuous mode is used to boost the downstream signal before it is sent to the optical distribution network (ODN) through a circulator. In upstream direction, a burst-mode EDFA acts as a pre-amplifier before the signal is detected by a burst-mode coherent receiver (BM-CRX) [78, 89]. Details about the burst-mode EDFA can be found in [88]. Digital signal processing is carried out in an integrated complementary metal-oxide-semiconductor (CMOS) circuit for the OLT, which also includes an appropriate

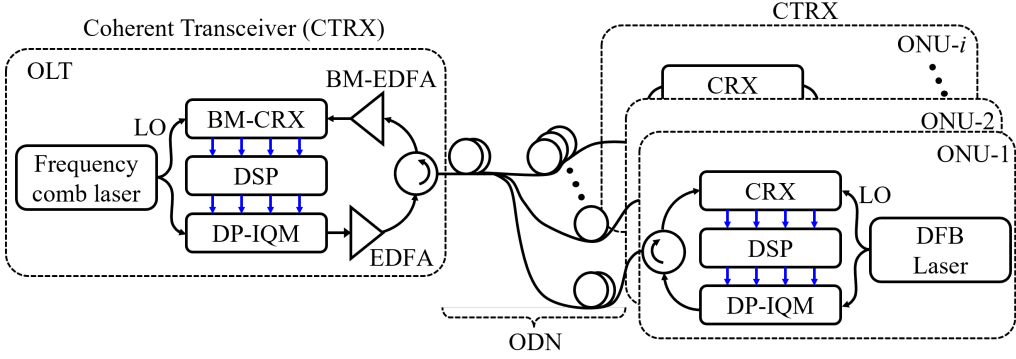


Figure 3.1: Schematic of the proposed colorless coherent TDM-PON architecture. A C-band frequency comb source is shared between transmitter and receiver at the OLT. In downstream direction, a continuous-mode EDFA is used as booster amplifier, while in upstream direction, a burst-mode (BM) EDFA is used as a pre-amplifier. In the ONU transceiver, we consider shared C-band DFB lasers for up- and downstream operation. The coherent transceivers include dual-polarization I/Q modulators (DP-IQM), polarization diverse coherent receivers (CRX), as well as digital signal processing (DSP) logic.

client interface. In the ONUs, a single DFB laser simultaneously acts as a light source for the upstream signal and as LO for the downstream. A DP-IQM is used to modulate all four dimensions in upstream operation and a coherent receiver (CRX) is used to receive the continuous downstream signal. Again, up- and downstream signals are interfaced to the ODN with a circulator. Another integrated CMOS circuit performs the required DSP at the ONUs. In bi-directional fiber links, multipath interference and Rayleigh back scattering can result in performance degradations. For a more detailed discussion and potential solutions, we refer to [91, 92].

3.3 Theoretical System Model

In this section, we briefly review the downstream and upstream operation of our proposed TDM-PON architecture. This section is as an extension of Sections 2.2

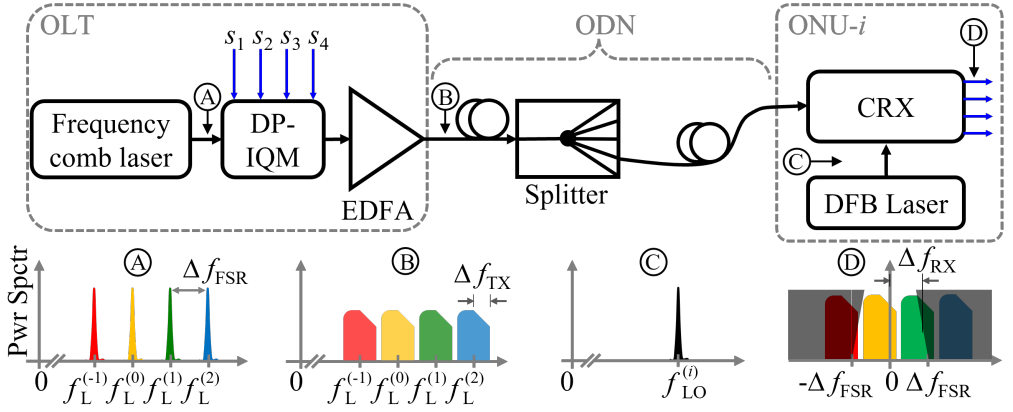


Figure 3.2: Downstream schematic of the proposed coherent PON. At the OLT, we use a coherent frequency comb laser with an FSR of Δf_{FSR} . Using a dual-polarization I/Q modulator (DP-IQM), the downstream signal is modulated onto each comb line. Subsequently, an EDFA is used to boost the resulting optical signal to the required transmit power. Insets (A) and (B) illustrate the optical power spectra of the coherent comb laser and of the modulated transmit signal, respectively. In (B), $2\Delta f_{\text{TX}}$ indicates the optical bandwidth of the comb lines modulated with complex modulation signals $\underline{s}_{x,y}(t)$, which has to be smaller than Δf_{FSR} . At each ONU, we use a polarization-diverse coherent receiver (CRX) and a distributed feedback (DFB) laser as an LO. Inset (C) illustrates the optical spectrum of the LO with an exemplary frequency offset. Inset (D) shows the resulting baseband spectrum of the complex-valued received signals. The shaded regions illustrate the effect of the receiver's electrical bandwidth Δf_{RX} .

3.3.1 Colorless Coherent Downstream

The content of this section is analogous to subsection 2.2.2. Here, the downstream (DS) model is extended to the case of colorless TDM-PON. As before, the relevant DS quantities are marked by $[\cdot]^\downarrow$. As shown in Fig. 3.2, the output of the frequency comb source in the OLT as explained with Eq. (2.4) is launched into a DP-IQM. Insets (A) and (B) show schematics of the power spectra at the input and at the output of the DP-IQM, respectively. We assume real electrical filter with a bandwidth Δf_{TX} for both the I and Q components, so that the optical signal bandwidth $\Delta f_{\text{Sig}} = 2\Delta f_{\text{TX}}$. The DS signal $\underline{S}_{x,y}^\downarrow(t)$ is modulated on the frequency comb $\underline{E}_{L,x,y}(t)$ using DP-IQM. The output signal $\underline{E}_{\text{Sig},x,y}^\downarrow(t)$ follows the liner modulation characteristics as mentioned in previous chapter. In order to avoid spectral overlap,

the bandwidth Δf_{Sig} of the transmit signal needs to be smaller than the FSR of the source, i.e., $2\Delta f_{\text{TX}} \leq \Delta f_{\text{FSR}}$. Notice that each comb line is modulated by the same data signal, and hence, each spectral line carries the same information. By tailoring the spectrum of the comb laser, compatibility with existing PON standards can be ensured. Next, we boost the power of resulting optical signal $\underline{E}_{\text{Sig},x,y}^\downarrow(t)$ with an EDFA. Within its gain window (typically in the range of 30 nm [130]), the EDFA with power gain $G_A^\downarrow > 1$ adds ASE noise $\underline{E}_{\text{ASE},x,y}^\downarrow(t)$ to the signal. Optionally, an optical filter, which passes the modulated comb lines only, could be added to limit the noise bandwidth. The combined effect of EDFA bandwidth and optional filter is described by the optical impulse response $\underline{h}_o^\downarrow(t)$. As introduced in previous chapter, the symbol $*$ describes convolution. The amplified DS signal $\underline{E}_{x,y}^\downarrow(t)$ at point ③ in Fig. 3.2 can thus be expressed as

$$\underline{E}_{x,y}^\downarrow(t) = \left[\sqrt{G_A^\downarrow} \underline{E}_{\text{Sig},x,y}^\downarrow(t) + \underline{E}_{\text{ASE},x,y}^\downarrow(t) \right] * \underline{h}_o^\downarrow(t), \quad (3.1)$$

which is analogous to Eq. 2.9. The complex noise term $\underline{E}_{\text{ASE},x,y}^\downarrow(t)$ is modelled by zero-mean circularly-symmetric AWGN. At the i th ONU, we consider a DFB laser as the local oscillator and a balanced polarization-diverse coherent receiver. Inside the ODN, the power “gain” $G_{\text{ODN}}^{(i)} < 1$ describes the ODN power loss from point ③ at the OLT to the i th ONU input of the balanced photodiode. The optical signals $\underline{E}_{x',y'}^{\downarrow(i)}$ received in x' , y' polarizations by the photodetectors of the balanced receivers in the i th ONU are described by the following equations

$$\underline{E}_{x'}^{\downarrow(i)}(t) = \sqrt{G_{\text{ODN}}^{(i)}} \left[\underline{h}_{x'x}^{(i)}(t) * \underline{E}_x^\downarrow(t) + \underline{h}_{x'y}^{(i)}(t) * \underline{E}_y^\downarrow(t) \right], \quad (3.2)$$

$$\underline{E}_{y'}^{\downarrow(i)}(t) = \sqrt{G_{\text{ODN}}^{(i)}} \left[\underline{h}_{y'x}^{(i)}(t) * \underline{E}_x^\downarrow(t) + \underline{h}_{y'y}^{(i)}(t) * \underline{E}_y^\downarrow(t) \right]. \quad (3.3)$$

A schematic of the power spectrum of the LO is shown in Fig. 3.2 inset ④, centered at an exemplary frequency $f_{\text{LO}}^{(i)}$, which can take arbitrary values within the range

of the modulated comb spectrum at point ③. The mathematical descriptions of a single-line LO for the i th ONU in x' - and y' -polarization is in analogy to Eq. (2.1)

$$\underline{E}_{\text{LO},x',y'}^{(i)}(t) = \sqrt{P_{\text{LO}}^{(i)}} e^{j[2\pi f_{\text{LO}}^{(i)}t + \phi_{\text{LO}}^{(i)}(t)]}. \quad (3.4)$$

In the ONU receiver, the LO mixes with the received downstream signal in balanced photodetectors, resulting in the electrical data signals $\underline{r}_{x',y'}^{(i)}(t)$. As mentioned before, the combined effect of shot noise and thermal noise $\underline{n}_{x',y'}^{(i)}(t)$ is added. The quantity $h_{\text{RX}}^{(i)}(t)$ for the i th ONU represents the real electrical impulse responses for the I and Q signals in x' - and y' -polarization. The corresponding transfer functions are assumed to be identical with a single-sided bandwidth Δf_{RX} . Furthermore, $R^{(i)}$ is a constant conversion factor including the responsivity and the gain of the electrical amplifiers for all balanced receivers. The resulting received electrical signal is

$$\underline{r}_{x',y'}^{(i)}(t) = \left[R^{(i)} \underline{E}_{\text{LO},x',y'}^{(i)}(t) \underline{E}_{x',y'}^{\downarrow(i)}(t) + \underline{n}_{x',y'}^{(i)}(t) \right] * h_{\text{RX}}^{(i)}(t) \quad (3.5)$$

Figure 3.2 inset ④ illustrates the power spectrum of the received complex electrical signal at the i th ONU. The shaded region illustrates the effect of the receiver's low-pass characteristics. To avoid cost issues, no EDFA is put in front of the ONU. Therefore we expect that LO shot noise and thermal noise from the electronic circuits are the dominating noise sources. Using DSP, the impairments caused by CD and PR as well as bandwidth limitations of the transmitter and the receiver can be compensated to a large extent. If the transmit signal is boosted above a certain power level, we also expect impairments from fiber nonlinearities which are more difficult to mitigate.

3.3.2 Colorless Coherent Upstream

Figure 3.3 shows a simplified model for the upstream (US) operation of colorless coherent PON. This model is an extended version of subsection 2.2.3. As before,

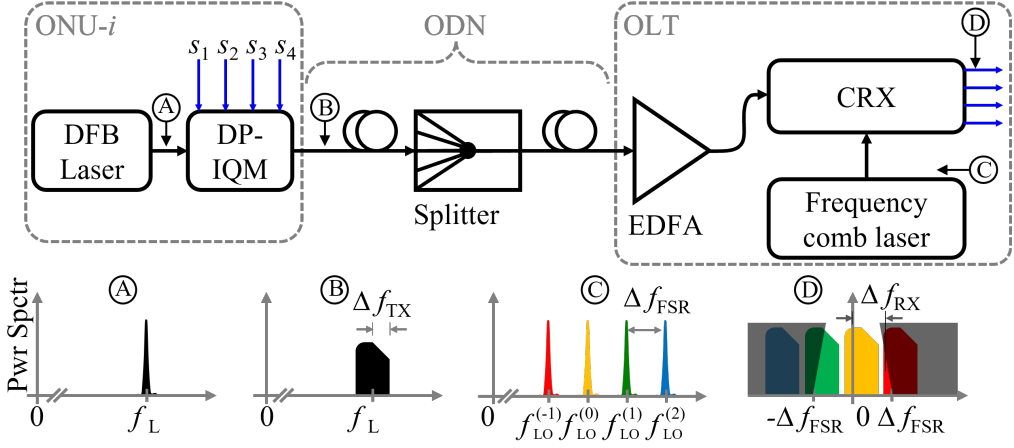


Figure 3.3: Upstream schematic of the proposed coherent PON. At the ONU transmitter, we use a DFB laser which is followed by a DP-IQM. Insets (A) and (B) illustrate the optical spectra of the DFB laser and of the modulated signal, respectively. At the OLT side, we use an EDFA as a pre-amplifier, a coherent receiver (CRX) and a coherent frequency comb laser as an LO with an FSR of Δf_{FSR} . Inset (C), illustrates the optical spectrum of the LO frequency comb and inset (D) shows the baseband spectrum of the complex-valued received signals. The shaded regions illustrate the effect of the receiver's electrical bandwidth Δf_{RX} .

the US relevant quantities are marked by $[\cdot]^\uparrow$. At the ONU, a DFB laser acts as the transmit laser defined in analogy to Eq. (3.4). Inset (A) of Fig. 3.3 shows a schematic of the power spectrum of a single-line laser as seen at position (A) in Fig. 3.3. The US signal $\underline{s}_{x',y'}^\uparrow(t)$ is modulated onto this carrier $\underline{E}_{L,x',y'}^{(i)}(t)$ using a DP-IQM. The modulated US optical signal $\underline{E}_{x',y'}^{\uparrow(i)}(t)$ from the i th ONU is launched into the ODN and transmitted in bursts as a TDM signal. The DP-IQM follows the linear modulation characteristics. The power spectrum of the modulated signal at position (B) in Fig. 3.3 is shown in inset (B). The quantity $\Delta f_{\text{TX}} \leq \frac{1}{2}\Delta f_{\text{FSR}}$ corresponds to the bandwidth of the complex transmitted signal. The optical signal from the i th ONU received at the OLT can be written with definitions in analogy to Eq. (3.2)–(3.3). However, while the ONU sends out signals in x' - and y' -polarizations, the OLT receives them in x'' - and y'' -polarizations

$$\underline{E}_{\text{Sig},x''}^{\uparrow(i)}(t) = \sqrt{G_{\text{ODN}}^{(i)}} \left[\underline{h}_{x''x'}^{(i)}(t) * \underline{E}_{x'}^{\uparrow(i)}(t) + \underline{h}_{x''y'}^{(i)}(t) * \underline{E}_{y'}^{\uparrow(i)}(t) \right], \quad (3.6)$$

$$\underline{E}_{\text{Sig},y''}^{\uparrow(i)}(t) = \sqrt{G_{\text{ODN}}^{(i)}} \left[\underline{h}_{y''x'}^{(i)}(t) * \underline{E}_{x'}^{\uparrow(i)}(t) + \underline{h}_{y''y'}^{(i)}(t) * \underline{E}_{y'}^{\uparrow(i)}(t) \right]. \quad (3.7)$$

The EDFA pre-amplifier with power gain $G_A^{\uparrow(i)} > 1$ adds ASE noise $\underline{E}_{\text{ASE},x'',y''}^{\uparrow(i)}(t)$ as discussed in Section 3.3.1. The ASE noise power spectral density depends on the instantaneous optical power of the upstream signal and EDFA gain $G_A^{\uparrow(i)}$. The pre-amplified US signal at the OLT reads

$$\underline{E}_{x'',y''}^{\uparrow(i)}(t) = \left[\sqrt{G_A^{\uparrow(i)}} \sum_i \underline{E}_{\text{Sig},x'',y''}^{\uparrow(i)}(t) + \underline{E}_{\text{ASE},x'',y''}^{\uparrow(i)}(t) \right] * \underline{h}_o(t). \quad (3.8)$$

At the OLT side, we consider a frequency comb laser source as an LO and a balanced polarization-diverse coherent receiver (CRX). The mathematical descriptions of a LO comb for the OLT in x'' - and y'' -polarization is in analogy to Eq. (2.4),

$$\underline{E}_{\text{LO},x'',y''}(t) = \sum_{n=-N}^N \sqrt{P_{\text{LO}}^{(n)}} e^{j[2\pi n \Delta f_{\text{FSR}} t + \Delta \phi_{\text{LO}}^{(n)}]} e^{j[2\pi f_{\text{LO}} t + \phi_{\text{LO}}(t)]}. \quad (3.9)$$

Figure 3.3 inset ㉔ illustrates the power spectrum of the LO at position ㉔. In the balanced photodetectors of the OLT CRX, the LO comb mixes with the pre-amplified US signal. The quantity R is a constant conversion factor including the responsivity and the gain of the electrical amplifiers of the CRX. The received electrical signal can be written as

$$\underline{r}_{x'',y''}(t) = \left[R \underline{E}_{\text{LO},x'',y''}(t) \underline{E}_{x'',y''}^{\uparrow(i)}(t) + \underline{n}_{x'',y''}(t) \right] * h_{\text{RX}}(t). \quad (3.10)$$

Figure 3.3 inset ㉕ illustrates the power spectrum of the complex received electrical signal measured at position ㉕. The shaded regions represent the effect of the low-pass characteristic of the OLT receiver. The pre-amplifier at the OLT side adds ASE noise so that the ASE-LO beat noise is expected to dominate over the combined thermal noise and shot noise in $\underline{n}_{x'',y''}(t)$.

3.4 DSP for Colorless Coherent Reception

This section provides a detailed discussion of the DSP schemes at the receivers in the ONUs and in the OLT, respectively. According to above assumptions and in contrast to ordinary heterodyne reception, the LO frequency cannot be controlled in such a way that the downconverted signal falls completely into the RX filter window. The proposed algorithms take care of this issue and can be used both in up- and in downstream reception.

Figure 3.4 shows three different DSP schemes compared in this work whereas sketches of the signal spectra at different positions along the DSP chains are depicted in Fig. 3.5. While Fig. 3.4 (a) illustrates the reference scheme which is denoted as *DSP Scheme-I* in the following, Fig. 3.4 (b) and (c) illustrate two newly proposed schemes which are denoted as *DSP Scheme-II* and *DSP Scheme-III*, respectively. In all three schemes, the received signal is detected with an integrated coherent receiver (ICR) having 4 real-valued electrical outputs ($r_{x'',y''}(t)$ for US and $r_{x',y'}(t)$ for DS) for I and Q in two polarizations, see Eq. (3.5) and Eq. (3.10). An important difference between the schemes is that while *DSP Scheme-I* and *DSP Scheme-II* require a single-sided electrical receiver bandwidth of $\Delta f_{RX} \geq \Delta f_{FSR}$, *DSP Scheme-III* requires only half that bandwidth. The received electrical signals are sampled and quantized in 4 analog-to-digital converters (ADCs) with a sampling rate of $f_{Sa} = 2\Delta f_{RX}$.

In all three schemes, as the first step after analog-to-digital conversion, we apply front-end corrections to compensate for possible imbalances, skews, and offsets between the four receiver outputs. The real and imaginary parts in each received polarization are then combined to form a complex-valued number as indicated by the double-line arrows in Fig. 3.4 at points ① and ②, respectively.

As pointed out earlier, we allow the emission frequency of a DFB laser to vary within a broad range due to temperature changes and manufacturing tolerances. This implies that the frequency offset between the DFB laser and the closest line of the frequency comb source in the OLT is different for each ONU. In upstream

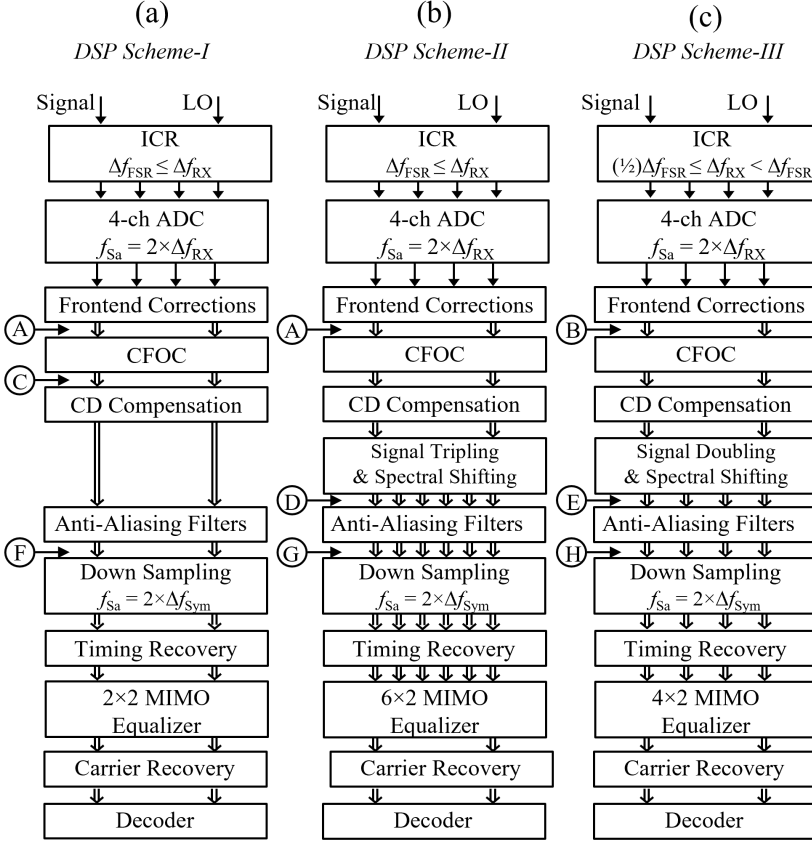


Figure 3.4: Three different DSP schemes: (a) Reference scheme with 4-channel ADC and a sampling rate two times the electrical bandwidth Δf_{RX} of the receiver, followed by a coarse frequency offset compensation (CFOC), chromatic dispersion (CD) compensation, and anti-aliasing filters. The reduced-bandwidth signal is down-sampled with a sampling rate f_{Sa} two times the symbol rate Δf_{Sym} , which is in practice slightly smaller than the Nyquist rate Δf_{RX} . Timing recovery, multiple-input multiple-output (MIMO) equalization, carrier recovery, and finally demapping and decoding concludes the DSP chain. This scheme requires a receiver bandwidth of $\Delta f_{\text{RX}} \geq \Delta f_{\text{FSR}}$. (b) Advanced DSP scheme with signal tripling, spectral shifting by $\pm \Delta f_{\text{FSR}}$ and 6×2 MIMO equalizer, which again requires a receiver bandwidth of $\Delta f_{\text{RX}} \geq \Delta f_{\text{FSR}}$. (c) The DSP scheme with signal doubling, spectral shifting by $+\Delta f_{\text{FSR}}$ or $-\Delta f_{\text{FSR}}$ and 4×2 MIMO equalization. Here, the receiver bandwidth requirement is reduced to $\Delta f_{\text{FSR}} > \Delta f_{\text{RX}} \geq \frac{1}{2} \Delta f_{\text{FSR}}$. Notice that single-line arrows represent real-valued signals whereas double-line arrows represent complex-valued signals.

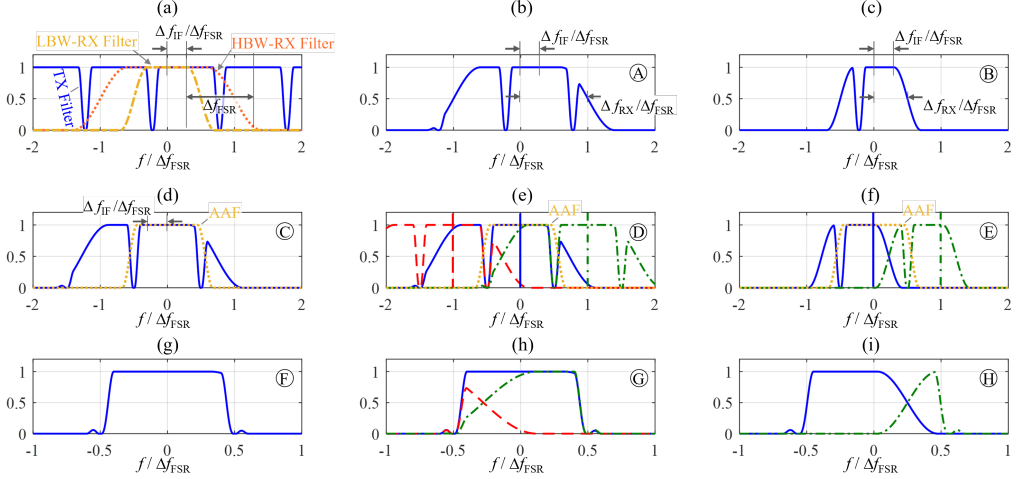


Figure 3.5: Schematic representations of baseband signal spectra at different positions along the three different DSP schemes in Fig. 3.4, indicated by encircled capital letters (A)-(H). In the present example, the symbol rate is set to $f_{\text{Sym}} = (8/9) \times \Delta f_{\text{FSR}}$ for avoiding spectral overlap caused by finite TX filter slopes. (a) Reference signal spectrum after ideal balanced detection if the receiver bandwidth is infinitely large. The TX filter slopes are clearly to be seen. The frequency offset is set to $(5/16) \times f_{\text{Sym}}$. The dash-dotted yellow and dotted orange lines represent low- and high-bandwidth receive filters, respectively. (b) Signal spectrum if the one-sided half-power bandwidth of the receiver filter equals the FSR ($\Delta f_{\text{RX}} = \Delta f_{\text{FSR}}$). In this case, we receive a full copy of the data spectrum, and a partial copy of the spectra at either side. (c) Signal spectrum if the bandwidth of the receiver filter equals half the FSR ($\Delta f_{\text{RX}} = \frac{1}{2} \Delta f_{\text{FSR}}$). In this case, only (two) partial copies of the data spectrum are received. (d) Power spectrum after coarse frequency offset estimation (CFOC) in case of $\Delta f_{\text{RX}} = \Delta f_{\text{FSR}}$. The dotted yellow line represents anti-aliasing filter (AAF). (e) Power spectra after Signal Tripling & Spectral Sifting in case of $\Delta f_{\text{RX}} = \Delta f_{\text{FSR}}$. The signal after CFOC is colored in blue, whereas its copies shifted by $-\Delta f_{\text{FSR}}$ and $+\Delta f_{\text{FSR}}$ after CFOC are highlighted in red (dashed) and green (dash-dotted), respectively. The dotted yellow line represents AAF. (f) Power spectra after CFOC and Signal Doubling & Spectral Sifting in case of $\Delta f_{\text{RX}} = \frac{1}{2} \Delta f_{\text{FSR}}$. The dotted yellow line represents AAF. (g) Power spectrum after AAF in case of *DSP Scheme-I*. (h) Power spectrum after AAF in the case of *DSP Scheme-II*. The MIMO equalizer combines coherently the blue, the red, and the green signals and hence improves the SNR. (i) Power spectrum after AAF in case of *DSP Scheme-III*. Note that for sub-figures (g-i) the horizontal scale doubles.

operation, the received spectra can therefore be positioned anywhere within the range of the LO frequency comb. Similarly, in downstream operation, the LO in the ONU can be positioned anywhere within the modulated frequency comb spectrum. Dependent on the available receiver bandwidth, we propose either *DSP Scheme-II* or *DSP Scheme-III* in order to optimize the system performance. In Fig. 3.5 (a-c), we consider the following three cases:

- I) *Reference case* without any receiver-bandwidth limitation. The reference power spectrum after ideal balanced detection and front-end correction includes one copy of the signal spectrum per comb line as sketched in Fig. 3.5 (a). The dash-dotted yellow and dotted orange lines represent low- and high-bandwidth receive filters, respectively. The intermediate frequency in US is $\Delta f_{\text{IF}}^{(i)\uparrow} = \min |f_{\text{L}}^{(i)} - (f_{\text{LO}} + n\Delta f_{\text{FSR}})|$, and in DS we have $\Delta f_{\text{IF}}^{(i)\downarrow} = \min |(f_{\text{L}} + n\Delta f_{\text{FSR}}) - f_{\text{LO}}^{(i)}|$. If the frequency offset is referred to as $\Delta f_{\text{IF}}^{(i)}$ only, it has to be properly interpreted as either $\Delta f_{\text{IF}}^{(i)\uparrow}$ or $\Delta f_{\text{IF}}^{(i)\downarrow}$.
- II) *Receiver bandwidth* $\Delta f_{\text{FSR}} \leq \Delta f_{\text{RX}}$. The received spectrum contains at least one full copy of the data spectrum and usually partial copies towards higher and lower frequencies, depending on the frequency of the DFB laser with respect to the comb source frequency. From now on, we refer to this receiver as the *high-bandwidth receiver* (HBW-RX). An exemplary power spectrum at point ① in Fig. 3.4 (a,b) with a frequency offset of Δf_{IF} is sketched in Fig. 3.5 (b), where the roll-off of the spectrum results from the receiver bandwidth limitation. In this example, the RX bandwidth equals the FSR, $\Delta f_{\text{RX}} = \Delta f_{\text{FSR}}$. Only in the special case, where the emission frequency of the ONU laser is located exactly in the middle of two comb lines, two full copies of the signal spectrum are received.
- III) *Receiver bandwidth* $\frac{1}{2}\Delta f_{\text{FSR}} \leq \Delta f_{\text{RX}} < \Delta f_{\text{FSR}}$. Two partial copies of the signal spectrum are received unless the emission frequency of the DFB laser exactly matches a comb line. From now on, we refer to this receiver as the *limited-bandwidth receiver* (LBW-RX). An exemplary power spectrum at point ② in Fig. 3.4 (c) with a frequency offset of Δf_{IF} is shown in Fig. 3.5 (c). In this example, the RX bandwidth equals half the FSR, $\Delta f_{\text{RX}} = \frac{1}{2}\Delta f_{\text{FSR}}$.

In the DSP block following positions ① and ②, we employ a coarse frequency offset compensation (CFOC) for reducing the frequency offset to a value that can be handled by the subsequent carrier recovery. The CFOC algorithm works as follows: First, we apply a fast Fourier transform (FFT) with a size of 1024 to the time sequence delivered by the previous DSP block. Then we identify the spectral dips (for HBW-RX) or dip (for LBW-RX), which are visible as long as the signal shaping TX filter with bandwidth Δf_{TX} is designed with a sufficiently sharp roll-off. For the HBW-RX, Fig. 3.5 (b), the center frequency between these two dips defines the frequency offset $\Delta f_{\text{IF}}^{(i)}$. For the LBW-RX, Fig. 3.5 (c), we observe a dip at f_{dip} within the frequency range $-\Delta f_{\text{RX}} < f_{\text{dip}} < +\Delta f_{\text{RX}}$, from which we identify the frequency offset $\Delta f_{\text{IF}}^{(i)} = f_{\text{dip}} + \frac{1}{2}\Delta f_{\text{FSR}}$, for $f_{\text{dip}} < 0$, and $\Delta f_{\text{IF}}^{(i)} = f_{\text{dip}} - \frac{1}{2}\Delta f_{\text{FSR}}$, for $f_{\text{dip}} \geq 0$. A sketch of the shifted signal spectrum from Fig. 3.5 (b) at the output of the CFOC at point ③ in Fig. 3.4(a) is shown in Fig. 3.5 (d). The blue power spectra of Fig. 3.5 (e-f) represent the CFOC outputs for *DSP Scheme-II* and *DSP Scheme-III* in Fig. 3.4 (b) and (c), respectively. Chromatic dispersion (CD) compensation can be applied either before or after the CFOC block.

In the following, we discriminate between the three schemes shown in Fig. 3.4. While *DSP Scheme-I* follows the steps of a conventional digital coherent receiver, it requires a HBW-RX. With *DSP Scheme-II*, we introduce an advanced DSP technique, which makes use of all copies of the received signal spectrum. As a result, it improves the signal-to-noise ratio (SNR). Finally, with *DSP Scheme-III*, we introduce another advanced DSP scheme, which features the use of a LBW-RX.

3.4.1 DSP Scheme-I (with 2×2 MIMO)

For this scheme, we restrict the processing to the case illustrated in Fig. 3.5 (d), where a full copy of the data spectrum is received by a HBW-RX. It requires an ADC with an analog bandwidth exceeding the FSR (Δf_{FSR}), i.e., its sampling rate f_{Sa} must exceed $2\Delta f_{\text{RX}}$.

We first remove the redundant partial copies by employing an anti-aliasing filter (AAF) in combination with downsampling to two samples per I and Q symbol after the coarse frequency-offset compensation. In this work, we choose an AAF with a root-raised-cosine (RRC) shaped frequency response and a roll-off factor of 0.02, independently of the TX filter shape. Other filter shapes could be used as well. Figure 3.5 (g) illustrates the power spectrum after the AAF at point ⑥ in Fig. 3.4 (a). Next, we apply a frequency-domain feed-forward timing recovery (TR). More specifically, we estimate the timing error by employing a frequency-domain algorithm proposed by Barton & Al-Jalili, and compensate the timing error by a seventh-order Lagrange interpolation [131, 132]. Afterwards, we use a 2×2 MIMO adaptive equalizer whose coefficients are adapted by the constant modulus algorithm (CMA) [133] to correct for the polarization rotation, to compensate for residual CD, and to mitigate the effect of bandwidth limitations as well as multipath and intersymbol interference in the transceivers [134]. Finally, we apply a carrier recovery (CR) [135] to compensate for the residual frequency offset as well as for laser phase noise using the Viterbi-Viterbi algorithm. We finalize the DSP by demapping and decoding.

3.4.2 DSP Scheme-II (with 6×2 MIMO)

In order to utilize all copies of the received signal spectrum, we introduce advanced *DSP Scheme-II* based on signal tripling, spectral shifting and 6×2 MIMO equalizer, see Fig. 3.4 (b) and Fig. 3.5 (b), (e), and (h). In the first step, we digitally create two copies of the dual-polarization received signal. Next, we simultaneously process this signals in three DSP lanes, namely “blue-lane”, “green-lane”, and “red-lane”. The “blue-lane” operates on original signal delivered by CFOC and the corresponding power spectrum is shown in blue solid line in Fig. 3.5 (e). The adjacent “green-lane” and “red-lane” operate on the digitally create copies, whose spectra are shifted to the right and to the left by $\pm \Delta f_{\text{FSR}}$, respectively. Spectral shifting requires an FSR detection algorithm. Figure 3.5 (e) illustrates

the shifted signal spectra of the “green-lane” and the “red-lane” in green dash-dotted line and in red dashed line, respectively. Next, we apply the same AAF to all three lanes, cutting away unnecessary spectral parts as seen in Fig. 3.5 (h). After downsampling and timing recovery as described in Subsection 3.4.1, a MIMO equalizer adds up the various lanes coherently: The addition of the “red-lane” and the “green-lane” outputs result in an identical signal as delivered by the “blue-lane”, and adding all three lane outputs coherently therefore results in a 2-fold increase of the signal amplitude. In case the noise is uncorrelated, this increases the signal-to-noise ratio (SNR) by a factor of two. However, this requires a receiver with twice the bandwidth.

Each lane processes two polarizations, therefore the 2×2 MIMO equalizer of Fig. 3.4(a) has to be extended to a 6×2 MIMO equalizer in Fig. 3.4(b), which acts as an adaptive maximum ratio combiner [136]. As in *DSP Scheme-I*, the MIMO equalizer also corrects for the polarization rotation and the CD. Finally, the CR algorithm is applied. Notice that the proposed 6×2 MIMO equalizer will only converge if the phase difference $\Delta\phi_{\text{L,LO}}^{(n)}$ (Eq. (2.4) for DS and Eq. (3.9) for US) between neighboring comb lines is only slowly varying in comparison to the symbol rate Δf_{Sym} . Therefore, a coherent frequency comb source, as defined in Subsection 2.2.1.4, is required.

3.4.3 DSP Scheme-III (with 4×2 MIMO)

DSP Scheme-III allows to use intradyne coherent receivers with a minimum bandwidth. The principle is much the same as described in Section 3.4.2, however, only two processing lanes are employed: A digital copy of the data spectrum is created and shifted by either $+\Delta f_{\text{FSR}}$ or $-\Delta f_{\text{FSR}}$. Figure 3.5 (f) shows an exemplary power spectrum at point ⑤ in Fig. 3.4 (c). The sign of this frequency shift is chosen according to the direction of the frequency offset: The spectrum is moved in positive direction for positive frequency offsets, and in negative direction if the frequency offset is negative. The subsequent DSP blocks are identical to the ones used in *DSP Scheme-II*, with the exception that only a 4×2 MIMO

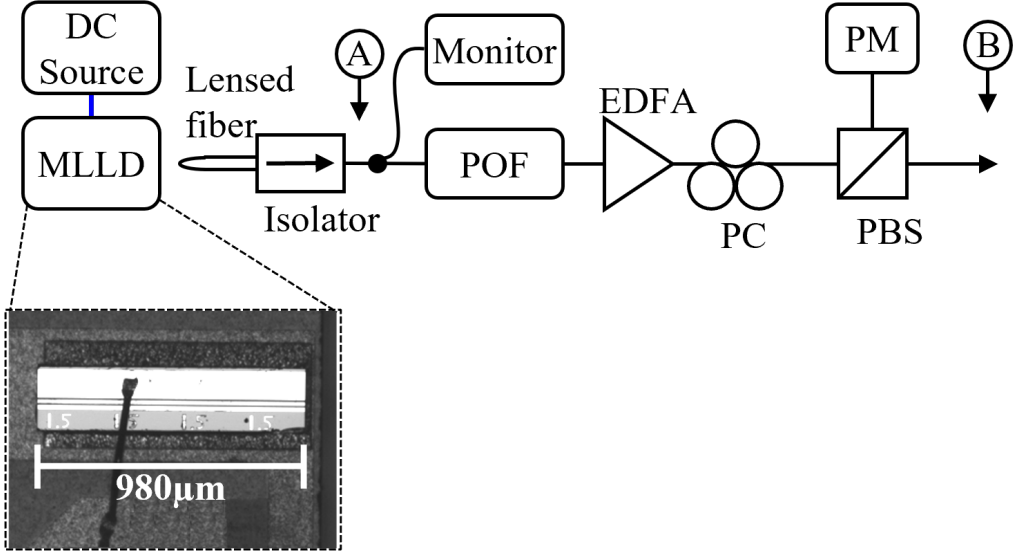


Figure 3.6: Experimental setup of the coherent frequency comb source. A microscope image of the 980- μm -long quantum-dash mode-locked laser diode (MLLD) is shown in the inset [137]. Notice that only a DC current is supplied through the wire bond. The light generated by the MLLD is coupled into a lensed optical fiber. The optical isolator avoids back reflection into the MLLD. We use a programmable optical filter (POF) followed by an EDFA to amplify the signal and to equalize the comb lines at position ②. A polarization controller (PC), a polarization beam splitter (PBS), and a power meter (PM) are used to align the polarization across all comb lines. Point ② is connected with the DP-IQM (downstream) or the CRX (upstream).

equalizer is needed. Figure 3.5 (i), shows the power spectrum after the AAF at point ② in Fig. 3.4 (c). While a detailed analysis of the DSP power consumption is outside the scope of this paper, we would like to point out that we do not expect a significant increase, especially for *DSP scheme-III*, since most of the DSP functionalities remain unchanged.

3.5 Experimental Setups

In order to investigate the feasibility of the proposed colorless coherent TDM-PON architecture, we set up two experiments, one for downstream operation

and another one for upstream operation. There are several options for frequency comb laser sources, such as Erbium glass oscillator (ERGO) lasers, electro-optic modulators, Kerr microresonators, and mode-locked laser diodes (MLLD). In our experiment, we use an MLLD as a frequency comb source. Figure 3.6 shows the experimental setup for generating a flat-top coherent frequency comb. The MLLD is $980\text{ }\mu\text{m}$ long. Its light is outcoupled by a lensed fiber. With the help of integrated optics, a more stable and accurate coupling can be realized by using 3D printed waveguides or free-form coupling elements for hybrid photonic or flip-chip coupling technology [138–140]. Next, we employ an optical isolator to avoid back reflections into the MLLD. At room temperature and with a DC current of 180 mA, we measure an optical power of 5 dBm at position ① in Fig. 3.6. Figure 3.7(a) shows the power spectrum measured at position ① in Fig. 3.6. The measured 3 dB bandwidth is 1.42 THz and the FSR is 25.0812 GHz at room temperature with a DC current of 180 mA. Note that we do not utilize any temperature controller to stabilize the output signal of the MLLD in our experiment. As a monitor we employ an optical power meter (PM) and a 43 GHz photodiode followed by an electrical spectrum analyzer (ESA). The ESA allows to measure the RF beat signal of the comb lines. The generated frequency comb is spectrally flattened with a programmable optical filter (POF, Finisar waveshaper 4000s) and reduced to a desired number of comb lines, which are then amplified with an EDFA. With the polarization controller (PC) and a polarization beam splitter (PBS) we set the correct polarization state so that we can efficiently couple into the polarization maintaining fiber. Figure 3.7 (b-c) shows the flattened comb spectrum of 20 and 40 lines at position ② in Fig. 3.6, respectively. As can be seen in the figure, the peak power variation is about $\pm 0.5\text{ dB}$ in both cases, except for a single comb line in case of 40 lines in Fig. 3.7(c). Note that 20 and 40 lines correspond to bandwidths of 0.5 THz and 1.0 THz, respectively. The measured output power of the spectrally flattened comb at position ② in Fig. 3.6 is 16 dBm for all cases. Next, we modulate all comb lines with a LiNbO_3 DP-IQM, driven by a four-channel arbitrary-waveform generator (AWG, 120 GSa/s, Keysight M8194A). The test patterns consist of two uncorrelated pseudo random sequences of 2^{15} QPSK symbols, which are over-sampled, and then shaped by

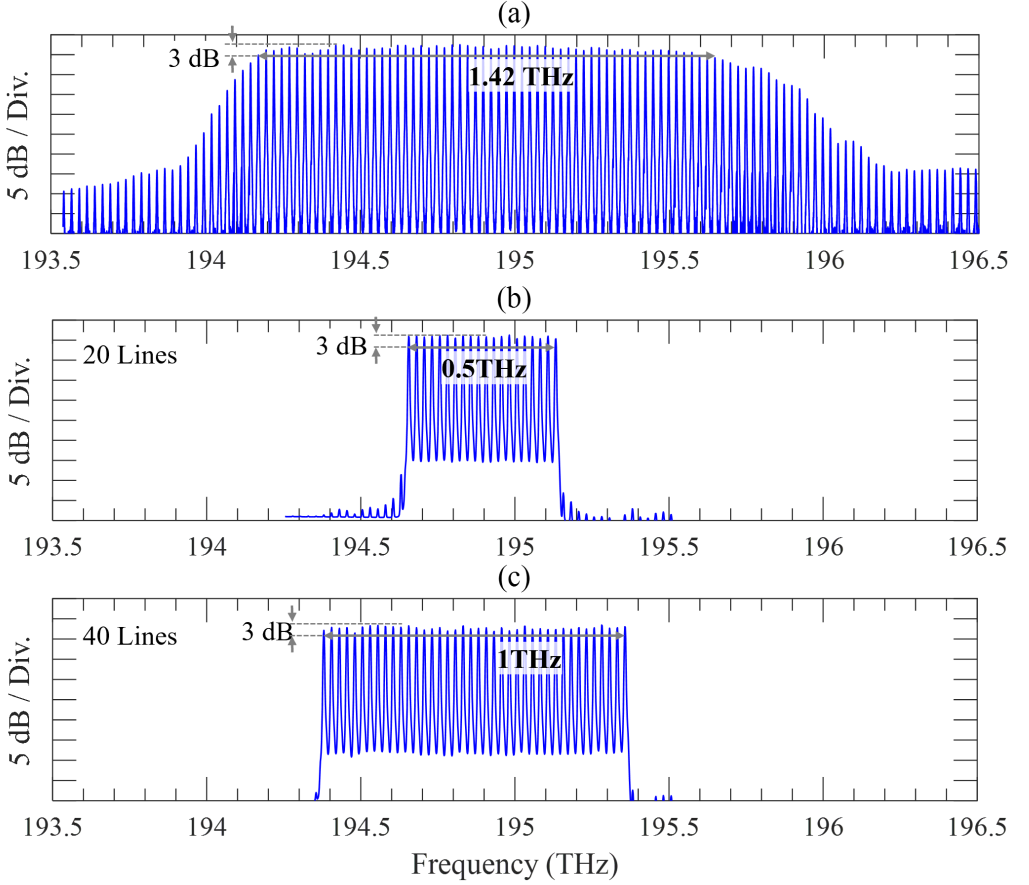


Figure 3.7: Optical spectra of the frequency comb source measured in a resolution bandwidth of 2 GHz. (a) Optical spectrum measured at position ① in Fig. 3.6 for a DC current of 180 mA. We find a 3-dB bandwidth of 1.4 THz and an FSR of 25.0812 GHz. The optical power coupled into the lensed-fiber is 5 dBm. (b) Optical spectrum measured at position ② in Fig. 3.6. With the POF we filtered out 20 comb lines and equalized them to within about ± 0.5 dB. (c) Corresponding optical spectrum for 40 comb lines.

a pulse-shaping filter exhibiting a RRC spectrum. The FSR of the coherent frequency comb generated with the MLLD is 25.0812 GHz and limits the symbol rate to 24 GBd when considering a sharp roll-off of 0.02 for the RRC pulse shaping. With a frequency comb with slightly higher FSR, symbol rate can easily be scaled to 25 GBd, resulting in a bit rate of 100 Gbit/s. In the downstream case, the modulated signal is amplified with a booster EDFA, resulting in the comb spectrum depicted in Fig. 3.8 (a) measured at position ③ of Fig. 3.2. We attribute the power drop at high frequencies to a gain tilt of the EDFA. Figure 3.8 (b) provides a closer look into the modulated spectrum.

In an optical back-to-back setting, we vary the received power with a variable optical attenuator (VOA). For our fiber nonlinearities experiment, we employ 25 km of standard single-mode fiber (SSMF) that along with the VOA emulates the ODN. In that case, the launch power into the fiber is controlled by a concatenation of two booster amplifiers (instead of only one in optical back-to-back) followed by another VOA. At the ONU side, we receive the optical signal with an integrated coherent receiver (ICR, Neophotonics, OIF Type II). The ICR features a bandwidth of more than 25 GHz, which is larger than the FSR (HBW-RX, compare Subsection 3.4.1 and Subsection 3.4.2). Thus, we have to emulate the case of an LBW-RX (Subsection 3.4.3) by applying a digital low-pass filter with a bandwidth of 13 GHz and a roll-off of 0.3 at the beginning of our DSP chain. In addition, due to a limited number of available devices in our laboratory, we set up only one ONU transmitter and receiver. However, we mimic different ONUs by sweeping the ONU laser frequency. We use a 3 dB power splitter and a power meter to measure the received optical power impinging on the coherent receiver. In our experiments, we measure the receiver sensitivity for two different types of LOs, one being a DFB laser emitting at ~ 194.68 THz (~ 1540.00 nm) and the other being a narrow-linewidth tunable ECL. Our setup allows us to tune the ONU LO frequency over the full bandwidth of the frequency comb (1.05 THz) even if 40 lines are used.

For upstream, the experimental setup is modified as follows: The DFB laser, or alternatively the ECL, is used as the transmit laser at the ONU side, whereas the

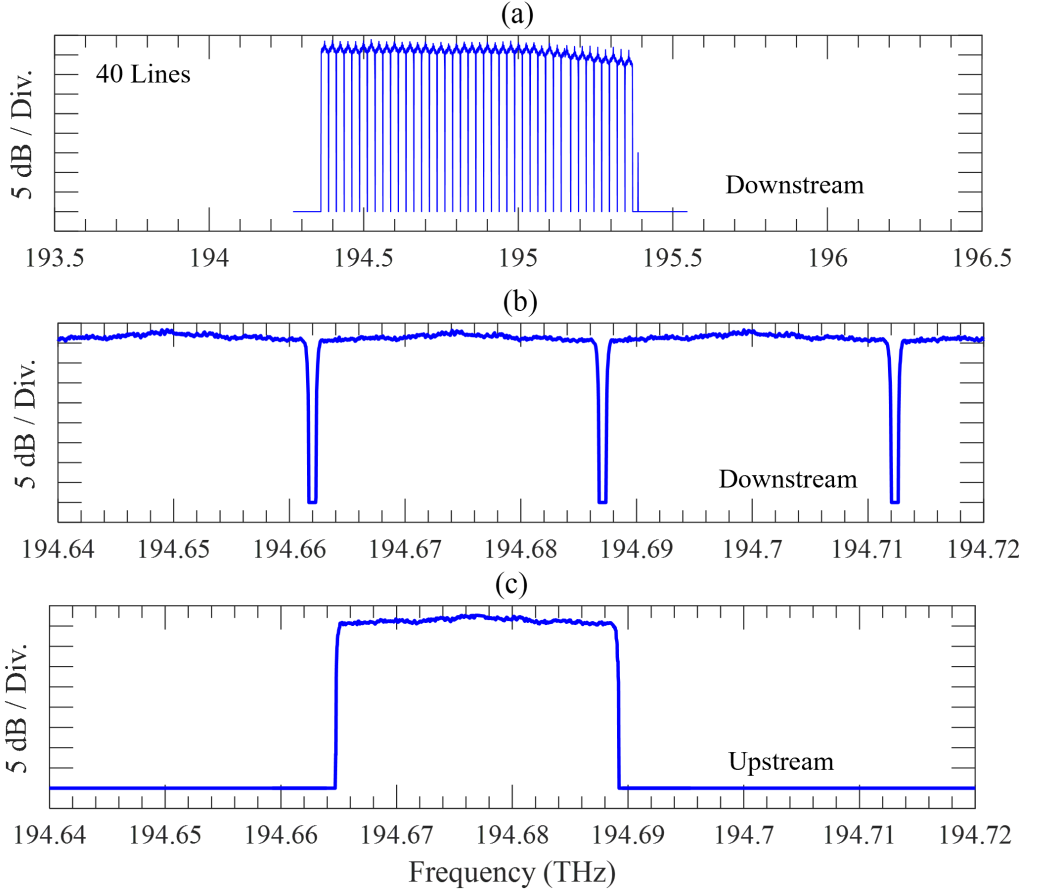


Figure 3.8: Modulated optical spectra for both US and DS operation. (a) Optical comb spectrum modulated with a 24-GBd QPSK signal, spectrally shaped with a root-raised-cosine (RRC) filter having a roll-off of 0.02, measured at position ② in Fig. 3.2. Towards higher frequencies, we observe the effect of a reduced gain of the EDFA following the modulator. (b) Same as (a) but plotted over a narrower frequency range. (c) Optical spectrum of the modulated output of a DFB laser centered at 194.68 THz measured at position B in Fig 3.3. The resolution bandwidth is 180 MHz in all measurements shown in the figure.

same DP-IQM as for the downstream is used. The measured upstream signal at position ⑥ of Fig. 3.3 for an exemplary ONU laser frequency of ~ 194.68 THz is shown in Fig. 3.8 (c). The received optical signal is pre-amplified using an EDFA at the OLT side. Note that we do not employ an optical filter for removing out-of-band ASE noise, since we want to demonstrate a wide variation of the ONU wavelengths. The frequency comb generated by the MLLD acts as an LO and allows the ONU laser frequency to drift over the entire comb. For reception, we use the same ICR as for the downstream.

In both experiments, we use a four-channel real-time oscilloscope with a sampling rate of 256 GSa/s and a realtime bandwidth of 80 GHz to capture the outputs of the ICRs. Afterwards, offline digital-signal processing algorithms are applied to the recorded waveforms, see Section 3.4 for details. As a final step, the bit error ratio (BER) is estimated by evaluating 2^{19} bit.

3.6 Experimental Results

3.6.1 Downstream Colorless Coherent PON

First, we investigate the downstream operation in a back-to-back configuration. As described before, see Section 3.3.1 and Fig. 3.2, a frequency comb generated by an MLLD is used as the transmit laser at the OLT, whereas the LO at the ONU is provided by a DFB laser. At the transmitter, we use the POF to select 20 or 40, respectively. The output power of the booster EDFA is set to a constant value of 8 dBm. As a result, the transmit power per line is reduced by a factor of 20 if 20 comb lines are considered and by a factor of 40 if 40 comb lines are used. The received optical power is swept by tuning a VOA.

In a first experiment, we characterize the ONU receiver. To this end, we measure the BER when sweeping the total received power (including all transmitted comb lines) by tuning a VOA, see in Fig. 3.9. The blue, green and red colors represent the BER obtained with *DSP Scheme-I*, *DSP Scheme-II* and *DSP Scheme-III*,

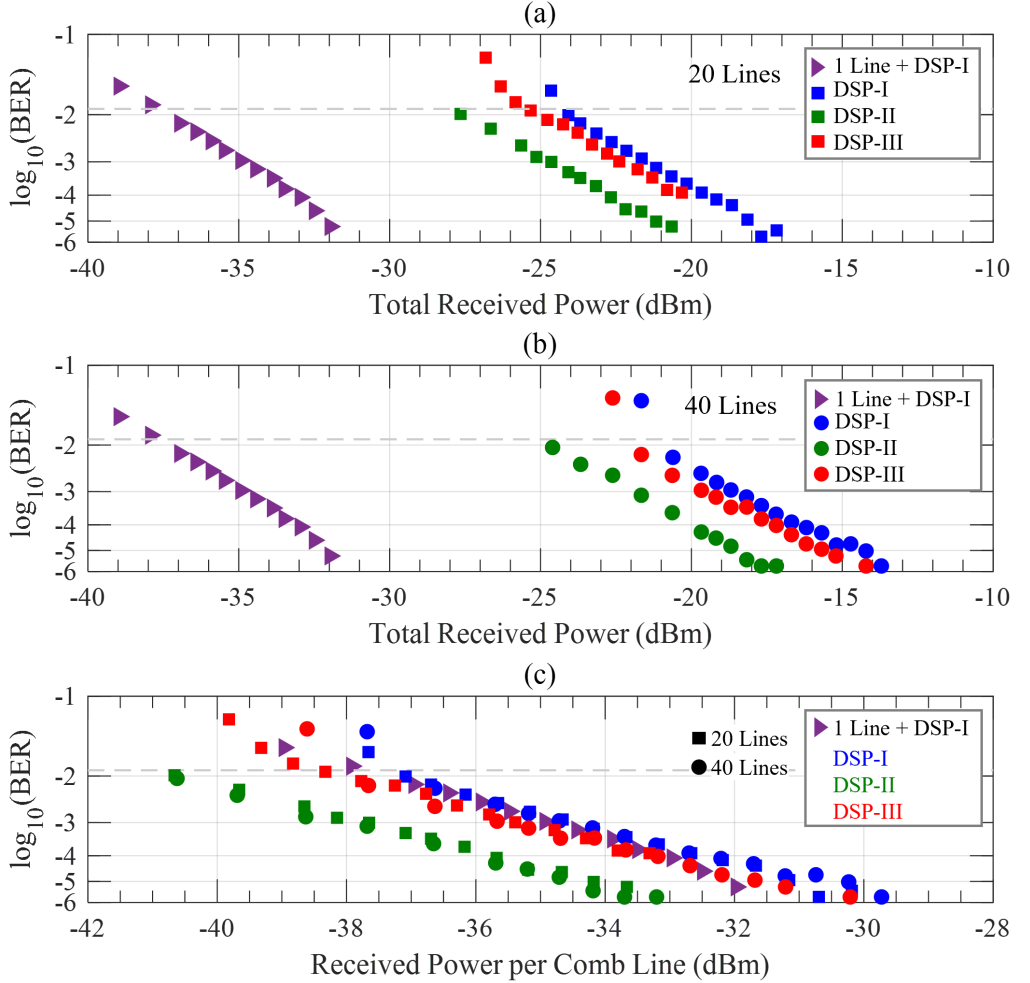


Figure 3.9: Downstream operation. Measured BER for the three DSP schemes shown in Fig. 3.4. Here, blue, green, and red colors represent values obtained with *DSP schemes I, II and III*, respectively. As a reference, purple triangles represent the values for a single-line ECL and the DSP scheme I. The BER is plotted as a function of the total optical power received at the ONU for (a) 20 comb lines, and for (b) 40 comb lines. The LO is a DFB laser for all measurements. (c) BER from (a) and (b) plotted as a function of the received optical power per comb line.

respectively. Furthermore, the square and the circle symbols illustrate the BER for 20 comb lines (see Fig. 3.9(a) and (c)) and for 40 comb lines (see Fig. 3.9 (b) and (c)). As a reference, we also measure the BER by using a single ECL as transmitter laser, see purple triangles in Fig. 3.9. The evaluation is first done with *DSP Scheme-I* employing a 2×2 MIMO equalizer, see blue symbols in Fig. 3.9(a)–(b). Considering a BER threshold of 1.25×10^{-2} for a forward error correction (FEC) code with 15% overhead [141], we observe receiver sensitivities of (leading to loss budgets of) -38 dBm (46 dB), -24.5 dBm (32.5 dB), and -21.5 dBm (29.5 dB) for the case of a single ECL, for 20 comb lines, and for 40 comb lines used in the OLT transmit laser, respectively. When replacing the DFB laser used as LO at the ONU by a low-linewidth ECL and when repeating the same experiment, we do not observe a substantial performance degradation. This indicates that phase noise is none of the dominant system limitations, because the linewidth of the DFB laser is already sufficiently low.

Next we evaluate the measured data with our proposed DSP schemes (*DSP Scheme-II*), and compare the results with the conventional procedure (*DSP Scheme-I*). The outcome is depicted with green symbols in Fig. 3.9(a)–(b). This time, we restrict our investigation to the case of a DFB laser as an LO, but again compare two different transmitter scenarios: 20 comb lines (Fig. 3.9 (a)), and 40 comb lines (Fig. 3.9 (b)). In both cases, we observe a 3 dB improvement of the receiver sensitivity and of the loss budget when replacing *DSP Scheme-I* by *DSP Scheme-II* for an HBW-RX. This improvement results from an SNR increase by 3 dB, when using the energy contained in the partial copies of the received spectrum, see Section 3.4.2.

We then assume an LBW-RX ($\frac{1}{2}\Delta f_{\text{FSR}} \leq \Delta f_{\text{RX}} < \Delta f_{\text{FSR}}$) and repeat our evaluation (with *DSP Scheme-III*). For this purpose, we apply a digital low-pass filter and artificially reduce the double-sided bandwidth of our receiver to 13 GHz. Comparing the receiver sensitivity obtained for *DSP Scheme-I* with the one achieved by processing according to *DSP Scheme-III*, we find a performance improvement of 0.5 dB (see red symbols in Fig. 3.9(a)–(b)). We attribute this gain to the extra signal power that is contained in the additional partial copy of the data spectrum

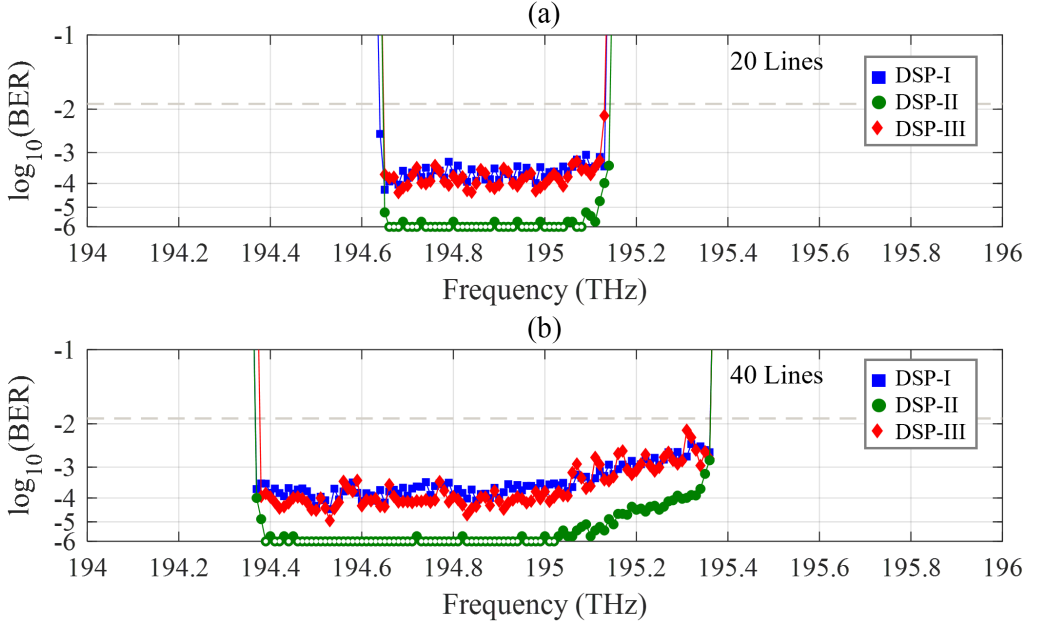


Figure 3.10: BERs measured when the LO generated by an ECL is swept over frequency for (a) 20 and (b) 40 comb lines, corresponding to an LO frequency (wavelength) variation of ± 0.25 THz (± 2 nm) or ± 0.5 THz (± 4 nm), respectively. The open symbols indicate that no bit errors.

($\Delta f_{\text{RX}} > \Delta f_{\text{TX}}$) which is taken into account when applying the 4×2 MIMO equalizer, see Section 3.4.3.

The results presented so far show that the receiver sensitivity scales in proportion to the number of comb lines. This becomes even more visible in Fig. 3.9(c), where the BER for 20 and 40 comb lines as a function of the received power per comb line nicely coincide. The BER obtained with a single-line ECL transmitter laser is again plotted for comparison.

As described in Section 3.2, our proposed colorless coherent TDM-PON architecture aims at solving the challenge of matching the transmitter frequency with the corresponding receiver LO frequency. To demonstrate that we can cope with substantial manufacturing tolerances and temperature-induced wavelength drifts of the DFB lasers used in the ONUs, we investigate the system performance when tuning the LO frequency over the full bandwidth of the comb spectrum. Since

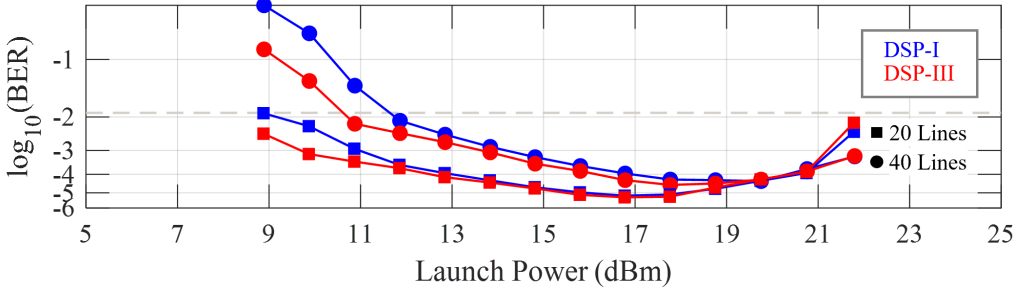


Figure 3.11: BER as a function of the launch power into a 25 km SSMF followed by 25 dB additional ODN loss. The circled and squared symbols represent the transmit laser consisting of 20 and 40 comb lines, respectively. A DFB laser is used as a LO. The blue color represents *DSP Scheme-I* and the red color represents *DSP Scheme-III*.

DFB lasers are not tunable over frequency ranges in the order of 1 THz and a large enough sample of differently emitting DFB lasers was not available, we employed a tunable ECL as an LO. This choice reflects real-world BER results because we already showed the equivalence of ECL and DFB laser as an LO.

The results of our experiments are summarized in Fig. 3.10 for a received power of -20 dBm in the case of 20 comb lines (Fig. 3.10(a)), and a received power of -17 dBm in the case of 40 comb lines (Fig. 3.10(b)). As before, the blue, the green, and the red color represent *DSP Scheme-I*, *II*, and *III*. Open symbols indicate that no errors could be detected in the recorded data. For all cases, we measure a BER that is below the 15 % FEC limit. The slight increase of the BER towards higher frequencies, Fig. 3.10 (b), is caused by a gain tilt of the booster amplifier. The experimental results confirm that our TDM-PON architecture can tolerate LO frequency (wavelength) variations at the ONU of ± 0.25 THz (± 2 nm) if 20 comb lines are used and ± 0.5 THz (± 4 nm) if 40 comb lines are used.

Finally, we investigate the proposed architecture in the presence of fiber nonlinearities. To this end, we slightly modify the experimental setup. We insert 25 km of standard single-mode fiber (SSMF) and set the subsequent VOA to a constant attenuation of 25 dB to emulate the loss of the passive splitter. This leads to an accumulated loss of about 30 dB, which is a typical number for ODN losses in PONs. To control the launch power going into the SSMF, we deploy a second

booster EDFA and another VOA in front of the fiber. We measure the BER for various launch powers to find the optimum operating point of the system, see Fig. 3.11. The optimum launch power is 17 dBm and 20 dBm for 20 comb lines and 40 comb lines, respectively. The 3 dB difference is due to the 3 dB reduction of the launch power per comb line in the case of 40 comb lines.

3.6.2 Upstream Colorless Coherent PON

For upstream operation, we first investigate the receiver sensitivities. For the evaluation of the received data, we use *DSP Scheme-I* with a 2×2 MIMO equalizer. According to Section 3.4.1 and Fig. 3.3, a DFB laser is used as the transmit laser in the ONU, while a frequency comb acts as the LO in the OLT. Similar to downstream operation, the received power is swept by tuning a VOA. We select either 20 or 40 comb lines for the LO and compare the system performance for both cases, see Fig. 3.12 (a)–(b). We plot the BER as a function of the received power measured at the input of the OLT pre-amplifier. The total LO power is kept constant at 16 dBm so that the LO power per comb line decreases with an increasing number of lines used. As a reference, we also measure the BER for a single-line ECL as an LO, see purple labels in Fig. 3.12.

Furthermore, we repeat the measurements when replacing the DFB transmit laser by an ECL and observe an improvement by 0.5 dB, which we attribute the optical carrier-to-noise power ratio (OCNR) which is better by 0.5 dB compared to the DFB laser. For the DFB as a transmit laser, we find receiver sensitivities of -43.5 dBm (ECL as LO), -29.5 dBm (20 LO comb lines), and -26 dBm (40 LO comb lines) at the 15 % FEC limit (see Fig. 3.12(a)-(b)). The differences mainly result from the reduction of the power per LO laser line by a factor of 20 (40) if 20 (40) comb lines are used as LO. We attribute the additional penalty of 1 dB to a reduced OCNR and accumulated LO-ASE beat noise, see Section 3.3.2. Finally, we confirm a negligible BER penalty in comparison with ECL and 1 line MLLD LO and conclude that the laser phase noise is sufficiently low.

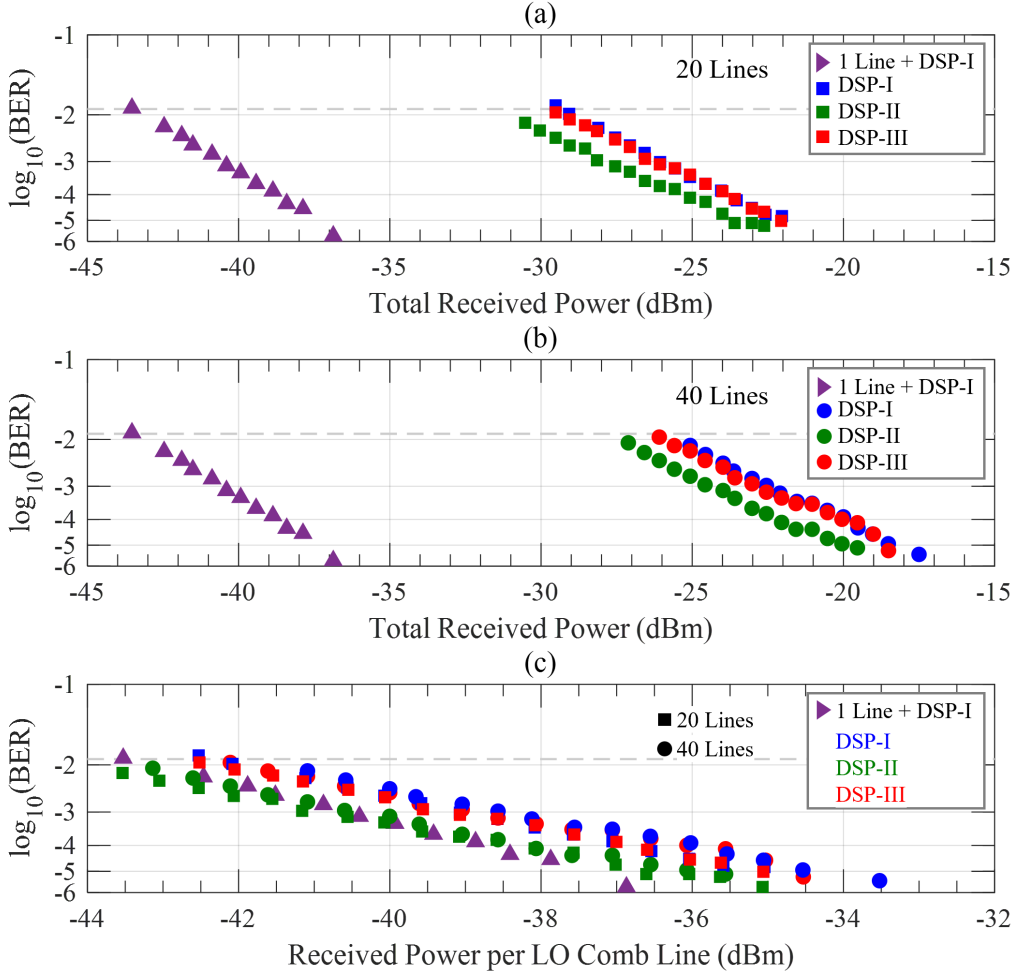


Figure 3.12: Upstream operation. Measured BERs for the three DSP schemes shown in Fig. 3.4. Blue, green and red colors represent *DSP schemes I, II, and III*, respectively. Purple triangles represent the back-to-back measurement using an ECL LO and conventional coherent DSP. The BER is plotted as a function of the total optical power received at the OLT for (a) 20 comb lines, and (b) 40 comb lines. (c) BER plotted as a function of the received optical power per LO comb line considering 20 and 40 comb lines.

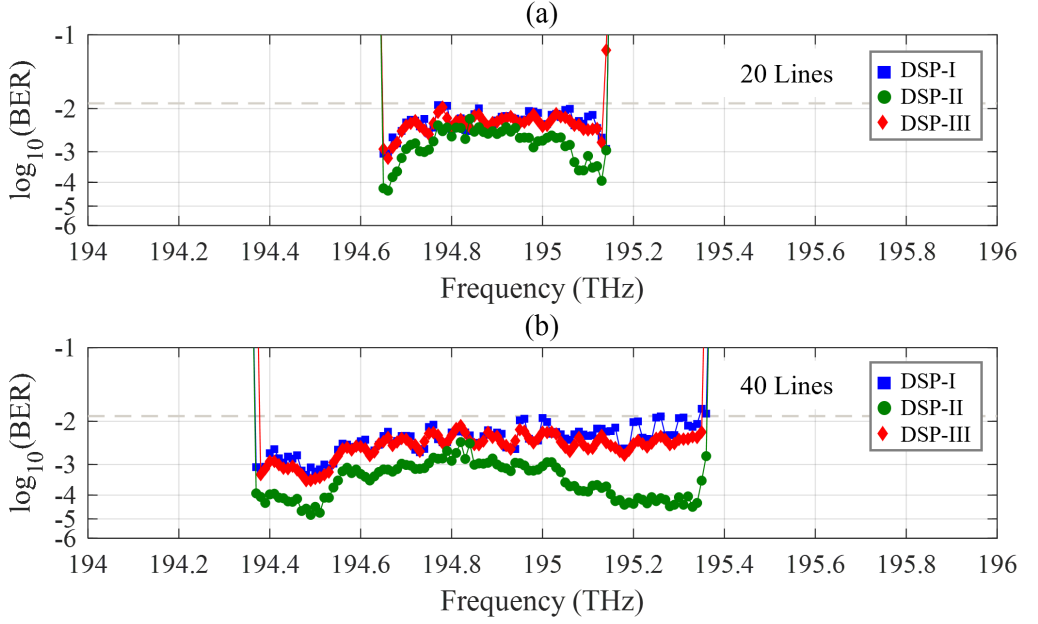


Figure 3.13: BER obtained while tuning the center frequency of the ONU transmit laser and using either (a) 20 or (b) 40 comb lines as LO. These two cases mimic a transmit laser frequency variation of ± 0.25 THz (± 2 nm) and ± 0.5 THz (± 4 nm), which can occur due to fabrication constraints and temperature drift.

In another evaluation, we again compare the proposed DSP schemes (*DSP Scheme-II and III*) with the conventional DSP processing (*DSP Scheme-I*). The results are depicted in Fig. 3.12. As for the downstream operation, we restrict our BER analysis to the case of a DFB laser at the ONU, but compare the results for an LO with 20 lines (Fig. 3.12 (a)), and with 40 lines (Fig. 3.12 (b)). Moreover, the BER achieved for an LO consisting of a single ECL line is plotted in purple triangles as a reference. The blue, green and red symbols correspond to *DSP Scheme-I, II, and III*, respectively. For an HBW-RX, we observe a substantial performance improvement when employing *DSP Scheme-II*. We find an improvement of 2.5 dB for 20 comb lines (see green square symbols in Fig. 3.12 (a)), and an additional improvements of 2.0 dB for 40 comb lines (see green circle symbols in Fig. 3.12 (b)). Compared to downstream operation, the improvement is less because of (partially) coherent LO-ASE beat noise within the neighboring signal bands (compare Fig. 3.9(a)-(b) with Fig. 3.12(a)-(b)). For the LBW-RX

emulated by digital low-pass filtering of the ICR output signal, we find the same 0.5 dB receiver sensitivity gain as for downstream, when replacing *DSP Scheme-I* by *DSP Scheme-III* (see red symbols in Fig. 3.12 (a)-(b)). As explained before, this improvement results from the additional signal power that is contained in the received spectrum and that can be extracted with *DSP Scheme-III*, but not by the conventional 2×2 MIMO processing.

In Fig. 3.12 (c), we plot the measurement results as a function of the received power per LO comb line. The results indicate a negligible penalty of 1 dB compared to using a single ECL line as an LO. The penalty is increasing for higher received powers. This penalty is again caused by accumulated LO-ASE beat noise.

Finally, we emulate the wavelength variation of the ONU laser by tuning an ECL over the full bandwidth of the LO comb. As only a slight performance degradation (0.5 dB because of reduced OCNr) has been obtained with a DFB transmit laser compared to the ECL, we expect the results to be representative for a typical low-cost PON transmit laser. The results of the wavelength sweep are depicted in Fig. 3.13. For 20 (40) comb lines and at a received power of -28 dBm (-25 dBm), the BER stays below the 15 % FEC limit over the entire comb bandwidth of 0.5 THz (1 THz). We attribute the variations in the BER largely to imperfect per-line power equalization of the LO and the gain tilt of the pre-amplifier EDFA.

In conclusion, we confirmed that the proposed colorless coherent TDM-PON architecture tolerates strong ONU lasers frequency (wavelength) variations even in the more challenging upstream scenario.

3.7 Summary

Due to the growing amount of data traffic, it is to be expected that passive optical networks need to support data rates of 100 Gbit/s or more in the near future. Such high data rates can be achieved by employing DP-QM and coherent receivers at

the OLT as well as at the ONUs. On the one hand, coherent receivers require local oscillators that are precisely matched with the transmit lasers, which makes wavelength-stable and low-linewidth lasers the technology of choice. On the other hand, it is preferable to use low-cost DFB lasers in the ONUs because of the omnipresent economic constraints in access networks. DFB lasers in turn are subject to temperature-induced wavelength drifts and are manufactured in processes that can lead to significant wavelength variations of up to ± 4 nm from batch to batch. This dilemma is solved by our proposed colorless coherent TDM-PON architecture, which to the best of our knowledge is the first of its kind. It relies on a frequency comb laser at the OLT, which greatly relaxes the requirements for the wavelength accuracy and stability of the lasers in the ONUs. Furthermore, it avoids the need for LO wavelength matching between ONU and OLT lasers because the wavelength of the DFB lasers used in the ONUs can vary or drift within the entire comb bandwidth without causing a substantial performance penalty. We demonstrate error-free colorless coherent upstream and downstream operation over a wide bandwidth of 1 THz (± 4 nm) at an aggregated line rate of 96 Gbit/s. In addition, we report on an advanced DSP scheme based on Signal Tripling & Spectral Shifting after a coarse frequency offset compensation and a 6×2 MIMO equalizer. These measures improve the receiver sensitivity by 3 dB. Finally, we propose a DSP scheme based on a 4×2 MIMO equalizer, which works equally well for low-bandwidth receivers. We believe, that frequency comb laser sources have the potential to become a key building block in integrated burst-mode coherent receivers.

End of Journal [1]

4 Coherent TWDM-PON

This chapter explores the feasibility of achieving 200 Gbit/s coherent time- and wavelength-division multiplexed point-to-multipoint optical access networks using a frequency comb laser in the OLT and a low-cost thermally tuned laser on the ONU side. Furthermore, we study the burst-mode operation for coherent PON and introduce a unique burst-mode digital signal processing chain to address a few burst-mode challenges. This chapter is based on a journal publication [2], which was published in *Optics Express*. The material from the publication is reproduced here with the appropriate changes to fit the structure and notation of this thesis.

Start of journal [2]

Copyright © 2024 Optica Publishing Group under the terms of the Optica Open Access Publishing Agreement

Coherent time- and wavelength-division multiplexed point-to-multipoint optical access network using low-cost DFB lasers enabled by a frequency comb

Optics Express, Volume: 32 Issue: 22 pp. 38516-38530

DOI: doi.org/10.1364/OE.531344

Md Mosaddek Hossain Adib^{1,2}, Christoph Füllner^{1,2}, Huanfa Peng¹, Christian Koos¹, Wolfgang Freude¹, and Sebastian Randel¹

¹ Institute of Photonics and Quantum Electronics (IPQ), Karlsruhe Institute of Technology (KIT), Germany

² Nokia Bell Labs, Stuttgart, Germany

Coherent reception, along with time- and wavelength-division multiplexing (TWDM), is a promising concept to simultaneously support multiple services in future high-speed point-to-multipoint passive optical networks (PONs). The Next-Generation PON 2 (NG-PON2) standard describes a TWDM-PON based on IM/DD intensity modulation and direct detection (IM/DD) which employs tunable-lasers and optical filters such as tunable optical filters or cyclic arrayed-waveguide gratings. Here, we investigate a novel coherent TWDM-PON architecture based on a frequency comb source in the optical line terminal (OLT), and thermally-tuned distributed-feedback (DFB) lasers in the optical network units (ONUs). For downstream operation, we broadcast multiple copies of two 25 GBd dual-polarization quadrature phase shift keying (DP-QPSK) signals, resulting in a total PON downstream capacity of 200 Gbit/s. The copies of the downstream signals are spanning ± 2 nm (± 250 GHz). In the ONUs, we align the wavelengths of the DFB lasers, which act as local oscillators (LOs), to one of the downstream signals by a thermal heater or by changing the direct current. In upstream, the already aligned DFB lasers act as transmit lasers and the frequency comb as LO. We demonstrate TWDM upstream by emulating two ONUs with 25 GBd DP-QPSK, resulting in a total PON upstream capacity of 200 Gbit/s.

4.1 Introduction

Initially, passive optical networks (PONs) have been designed to provide high-speed fiber-to-the-home (FTTH) connectivity based on time-division multiplexing (TDM) in downstream and time-division multiple access (TDMA) in upstream[142]. In the future, PONs will need to support multiple services simultaneously and those services will have diverse requirements in terms of data rate, reliability, latency, and cost [95]. Therefore, the future PON might require high data rate (e.g., >100 Gbit/s) along with time- and wavelength-division multiplexing (TWDM) in downstream and time- and wavelength-division multiple

access (TWDMA) in upstream to address these diverse service requirements. Currently, the ITU-T SG15/Q2 is analyzing different technology options as part of the very-high speed PON supplement project, G.sup.VHSP, in which line rates in the range of 100 Gbit/s to 200 Gbit/s along with various multiplexing technique are analyzed [86]. Regarding other ongoing standardization activities in the ITU for TWDM-PON we refer the reader to the following references[143, 144]. The Next-Generation PON 2 (NG-PON2) is based on TWDM and TWDMA technology and it supports four wavelength channels with a total rate of 40 Gbit/s [68, 69, 105], can multiplex different services to distinct wavelength windows and transmit them over the same optical distribution network (ODN). NG-PON2 relies solely on intensity modulation and direct detection (IM/DD) [145]. In principle, these techniques get along with simple and low-cost optics. However, in the specific case of NG-PON2, tunable optical filters are required in the optical network units (ONUs) to detect the desired signal and tunable distributed-feedback (DFB) lasers are needed to select the relevant wavelength of the upstream signal [68, 69, 146]. The NG-PON2 architecture is not readily compatible with coherent reception, which will likely be required for next generation TWDM-PON [147, 148].

Coherent reception provides frequency selectivity without the need for tunable optical filters in the ONUs. It offers a high receiver sensitivity and allows electronic chromatic dispersion (CD) compensation [149]. However, coherent receivers require a wavelength-stable local oscillator (LO), whose wavelength is closely matched to the transmit laser [129]. The tolerable frequency offset does typically not exceed a few GHz hence imposing a strict requirement on the wavelength accuracy for intradyne reception. In this work, we consider that the tunable narrow-linewidth lasers with wavelength locker are prohibited in PONs for techno-economic reasons [66]. It is an important feature of our architecture that it allows the use of low-cost DFB lasers in ONUs. However, at a given temperature, the wavelength of DFB lasers can vary over a span of about ± 2 nm due to imperfections in the laser fabrication process [122, 125]. On top of that, they exhibit a temperature-induced wavelength drift of 0.1 nm/ $^{\circ}$ C (20 $^{\circ}$ C-50 $^{\circ}$ C)

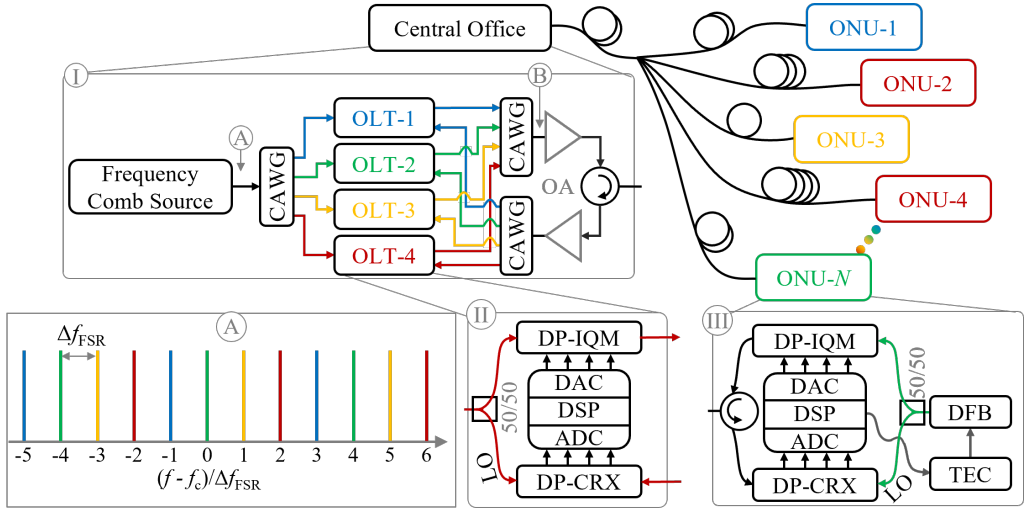


Figure 4.1: Architectural vision of the proposed coherent TWDM-PON. Inset ① illustrates the architecture of the central office that makes use of a frequency comb source which is shared for shared upstream and downstream. Inset ② illustrates the corresponding optical spectrum at position ②. Inset ③ shows the architecture of an OLT transceiver and inset ④ shows the design of the ONU transceiver.

[122]. Moreover, their wavelength can only be tuned over a limited-range (e.g. 2 nm) either by employing a thermal heater or by changing the direct current, or a combination of both without introducing additional penalties in terms of laser linewidth, relative intensity noise, and optical power [125].

In [91, 150], a coherent dense wavelength-division multiplexing (DWDM) PON was demonstrated employing an integrated tunable laser assembly (ITLA) in the ONUs, which will presumably not meet the cost requirement of PONs. In [151], on the other hand, a 10 Gbit/s coherent TWDM-PON was demonstrated utilizing a reflective electro-absorption modulator (R-EAM) at the ONU and a DFB-LO at the optical line terminal (OLT). However, IM/DD-based TWDM PON requires a tunable optical filter in the ONU. In [1], we proposed a TDMA-PON using an optical frequency comb source at the OLT, which allows the use of low-cost DFB lasers in the ONUs while providing a solution for the wavelength-matching problem. However, our proposed scheme [1] does not support wavelength-division multiplexing, which might be required in future

TWDM-PON to allow for simultaneous operation of multiple services. In this work, we extend our TDM-PON approach to the wavelength dimension and propose a novel coherent TWDM-PON. Initial results for downstream operation have been presented in [20]. The proposed architecture employs a cyclic arrayed waveguide grating (CAWG), a frequency comb source in the OLT and DFB lasers in the ONUs. We experimentally demonstrate a 200-Gbit/s TWDM-PON, which tolerates a loss budget of over 37 dB in downstream and 24 dB in upstream and which can tolerate an ONU-wavelength variation of up to ± 2 nm (± 0.25 THz).

4.2 Coherent TWDM-PON using a frequency comb source as OLT laser

4.2.1 Coherent TWDM-PON architecture

The architectural vision of the proposed coherent TWDM-PON is sketched in Fig. 4.1. It shows an optical access network interconnecting multiple OLTs in a central office to multiple ONUs via an ODN consisting out of bidirectionally operated single-mode fiber and a passive splitter. Groups of multiple comb lines, differentiated by color, each carry a signal which interconnects either a single user or a subset of users to the central office using a TDM scheme with dynamic bandwidth allocation. Multiple of these groups can be simultaneously run on the same ODN, thereby realizing a TWDM-PON.

Inset-① in Fig. 4.1 shows the proposed hardware architecture in the central office. Key element is the frequency comb source, which generates N_{comb} optical carriers (comb lines) with a fixed spacing, referred to as free spectral range (FSR) Δf_{FSR} , thereby covering a bandwidth of $\Delta f_{\text{comb}} = N_{\text{comb}} \Delta f_{\text{FSR}}$ around the optical center frequency f_c . An exemplary optical spectrum at the output of the frequency comb source is sketched in Inset-②. In this example, the output of the frequency comb source is split into four groups of wavelengths by a first cyclic arrayed-waveguide grating (CAWG). For each group, we consider a separate OLT sharing its group

of comb lines for generating the optical downstream signal and acting as the LO for coherently receiving the upstream signal. Inset-[\(II\)](#) in Fig. 4.1 shows the OLT transceiver design. For downstream, a group of comb lines is modulated by the same downstream signal using a dual-polarization inphase-quadrature modulator (DP-IQM). Notice that each comb line carries the same information. The data are provided by an application-specific integrated circuit (ASIC) that includes four digital-to-analog converters (DACs), transmit DSP, and an appropriate client interface. The downstream signals from different OLTs are combined using a second CAWG. Subsequently, an optical amplifier (OA) is used to boost the aggregated transmit signal prior to transmission over the ODN and reception in the ONUs. Details of the ONU transceiver design are shown in Inset-[\(III\)](#) of Fig. 4.1. First, the downstream signal is separated from the upstream signal by an optical circulator (OC). The downstream signal is received (continuous mode) using a dual-polarization coherent receiver (DP-CRX). A DFB laser is shared as LO and as transmit laser. The ONU ASIC includes four DACs, four analog-to-digital converters (ADCs) as well as DSP, and a client interface for both up- and down-stream operation. Wavelength alignment between downstream signal and the ONU LO is an important topic, which will be discussed in detail in section-4.2.2. For upstream operation, the analog burst-mode signals are modulated onto the output of the DFB laser using an DP-IQM. In the central office, the aggregated upstream signal is optically isolated from the downstream signal by an OC and pre-amplified using another OA, see Inset-[\(I\)](#) in Fig. 4.1. Next, the wavelength groups are separated with a third CAWG. In each OLT, the respective upstream signal is detected using a burst-mode DP-CRX, where a group of comb lines is used as a LO, see Inset-[\(II\)](#) in Fig. 4.1. The OLT ASIC further includes four ADCs, receiver DSP, and an appropriate client interface for the upstream signal.

At this point, we would like to comment on the use of OCs for enabling the bi-directional communication in both polarizations at the same wavelength. While this approach makes efficient use of the available bandwidth, it bears challenges in practice. First, OCs are costly and difficult to integrate in low-cost ONU

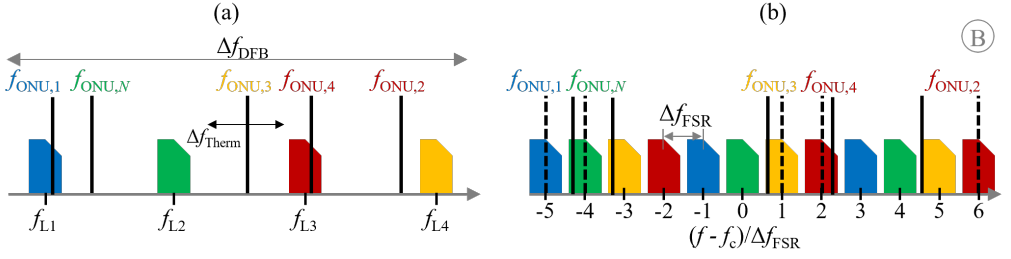


Figure 4.2: Ideal downstream optical spectra for different OLT lasers. (a) As an example, four independent lasers are considered in the central office. (b) With the proposed architecture that uses a de-interleaved comb source as a transmit laser, multiple equally-spaced spectral copies of the blue, the green, the yellow, and the red signals are transmitted. Here, the colored spectra represent the optical spectra at position ⑤ in Fig. 4.1.

transceivers. Second, the performance will be impacted by Rayleigh back-scattering and by multipath interference. It would be possible to modify our proposed architecture in a way that up- and downstream signals are transmitted in different frequency sub-bands, e.g. one side-band for downstream and the other side-band for upstream operation [91]. Another option could be the use of one polarization for the downstream and the orthogonal polarization for the upstream. Note that these two approaches reduce the PON capacity by a factor of two. Another potential solution has been presented by Shibita et al. [92], where a digital reflection interference cancellation scheme has been demonstrated. Even though this approach requires an increased DSP complexity, it allows to use the full bandwidth. Moreover, we want to point out that a bidirectional transmission enabled by optical circulators is utilized inside datacenters [152].

4.2.2 Solution to the wavelength-alignment challenge

Building lasers that fulfill the stringent cost requirements for an ONU and at the same time emit at a well-defined wavelength is a challenge. From a cost perspective, DFB lasers are an attractive option for this application. These lasers emit a single-mode, their linewidth is in the order of 1 MHz, and their maximum output power is in the order of 10 dBm [153]. As mentioned before, due to

fabrication process variations and temperature-induced drift of about $0.1 \text{ nm}/^\circ\text{C}$ [122], the wavelength of a DFB laser can vary within $\pm 2 \text{ nm}$, corresponding to a frequency range of $\Delta f_{\text{DFB}} = 500 \text{ GHz}$ in C-band. Here, we consider that the emission frequency (wavelength) of the DFB laser can be adjusted by heating or cooling of the laser sub-mount, or by changing the bias current, but only over a limited range such that $\Delta f_{\text{Therm}} \ll \Delta f_{\text{DFB}}$. We would obtain $\Delta f_{\text{Therm}} = 125 \text{ GHz}$, corresponding to 1 nm in C-band for a temperature tuning range 10°C . This becomes an issue in coherent PONs, where the wavelengths of signal and LO need to be matched. This wavelength-alignment challenge is illustrated in Fig. 4.2 (a). Here, the blue, the green, the red, and the yellow colored spectra represent four downstream signals that are centered at f_{L1} , f_{L2} , f_{L3} , and f_{L4} , evenly distributed within the frequency range Δf_{DFB} . The black vertical lines represent an exemplary set of LOs centered at $f_{\text{ONU},1}$, $f_{\text{ONU},2}$, $f_{\text{ONU},3}$, $f_{\text{ONU},4}$, and $f_{\text{ONU},N}$, randomly placed within the frequency range Δf_{DFB} . In this example it is not possible to shift $f_{\text{ONU},3}$ close to f_{L4} and thus, coherent reception is not possible for the yellow wavelength channel with a receiver with limited bandwidth. Figure 4.2 (b) illustrates the downstream spectrum of the proposed TWDM-PON, i.e., at position ⑥ in Fig. 4.1. As black vertical lines we indicate the LOs at the same random frequencies as before. These frequencies can be tuned, each within a frequency interval Δf_{Therm} . Accordingly, the DFB laser frequencies are tuned to the closest spectral copy of the corresponding downstream channel, shown as dashed black lines in Fig. 4.2 (b). As discussed before, the DFB laser in the ONU is tuned to the nearest copy of the desired downstream signal, the output of the same laser is split and used as a transmit laser for the upstream direction. If a dedicated laser is used as LO in the OLT, a similar wavelength alignment challenge as for downstream will occur in upstream direction. We therefore propose to reuse the filtered frequency comb source and use it as an LO in the OLT. In this way, the wavelength alignment is guaranteed.

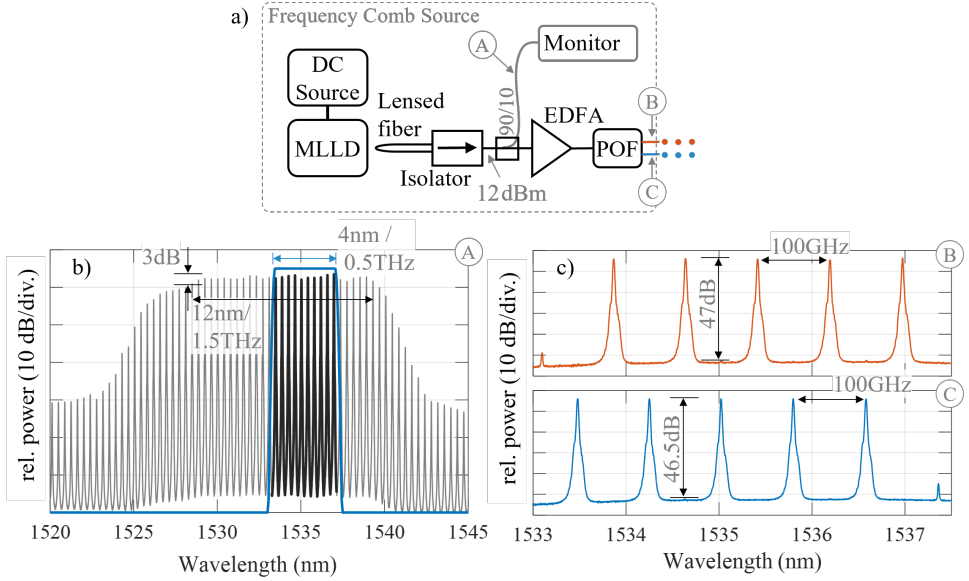


Figure 4.3: Frequency comb source used in this work. (a) Optical setup to couple the output of the MLLD-based frequency comb generator into a single-mode fiber. (b) Optical spectrum measured at position (A) at the output of the optical isolator. (c) Optical spectrum measured at position (B) and (C) at the outputs of the programmable optical filter (POF) used to interleave even and odd comb lines. The resolution bandwidth is 0.01 nm for all measurements shown in the figure.

4.3 Experimental setups and results

4.3.1 Frequency comb source

Different options exist for realizing frequency comb sources, including erbium glass oscillators (ERGOs) [154], integrated electro-optic modulators driven by an RF source [155], Kerr microresonators [156], and mode-locked laser diodes (MLLDs) [157]. For a review on frequency comb sources, we refer to [158]. Figure 4.3 (a) shows our experimental setup to generate a frequency comb and to separate even and odd comb lines. In this experiment, we use an MLLD as a frequency comb generator. A lensed fiber is employed at the output of the MLLD to couple light into the optical fiber, and a fiber-based optical isolator blocks back-reflections onto the MLLD chip. The optical spectrum measured after the

optical isolator is shown in Fig. 4.3 (b). We find a two-sided 3-dB bandwidth of 1.5 THz. The FSR is 49.8 GHz and the optical output power is 12 dBm for a direct current of 200 mA. We use a programmable optical filter (POF, Finisar-4000s) to select the spectral lines highlighted in black. Simultaneously, we equalize the power variation between the comb lines and de-interleave even and odd comb lines. The measured optical spectra at the outputs of the POF are shown in Fig. 4.3 (c). We employ an Erbium-Doped Fiber Amplifier (EDFA) before the POF in order to compensate for its insertion loss. With an optimized frequency comb generator, it might be possible to avoid this optical amplifier in future. For chip-scale integration of the frequency comb source, the POF could be also replaced by an integrated optical interleaver or a cyclic AWG, if more than two WDM tributaries are used.

4.3.2 Downstream experiments with two groups of comb lines

4.3.2.1 Experimental setup for downstream operation

In order to investigate the feasibility of the proposed coherent TWDMA-PON architecture in downstream direction, we set up a proof-of-principle experiment as shown in Fig. 4.4 (a). Here, we use either a filtered frequency comb source as transmit laser, or an ECL as a reference transmitter. We employ 10 comb lines which cover an optical bandwidth of about 500 GHz (i.e., ± 2 nm). The comb lines are modulated in a single DP-IQM. The DP-IQM is driven by two uncorrelated sequences of quadrature-phase-shift-keying (QPSK) symbols of length 2^{15} at a symbol rate of 25 GBd, corresponding to a line rate of 100 Gbit/s per OLT, which are generated by a four-channel arbitrary waveform generator (Keysight M8194A). In the digital domain, we apply a pulse shaping filter with a root-raised-cosine-shaped (RRC-shaped) frequency response having a roll-off of 0.1. We emulate the case of two WDM-multiplexed OLTs by employing a delay-and-add setup as follows. First, we de-interleave the modulated even and odd comb lines by a 50 GHz interleaver. Next, we decorrelate the tributaries using 200 m optical

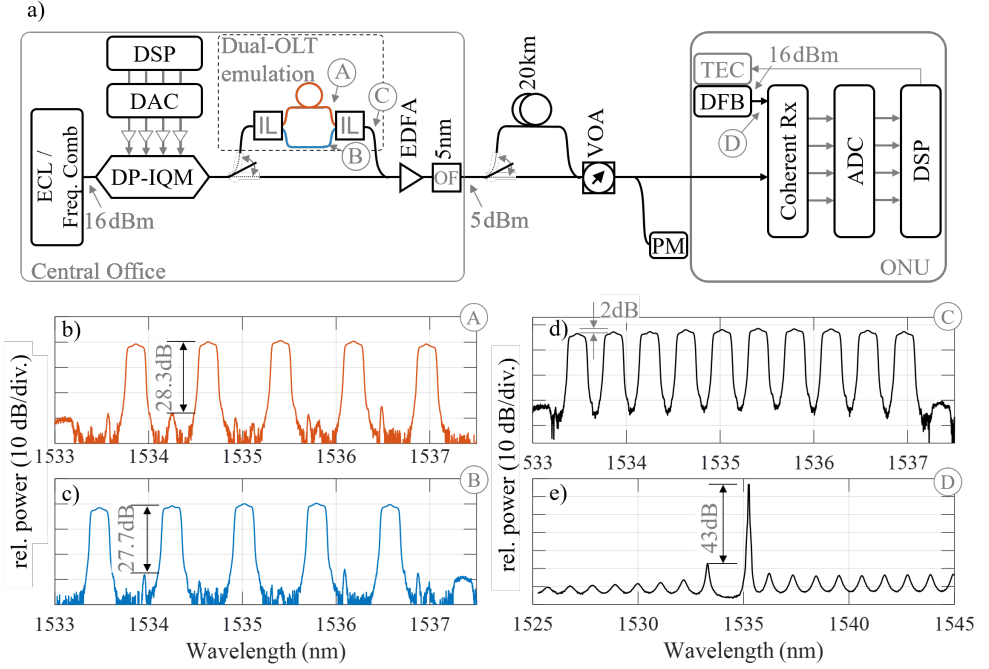


Figure 4.4: Setup for proof-of-concept evaluation of the proposed TWDMA-PON in downstream operation. (a) Experimental setup to emulate the wavelength multiplexing by employing a delay and add configuration. (b-c) Optical spectra of the emulated OLTs at positions ① and ②. Here, the red and the blue colors represent the OLT₁ and OLT₂, respectively. (d) Optical spectrum of the combined downstream signal, measured at position ③. (e) Optical spectrum emitted by the DFB laser used as local oscillator, measured at position ④. The resolution bandwidth is 0.01 nm for all measurements shown in the figure.

fiber in the upper arm. Figure 4.4 (b-c) show the measured optical spectra of the de-interleaved modulated comb lines at positions ① and ②, corresponding to OLT₁ and OLT₂, respectively. We observe an extinction ratio of more than 27.7 dB. Finally, we combine the tributaries using another interleaver. In the case of a reference transmitter with an external-cavity laser (ECL), we bypass the dual-OLT emulation setup. The losses of optical transmitter and WDM-emulation are compensated in an EDFA outputting +5 dBm optical power. This corresponds to an optical power of −2 dBm and −5 dBm per comb line for 5 and 10 modulated comb lines, respectively. At the OLT side, we employ a 5-nm-wide optical filter

to emulate the coexistence filter. Next, we use 20 km standard single mode fiber (SSMF) along with a variable optical attenuator (VOA) and a 50/50 coupler to emulate the ODN. In the back-to-back case, we bypass the 20 km optical fiber. The optical spectrum measured at position ③ is shown in Fig. 4.4 (d). We observe 2 dB power variations due to the gain tilt of the EDFA.

In the ONU, we receive the optical downstream signal with a 25-GHz integrated dual-polarization coherent receiver (DP-CRX) (NeoPhotonics). The electrical output signals are captured by a four-channel real-time oscilloscope. We apply offline DSP to detect the coarse frequency offset [17], to identify and correct timing offsets [132], to undo the polarization rotation and to mitigate inter-symbol interference (ISI) using an adaptive 2×2 multiple-input multiple-output (MIMO) filter [106], and to compensate a residual frequency offset and laser phase noise [159]. After demodulation, the bit-error ratio (BER) is measured by counting the number of bit errors in a sequence of 2^{19} bits. We compare the receiver sensitivities when using either a narrow-linewidth ECL (Keysight N7714A) or a DFB laser as LO. Figure 4.4 (e) shows the optical spectrum of the DFB LO measured at position ④. We observe a good side-mode suppression ratio of 43 dB.

4.3.2.2 Experimental results

In Fig. 4.5 we summarize our experimental results for downstream operation, comparing the receiver sensitivities for (a,b) back-to-back, and (c,d) 20 km SSMF. In (e), we study the impact of fiber nonlinearity for high transmit powers and in (f) we compare the wavelength dependence. In Fig. 4.5 (a), we plot the BER as a function of the total optical power received at the input of the ONU coherent receiver for different configurations. In all cases, the optical power of the LO is +16 dBm. The ONU receiver sensitivity for the reference case, in which an ECL is used as transmit laser in the OLT and a DFB laser as LO in the ONU, is represented by green circles. The receiver sensitivity is -27 dBm at a BER of 1×10^{-3} . Here, the linewidth of the DFB laser is 500 kHz and the output

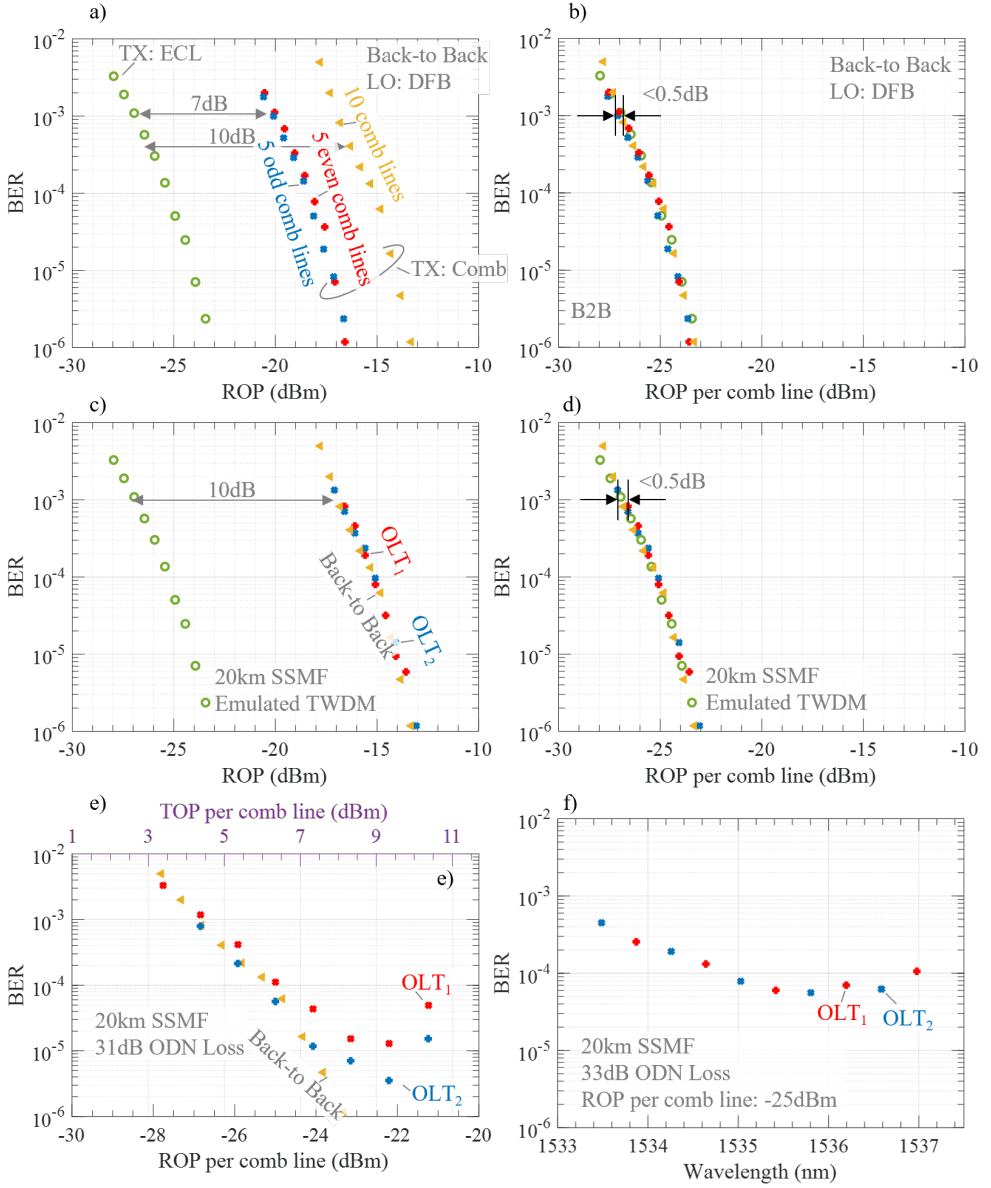


Figure 4.5: Experimental results for downstream operation. (a) **Back-to-back:** BER as a function of total received optical power (ROP) with different transmitter configurations and the DFB laser as LO. (b) **Same as (a),** but plotted as a function of the ROP per comb line. (c) **20-km SSMF:** BER as a function of ROP with and without emulated TWDM for 10 comb lines. (d) **Same as (c),** but plotted as a function of the ROP per comb line. (e) **BER as a function of the transmitted optical power (TOP) per line** into 20-km SSMF at 31dB ODN loss in case of emulated TWDM and comparison to the back-to back case. (f) **BER values are plotted as a function of ONU LO wavelength** with received optical power per comb line of -25 dBm.

power is 0 dBm. While a DFB laser with sufficient output power can be used in a real-world system, we amplified to 16 dBm with an EDFA. We compare the results with the DFB laser LO to that obtained when using an ECL LO at the ONU (not shown in Fig. 5) and observe a penalty of < 0.5 dB for the DFB laser, which we attribute to the higher laser linewidth and amplified spontaneous emission (ASE) noise. Furthermore, we do not observe an increased penalty from the phase noise.

We then replace the transmit laser by the MLLD with 5-even, or 5-odd, or 10 comb lines. The measured BERs are plotted with the red plus, blue crosses, and yellow triangular markers, respectively. With a DFB laser as LO, we obtain a receiver sensitivity of -20 dBm and -17 dBm at a BER of 1×10^{-3} in case of 5 and 10 comb lines, respectively. Compared to the reference case with ECL transmitter and DFB LO, the receiver sensitivity is reduced by 7 dB and 10 dB, which is due to the fact that the transmit power is distributed over multiple comb lines. In Fig. 4.5 (b), we plot the same results as a function of the optical received power per comb line. The results confirm that the receiver sensitivity (in terms of the total received optical power (ROP)) is proportional to the number of comb lines and we observe negligible penalty of less than 0.5 dB in all cases. In the next experiment, we measure the performance of emulated TWDM downstream for two interleaved sets of five comb lines with 20 km SSMF. The measured BERs for the red and the blue subset refer to the red plus and blue cross symbol in Fig. 4.5 (c). As expected, we observe a similar 10 dB receiver sensitivity penalty as in the back-to-back measurement. Next, we plot the emulated TWDM downstream results over the total receiver power per comb line and observe 0.5 dB penalty. In the next experiment, we investigate the fiber non-linearity by varying the transmit optical power (TOP). Here, we consider 20 km optical fiber followed by a 27 dB attenuation in the VOA to emulate the splitter and splicing losses, which corresponds to accumulated ODN loss of 31 dB. Figure 4.5 (e) shows the measured BER as function of TOP per comb line as well the ROP per comb lines. We found that the optimum TOP per comb line is 9 dBm, which allow for more than the 37 dB ODN loss budget.

To demonstrate that our approach can solve the wavelength alignment challenge occurring when using DFB lasers without wavelength alignment, we measure the BER for different LO frequencies within a range of 500 GHz around the center of the MLLD comb, see Fig.4.5 (f). Again, two interleaved subsets of five 100-GHz-spaced modulated downstream comb lines are emulated in the central office by employing dual-OLT emulation. The red- and blue-colors in the plot correspond to these two subsets of comb lines, which are dedicated to the red and blue ONUs in Fig.4.4(b-c), respectively. As an LO, we employ an ECL and tune it over the comb bandwidth to emulate DFB lasers with varying emission wavelengths. From the results discussed earlier, we can expect that comparable BER values are obtained if DFB lasers are used in the ONUs. The measured BER levels are highlighted by markers of the respective color. We find that the BER stays below 1×10^{-3} for received powers of -25 dBm for all LO frequencies covering a wavelength (frequency) range of ± 2 nm (± 250 GHz) with respect to the center comb line.

4.3.3 Upstream operation with a frequenting comb source as an LO

4.3.3.1 Upstream experimental setup

To investigate the upstream operation, we use the setup shown in Fig. 4.6 (a): We emulate the case of two ONUs, by launching two DFB lasers, at 1553.38 nm and 1535.80 nm, respectively, into a DP-IQM that is fed from a four-channel arbitrary waveform generator running at a sampling rate of 120 GSa/s. The digital test pattern consists of two uncorrelated random sequences of 2^{15} QPSK symbols at a symbol rate of 25 GBd having a RRC spectral shape with a roll-off factor of 0.1. The measured optical power at the output of the DP-IQM is in the order of -5 dBm. In this experiment, we emulate two ONUs by an de-interleaver and a delay-and-add setup, see Fig. 4.6 (a), block: Dual-ONU emulation. We bypass the dual-ONU emulation setup in the reference measurements. The ODN consists of 20 km optical fiber and a VOA. In the back-to-back measurement, we bypass the

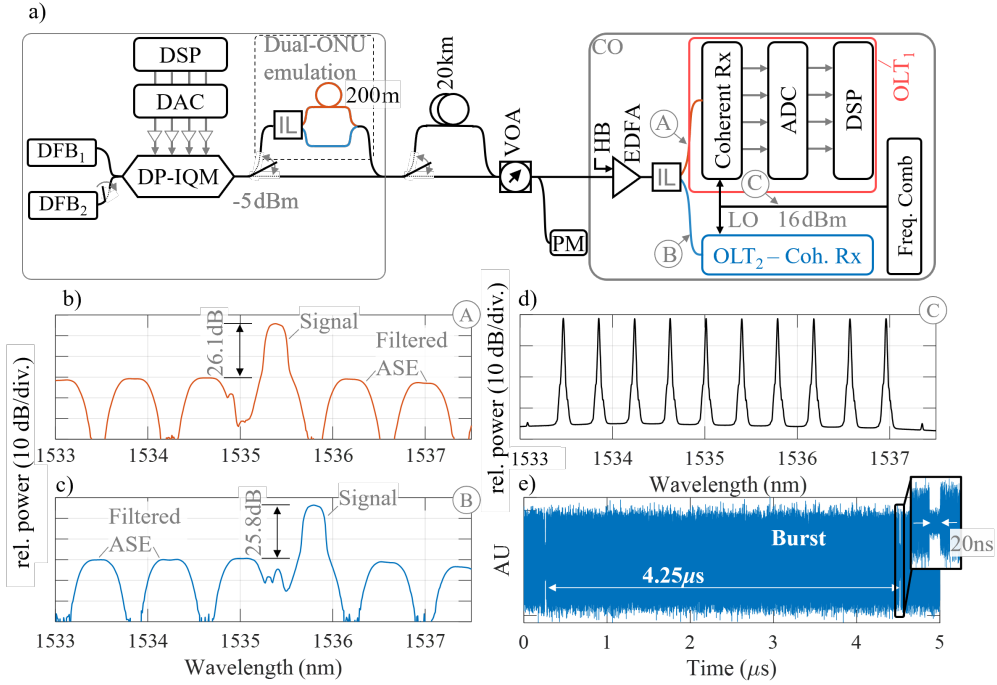


Figure 4.6: Upstream operation of the proposed TWDM-PON. (a) Experimental setup for a proof-of-principle demonstration of the proposed TWDM-PON architecture in upstream operation. (b-c) Optical spectra of the emulated ONUs, measured at positions ① and ② with a resolution bandwidth of 0.1 nm. Here, the red and the blue colors represent the OLT₁ and OLT₂, respectively. (d) Optical spectrum of the LO comb, measured at position ③ with a resolution bandwidth of 0.01 nm. (e) The received 4.25 μ s long burst-mode signal with 20 ns inter-burst gap.

20 km optical fiber. At the OLT, the received optical signal is pre-amplified using an EDFA prior to be de-interleaved with an IL. To measure the received optical power, we use a 50/50 optical power splitter and an optical power meter before the EDFA. To minimize the effect of the EDFA transient, we use an additional DFB laser at a wavelength of 1545 nm and an optical power of -35 dBm, which we indicate as a holding beam (HB) in Fig. 4.6 (a). Fig. 4.6 (b-c) shows the de-interleaved upstream signal measured at positions ① and ②, respectively. The red and the blue color represent the corresponding red and blue wavelength grids, which are dedicated to OLT₁ and OLT₂, respectively. The spectral shape of the ASE noise is determined by the transmission windows and the filter design of the

IL. The receiver consists of a 25 GHz DP-CRX followed by a four-channel real-time oscilloscope. Finally, we apply an offline preamble-based burst-mode DSP. The frequency comb generated by the MLLD acts as LO. Figure 4.6 (d) shows the optical spectrum of the filtered and flattened LO comb, measured at position ©. The peak power variation is <0.5 dB. The available memory of the arbitrary waveform generator allows to generate bursts with a length of 106252 symbols, which are followed by 500 zeros. Figure 4.6 (e) shows a received waveform of a $4.25 \mu\text{s}$ long burst with 20 ns inter-burst gap. The ROP is -25 dBm. Note that the adjacent bursts are coming from the same transmitter. However, this configuration allows to study the DSP and the burst mode capability of a conventional coherent receiver.

4.3.3.2 Upstream DSP

Figure 4.7 (a) shows the DSP chain for burst-mode upstream transmission. The single and double lines represent the real-valued and complex-valued signals, respectively. First, a frontend correction is carried out to compensate for the receiver-side imbalances and skews. The shaded region on the left represents the supporting DSP block, which enables the burst-mode detection using an off-the-shelf DP-CRX. First, we compare different complex-valued preamble sequences, e.g., Schmidl's and Cox's (S&C) [160], Minn's [161], Park's [162], Modified Park's [163] and complex-complementary Golay preamble [164–167]. Fig. 4.7 (b) shows the cross-correlation between the X- and Y- polarizations of the simulated upstream signal without any noise, and we found that the Golay preamble shows narrower peak compared to the other preamble sequences. Note that we employ this peak to align the upstream burst and initiate different DSP blocks. Furthermore, the Golay sequence has complementary properties, so it does not require the use of a pseudo-inverse matrix-based channel estimation, which is computationally intensive. Therefore, we use Golay preambles in our subsequent burst-mode experiments. Figure 4.7 (c) shows the normalized cross-correlation between X- and Y- polarization as a function of time with 64 Golay symbols as a preamble. Here, we observe a peak which marks the beginning of

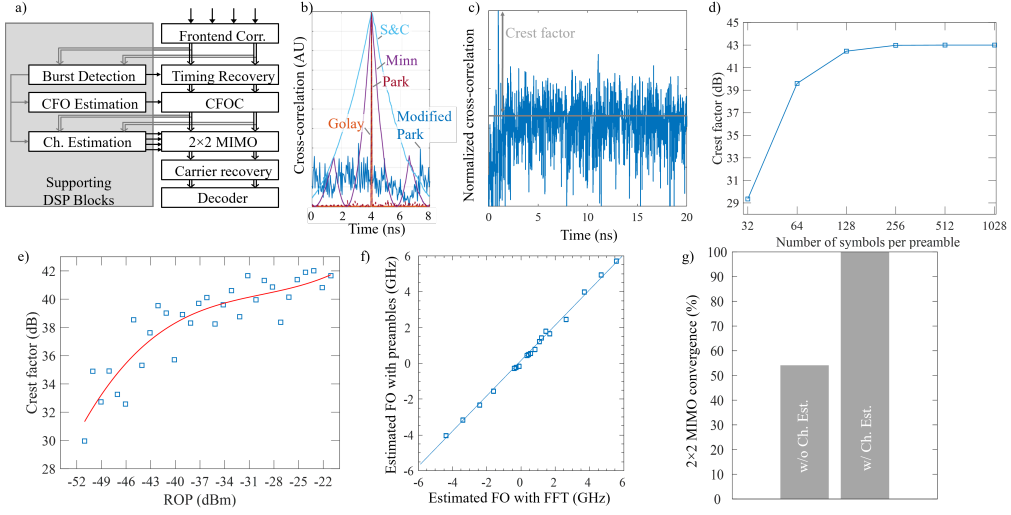


Figure 4.7: Upstream DSP. (a) The OLT DSP chain to process the burst-mode upstream signal. The gray-shaded region shows the supporting DSP blocks. (b) Cross-correlation as a function of time for different complex preamble sequences. (c) Normalized cross-correlation between X- and Y-polarization. (d) The crest factor (CF) of the cross-correlation as a function of the numbers of symbol in the preamble. (e) The CF as a function of received optical power (ROP). (f) The comparison between ideal FFT-based frequency offset estimation (FOE) and preamble-based FOE. (g) The comparison of MIMO filter convergence ratio with and without complex-Complementary Golay preamble-based channel estimation.

the burst. We utilize this peak to reset the timing error detector, initiate both the data-aided coarse frequency offset (CFO) estimation, and Golay preamble-based channel estimation. These processes occur at the onset of every upstream burst. Figure 4.7 (d) shows the crest factor (CF) as a function of the number of symbols (2^n) in the Golay preamble, where $n = 5, 6, 7, 8, 9$ and 10 . We observe an increase in the CF when $n \leq 8$ and negligible increase afterward. In the next experiment, we vary the ROP and estimate the corresponding CF using 64 Golay symbols as a preamble. In the Fig. 4.7 (e), we plot the measured CF as a function of ROP in blue, and the fitted curve is shown in red. We observe that the fitted CF decreases by 6 dB when the ROP changes from -22 dBm to -42 dBm. However, the CF remains high enough to perform all the above-mentioned DSP operations. The CF can be increased by introducing more Golay symbols to the preamble to compensate for

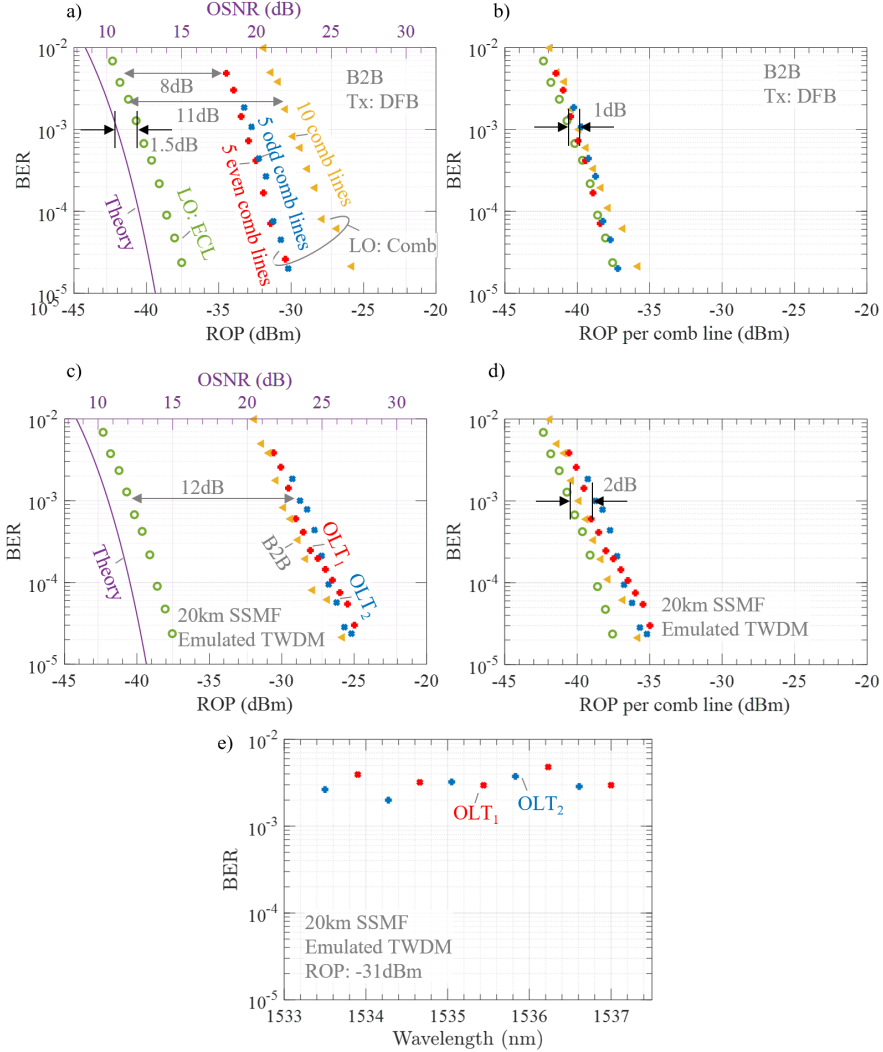


Figure 4.8: Experimental results for upstream operations. (a) BER as a function of ROP and optical signal-to-noise ratio (OSNR) for different types of transmit and LO lasers. The ROP and the OSNR are measured before and after the preamplifier EDFA, respectively. The LO power is 16 dBm in all cases. (b) The same BER values are plotted as a function of the ROP per comb line. (c) The BER values are plotted as a function of the ROP and OSNR in case of emulated TWDM upstream with 20 km SSMF. (d) The same BER values of emulated TWDM upstream are plotted as a function of the ROP per comb line. We observe a penalty of 2 dB. (e) We plot the BER values as a function of the ONU laser wavelength with received optical power of -31 dBm.

low ROP, note that the longer Golay preamble sequence is less susceptible to rapid changes in the channel and in the polarization. Timing recovery is the next step in the main DSP chain, which is done in two phases. In the first step, the timing error is blindly detected in the frequency domain by employing the Barton and Al-Jalili algorithm [131, 132]. In the second step, the timing error is corrected by employing a seventh-order Lagrange interpolator. Subsequently, we estimate the CFO using the preamble sequence and compensate for it in the coarse frequency offset compensation (CFOC) step in the main DSP chain [168]. Figure 4.7 (f) shows the estimated frequency offset (FO) using the FFT and preamble methods. We observe a penalty of <100 MHz, which is low enough for the following DSP steps i.g., channel estimation and carrier phase recovery. Subsequently, we apply an adaptive 2×2 multiple input multiple output (MIMO) equalizer based on the constant modulus algorithm (CMA) to compensate for the channel and undo the polarization rotation [133]. In the proposed DSP, we estimate the channel using the complementary property of the Golay sequence [166, 167] and initialize the filter coefficients of the CMA based MIMO equalizer. The Golay sequence-based channel estimation is more efficient and noise tolerant compare to pseudo-inverse matrix-based channel estimation. Note that both techniques require coarse frequency offset correction and synchronization. Figure 4.7 (g) shows the performance comparison without and with the channel estimation technique. Here, we digitally rotate the polarization state before the MIMO equalizer and estimate the statistics from two thousand random polarization states. We observe that the BER can be measured in 55 percent of cases without channel estimation, and in 100 percent of cases with channel estimation. The remaining DSP blocks (fine frequency offset compensation, carrier recover and decoder) are the same as in continues-mode DSP.

4.3.3.3 Upstream experimental results

In the first upstream experiment, we measure the OLT receiver sensitivities in case of a back-to-back configuration for different optical powers incident to the OLT pre-amplifier when employing one DFB laser as transmitter at the ONU

side, and an ECL as LO laser at the OLT side. Simultaneously, we measure the optical signal to noise power ratio (OSNR) after the pre-amplifier EDFA. Similar to downstream operation, the received power is swept by tuning a VOA. In Fig. 4.8 (a), we plot the BER as a function of the ROP with green circles for the reference case (DFB transmitter and ECL LO). The measured receiver sensitivity is about -40 dBm at a BER of 1×10^{-3} . In this experiment, the loss budget is about 35 dB. We also compare this results with an ideal case (ECL transmitter and ECL LO), and observe negligible 0.5 dB penalty, i.e., the increased phase noise is not limiting the performance. We did not plot the BERs referring to the ideal case for better readability of the figure. Afterward, we replace the ECL LO by a frequency LO comb at the OLT side. We compare the three cases of selecting either 5-even, or 5-odd, or 10 comb lines by appropriate adjustment of the POF. Note that the total LO power is kept constant at 16 dBm so that the optical power per comb line decreases with an increasing number of lines, which is clearly visible in Fig. 4.8 (a). There, the red filled circles, the blue squares and yellow triangle correspond to the cases of having 5-even, or 5-odd, or 10 comb lines as LO, respectively. The receiver sensitivities are -33 dBm and -30 dBm for 5 and 10 comb lines, respectively. Compared to the reference case with DFB transmitter and ECL LO, the receiver sensitivity is reduced by 8 dB and 11 dB, of which 7 dB and 10 dB are due to the fact that 5 and 10 comb lines LO are used with the same total optical power (16 dBm). The additional 1 dB penalty is attributed to the increased amount of optical noise impairing the signal quality, which is a result of the accumulation of various LO-ASE beat noise terms when using a comb source as an LO [1]. Eventually, the loss budgets are reduced by 8 dB and 11 dB, respectively. In Fig. 4.8 (b), we summarize the BER performance as a function of the received optical power per comb line and find a linear relation between the BER and the number of comb lines. The 1 dB higher received power required to achieve the same BER level when using a comb source as LO instead of an ECL is caused by accumulated LO-ASE beat noise. Next, we measure the performance of emulated TWDM upstream for two emulated ONUs with 20 km optical fiber. The measured BER performances of two OLTs as a function of ROPs are shown in Fig. 4.8 (c). We observe 12 dB performance difference compare to the reference

case (DFB transmitter and ECL LO). Next, in Fig. 4.8 (d), we plot the emulated TWDM downstream results over the total ROP per comb line and observe a 2 dB penalty. At the same time, the loss budget is reduced by 2 dB, which is due to the increased LO-ASE noise, and to the power loss from the dual-ONU emulation. In a last experiment, we analyze the impact of wavelength variations of the ONU transmit laser on the performance by actively tuning an ECL. The BER as a function of the ONU laser wavelength is plotted in Fig. 4.8 (e) for the case of 10 comb lines acting as an LO. The BER remains below 1×10^{-2} for received powers of -31 dBm for an ONU frequency (wavelength) variation of ± 0.25 THz (± 2 nm). Here, the red and the blue color represents the red and the blue wavelength grids, which represents OLT_1 and OLT_2 , respectively.

4.4 Summary

In the future, PONs will not only provide FTTH connectivity but also support additional services with specific traffic patterns and requirements. One possible solution to meet the diverse specifications and requirements of future optical access networks is to employ DP-QM and coherent reception, along with statistical TWDM/TWDM-A technology. However, coherent TWDM-PON poses a technical challenge: ensuring wavelength matching between the transmit laser and the LO when employing low-cost lasers, such as DFB lasers. To overcome this issue, we propose a novel coherent TWDM-PON architecture based on a frequency comb source at the OLT and low-cost DFB lasers at the ONUs. It broadcasts the downstream signal by de-interleaving the frequency comb lines into two or more wavelength grids and modulate them with independent data. Downstream signal covers a ONU wavelength span of ± 2 nm (± 250 GHz). We propose to tune the DFB LOs by employing a TEC or by changing direct current at the ONU side. For upstream operation, a tuned DFB-LO acts as a transmit laser. The upstream signals are separated by a CAWG and detected by a dual-polarization coherent receiver, where de-interleaved frequency combs act as LOs. We experimentally demonstrate a 200 Gbit/s TWDM-A-PON. We achieve a loss budget of more than

37 dB in downstream and 24 dB in upstream. An LO-wavelength variation of up to ± 2 nm (± 0.25 THz) can be tolerated.

End of journal [2]

5 Subcarrier Based Coherent PON for Smart Sustainable City

This chapter summarizes the results of a German government-funded project titled *KIGLIS*. In this project, various consortium partners contributed according to their technical expertise, with a focus on optical access networks to support AI-driven smart and sustainable cities. The outcomes of this project are published in the Journal of Optical Communications and Networking [3]. My contributions to the publication include overall editing and jointly outlining the introduction, vision, and the sections on fiber-optic network technologies. The section on subcarrier-based coherent PONs represents my principal contribution and forms a core part of this thesis. Accordingly, this chapter provides modified and expanded explanations of the coherent time-, wavelength-, and frequency-division multiplexed (via subcarrier) PON architecture, along with detailed descriptions of the DSP chains for both downstream and upstream transmission. The section on IM/DD-based 100 Gbit/s PON was jointly contributed by IPQ-KIT and VPIphotonics. The section on dense network monitoring was developed collaboratively by Nokia Bell Labs and AIFB-KIT. The section on network resource allocation was developed jointly by atesio and TelemaxX Telekommunikation. Finally, the section on remote assistance was contributed by FZI, with feedback and support from all other consortium partners. The content from the publication has been adapted here with appropriate revisions to align with the structure, notation, and research focus of this thesis.

Start of journal [3]

Copyright © 2025 Optica Publishing Group under the terms of the Optica Open Access Publishing Agreement

Optical-access networks for smart sustainable cities: from network architecture to fiber deployment

Journal of Optical Communications and Networking, Volume: 27 Issue: 3 pp. 221-232

DOI: doi.org/10.1364/JOCN.542368

Md Mosaddek Hossain Adib^{1,2,*}, Patrick Matalla^{1,*}, Christoph Füllner^{1,2}, Shi Li³, Elias Giacomidis³, Christian Raack⁴, Ulrich Menne⁴, Michael Straub², Tarek Saier⁵, Christoph Schweikert⁶, Stefan Orf⁷, Martin Gontscharow⁷, Tobias Käfer⁵, Michael Färber^{5,8}, André Richter³, René Bonk², and Sebastian Randel¹

¹ Institute of Photonics and Quantum Electronics (IPQ), Karlsruhe Institute of Technology (KIT), Germany

² Nokia Bell Labs, Stuttgart, Germany

³ VPIphotonics GmbH, Berlin, Germany

⁴ atesio GmbH, Berlin, Germany

⁵ Institute of Applied Informatics and Formal Description Methods, Karlsruhe Institute of Technology, Karlsruhe, Germany

⁶ TelemaxX Telekommunikation GmbH, Karlsruhe, Germany

⁷ FZI Research Center for Information Technology, Karlsruhe, Germany

⁸ Currently at AI Center ScaDS.AI, Technical University Dresden, Dresden, Germany

*These authors contributed equally to this work.

With the steadily progressing digitization of our society and the migration into urban areas, digitized and highly-connected smart cities have attracted much attention from the research community due to their impact on everyday life, potential for new innovations, and ability to reduce carbon footprints. The versatile applications, which are intended to improve life in cities in various aspects have one thing in common – they rely on widespread, reliable, and high-performing communication networks. Therefore, optical-access networks will be a crucial part of the smart cities' network infrastructure as they provide cost-effective and high-speed connectivity to antenna sites, residents, enterprises, businesses, and regional data centers in a point-to-multipoint topology. In this article, we address the overall impact of this urban transformation on such networks. We outline our vision of the future smart sustainable city, which will leverage advanced optical-access networks. Subsequently, the physical layer design of optical-access networks is analyzed in the context of point-to-multipoint network topology. This includes a 100-Gbit/s intensity-modulation and direct-detection (IM/DD) passive optical network (PON), and a 200-Gbit/s Coherent PON utilizing 8-digital subcarrier-based time and wavelength division multiplexing and coherent detection. We discuss artificial intelligence-based network monitoring and resource allocation. Next, we provide a techno-economical study for sustainable fiber deployment strategies. Finally, we report the results of a network demonstration for the remote assistance of a connected autonomous vehicle.

5.1 Introduction

The digitization of societies around the globe continues apace. Omnipresent connectivity in conjunction with artificial intelligence will make it possible to automate and optimize more and more processes in almost all aspects of life. In many areas, the vision of a smart sustainable city in which a large number of people, devices, and machines communicate with each other is starting to become

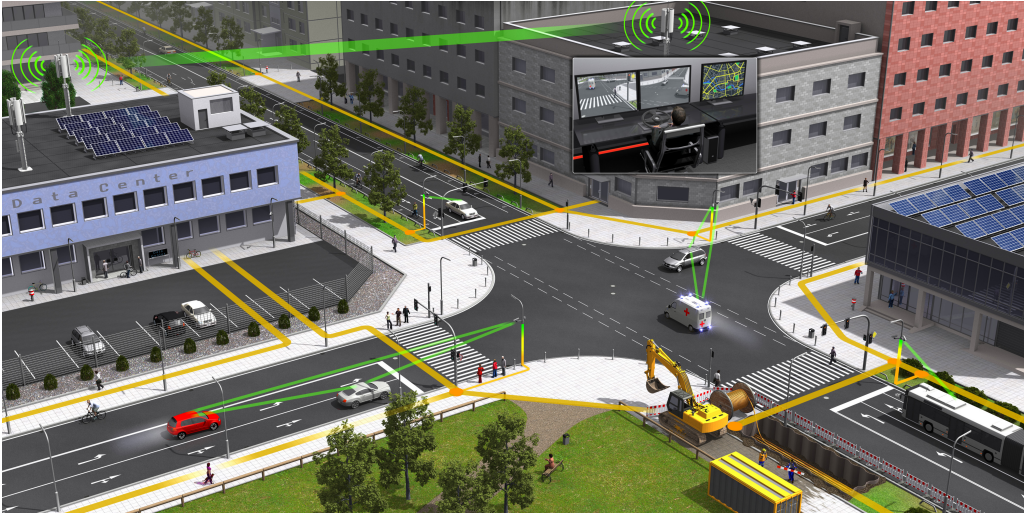


Figure 5.1: Vision of a smart sustainable city incorporating a dense fiber-optic network (yellow lines) enabling high-speed wireless connectivity (green lines). Small cells, integrated, e.g., in street and traffic lights, provide low-latency broadband access for diverse applications, such as connected driving, augmented reality, and smart-city monitoring. In addition, high-speed wireless point-to-point links complement the fiber network where fiber deployment is difficult, or as redundant/protection paths. Associated processing and storage needs for smart-city applications and services are accommodated in regional data centers. From an infrastructure control center, a remote operator can provide assistance to autonomous vehicles in critical situations. In this scenario, an ambulance equipped with network connectivity transmits vital information to the smart city monitoring system and nearby vehicles as it crosses a junction. This is achieved using high-speed wireless, point-to-multipoint optical access, and vehicle-to-vehicle communication technologies.

reality. As a result, the international telecommunication union (ITU) predicts 97 billion mobile connected devices by 2030, around 14 times more compared to 2020 and more than ten times the human population [169]. In future cities, this will include a large number of connected self-driving vehicles, which will exchange immense amounts of data with other road users and an intelligent infrastructure, imposing stringent demands on the underlying networking infrastructure. This scenario together with a wide spectrum of novel services and applications will be made possible by the ongoing rollout of the fifth generation (5G) mobile network and, expected by 2030, the sixth generation (6G) mobile network, which will feature increased data rates and reduced latency by densifying mobile cell

sites and by utilizing additional frequency bands [170]. Optical networks, which utilize the vast bandwidth of low-loss optical fibers, are used to aggregate the data traffic of cell sites, homes, enterprises, and sensor nodes in central offices and regional data centers [77, 171]. Besides the installation of a mobile network, the smart sustainable city will require the rollout of a next-generation fiber-optic network, which addresses the diverse requirements, e.g., in terms of data rate, latency, security, as well as operational and capital expenditures.

In this article, we describe our vision of a smart sustainable city, from which we derive the requirements for future fiber-optic access networks. Taking a holistic approach, we discuss how passive optical networks (PONs), can be scaled to provide high data rates and low latencies as well as network monitoring and dynamic resource allocation. We further present the results of a techno-economical study for a sustainable fiber rollout in the city of Karlsruhe, a city in Germany with approximately 300,000 residents. In the final section, we report on the access network demonstration of remote assistance for a connected autonomous vehicle. This paper provides an overview of the various results achieved within a three-year joint project named KIGLIS funded by the German Federal Ministry of Education and Research (BMBF). The KIGLIS project can be found here [172].

5.2 Vision of a Smart Sustainable City

The smart sustainable city uses advanced technologies to improve the quality of life of its residents, businesses, and visitors, while answering the economic, social, environmental, and cultural needs of current and future generations [173]. In this context, the smart city has to address the challenges and issues residents of modern cities are facing today. One example is the traffic situation, where congested streets and occupied parking spaces lead to carbon emissions, air pollution, stress, and accidents. Another example is the monitoring of environment and infrastructure, e.g., for city-wide waste management, disaster prevention, and safety. It is thereby imperative that all technical solutions comply with the prevailing laws concerning, e.g., privacy, safety, and data protection. In the future

smart sustainable city, a variety of connected services in the fields of economy, mobility, living, governing, and social affairs [174] place stringent demands on the underlying communication infrastructure in terms of security, latency, speed, management, and energy efficiency.

A key enabler for this is an ubiquitous and seamless communication infrastructure which includes broadband wireless and fiber-optic access, e.g., using Wi-Fi and 5G/6G, sensor networks based on LoRaWAN [175], and regional data centers, allowing high-performance, energy-efficient, and secure processing and storage of data. Our envisioned smart sustainable city is illustrated in Fig. 5.1. The realization of automated driving in a densely populated city will not only require a large number of sensors like cameras, radars, lidars, and microphones located in cars or at the traffic infrastructure but also a high-speed and low-latency communication infrastructure which allows to aggregate this data. This makes it possible to create a digital twin of the cities traffic situation in real-time. Artificial intelligence (AI) algorithms can then be used to optimize processes in the city and to enable secure automated driving. In a complex driving situation, a human remote operator can access the data and safely steer the vehicle around an obstacle. Processing and storing the data in regional data centers is not only energy-efficient but also allows privacy and data security.

In order to facilitate such a scenario, we envision a dense fiber-optic network based on optimized PON not only households and enterprises but also wireless small cells with high bandwidth and low latency to data centers within distances of up to 20 km [80, 81]. This allows to find locations also outside the expensive city centers. In the following, we look at various aspects of optical-access networks on different layers: network architecture, network maintenance, resource allocation, and finally, aspects of sustainable fiber rollout.

5.3 Fiber-Optic Network Technologies

This chapter covers the aspects of a smart city PON on the physical layer. Subsection A provides an overview of recent advances in PON standardization and the working principle of a PON system, followed by the requirements of our envisioned smart city PON architecture. In sections B and C we then present our research results for a 100-Gbit/s IM/DD and a 200-Gbit/s coherent high-speed PON, respectively. Finally, in subsection D we investigate machine learning methods to monitor the PON infrastructure more efficiently and possibly predict failures.

5.3.1 Passive Optical Networks

PONs are the preferred network architecture in fiber-optic access. As a point-to-multipoint network based on bidirectional transmission over a single fiber and a purely passive optical splitter, they require significantly fewer active devices when compared to a point-to-point network. The most frequently deployed PON standards are the Gigabit PON (GPON) and its successor, the symmetric 10-Gbit/s PON (XGS-PON). The highest capacity commercially available today is offered by the symmetric 25-Gbit/s PON that is defined in a multi-source agreement (25GS-PON MSA) [46, 176]. Recently, a 50-Gbit/s PON standard was agreed upon and is expected in the market in a few years from now [49]. In all these standards, the intensity of the light emitted by a laser is modulated by data and a single photodiode converts the received optical power into an electrical current - a scheme commonly referred to as intensity modulation and direct detection (IM/DD). In the optical distribution network (ODN), connecting a central office to a number of 32 or 64 endpoints over distances up to 20 km, a common feeder fiber is split using an optical power splitter. The total loss in the splitter, the fiber, splices, connectors together with a network deployment margin can be as high as 28 dB or even 35 dB according to the budget classes of the PON standards mentioned above, e.g., the 50G-PON [49]. The specified

receiver sensitivity dictates the transmitted optical power that also has to take the optical path penalty, introduced, e.g., by chromatic dispersion (CD) and fiber nonlinearities, into account. In downstream, the optical line termination (OLT) sends a continuous stream of data that is distributed to all optical network units (ONUs), which select only the allocated grants for further processing. In upstream direction, the OLT is dynamically allocating time slots, in which the ONUs are allowed to transmit. This way, the PON is a shared medium using time-division multiplexing (TDM) in downstream and time-division multiple access (TDMA) in upstream.

We envision that an evolved PON standard, which will likely be standardized in the time frame from 2025 to 2030, will further extend the possibilities of today's PON generations towards the requirements of future smart sustainable cities, such as new bandwidth-hungry services and a massive number of connected sensors. The large variety of smart city services will impose high demands in terms of data rate, reliability, latency, cost, flexibility, and energy efficiency [75]. Currently, it is an open question whether a 100-Gbit/s or a 200-Gbit/s PON should follow the 50-Gbit/s PON. Since 25G-PON, the PON transceiver technology is following the data center market trends [93]. Therefore, the best course for PON is to focus on the same $2\times$ increase in symbol rate as the ecosystem that it is leveraging. Thus, we focus our investigations on a future 100-Gbit/s IM/DD-PON and 200-Gbit/s coherent subcarrier PON for our smart-city concept. Considering the demands for high-bandwidth and low-latency, we expect that the future PON will have to offer not only a data rate of 100-Gbit/s or more, but also a latency of below 1 ms and 99.999% reliability. We present our results from the KIGLIS project considering two different 100-GBd-capable PON architectures.

5.3.2 IM/DD 100 Gbit/s PON

All PON standards mentioned above employ non-return-to-zero (NRZ) on-off keying (OOK) as the modulation format. So far, this format has prevailed because of its simplicity, its high tolerance against device nonlinearities, and its high

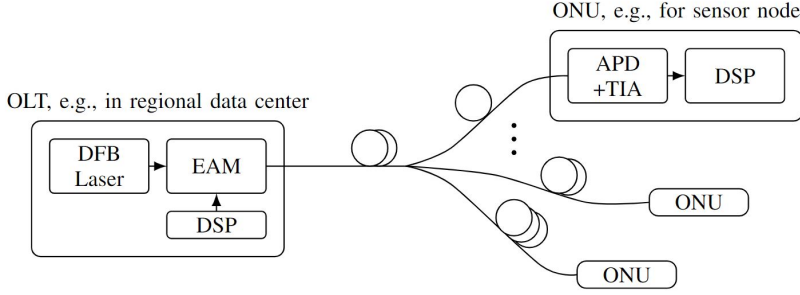


Figure 5.2: Downstream link configuration of the envisioned 100-Gbit/s IM/DD PON.

receiver sensitivity. However, scaling to data rates of 100-Gbit/s and above, will significantly reduce the tolerance versus CD, which is inversely proportional to the square of the symbol rate. Furthermore, bandwidth limitations of low-cost components will impair the signal quality. These drawbacks can be mitigated by increasing the spectral efficiency using a higher-order modulation format, e.g., quaternary pulse-amplitude modulation (4-PAM), in combination with adaptive equalization and forward-error correction (FEC) [96]. However, realizing a loss budget of around 30 dB poses a challenge, as 4-PAM modulation requires a significantly higher signal-to-noise ratio in comparison to OOK [177].

Figure 5.2, depicts our envisioned link configuration for the downstream of a 100-Gbit/s IM/DD PON using 4-PAM modulation. At the transmitter, we consider a distributed-feedback (DFB) laser emitting in O-band at a wavelength around 1344 nm in order to study the CD tolerance. The O-band has the benefit that the CD is significantly lower than in C-band around 1550 nm, however, this comes at the cost of a slightly increased fiber loss. We consider an electro-absorption modulator (EAM) [178], whose nonlinearity is pre-compensated using digital signal processing (DSP). At the receiver side, an avalanche photodiode (APD) followed by a transimpedance amplifier (TIA) is used to convert the received optical signal into an electrical one. APDs are commonly used in PONs, since they offer a higher receiver sensitivity compared to PIN photodiodes, which allow achieving high loss budgets. Finally, the received signal is processed using DSP. We simulate the proposed 100-Gbit/s 4-PAM downstream link as shown in Fig. 5.2

in a numerical simulation using the commercial software *VPItransmissionMaker Optical Systems* [179]. In O-band (1344 nm), we explore the effect of using an EAM with certain chirp characteristics. The bandwidth of the EAM is set to 55 GHz and electrical noise is set to $20 \text{ pA(Hz)}^{1/2}$. We found best performance for a drive signal with peak-to-peak voltage of 1.6 V and a EAM bias of -1.9 V. The inset in Fig. 5.3 shows the transfer function of the EAM and its measured chirp. To reduce the system costs, we excluded RF driver amplifiers and the optical launch power is set to 8.8 dBm. For the standard single-mode fiber, we used a CD coefficient of 3.85 ps/nm/km, a CD slope of 0.092 ps/(km \times nm²), an attenuation of 0.35×10^{-3} dB/km, and a nonlinearity index of 2.6×10^{-20} m²/W. At the receiver, we consider an APD/TIA with a bandwidth of only 25 GHz, which would allow the reuse of low-cost components from 50G-PON ONUs. The electrical low pass filters at both OLT and ONU were of fourth-order Bessel type. At the OLT transmitter, we performed an optimization of the PAM4 symbol levels. At the ONU, the receiver DSP includes timing synchronization, a 5-tap data-aided feed-forward equalizer, and FEC with 15% overhead and a bit-error ratio (BER) threshold of 0.0125 [180]. In Fig. 5.3, we compare the receiver sensitivity for optical back-to-back and for 20 km fiber either without or with chirp of the EAM. We find that CD leads to a 1-dB sensitivity penalty if no chirp is considered. With the chirp, this penalty increases to 2 dB. For the latter case, a receiver sensitivity of -22 dBm is achieved, which results in a total link budget of 30.8 dB. Therefore, the simulation shows that the proposed IM/DD PON can indeed fulfill the data-rate and link-budget requirements of a PON serving a future smart sustainable city. Further receiver sensitivity improvements can be achieved by replacing the linear 5-tap equalizer by neural-network-based equalizers. As discussed in [181–184], these allow the compensation of nonlinear effects caused, for example, by the EAM, gain saturation of semiconductor optical amplifiers (SOAs), or increased chromatic dispersion in C-band PONs at the expense of increased computational complexity.

With the rising number of digital services in a smart sustainable city, the number of optical network users may grow up to 256 users in the future [185]. Increasing

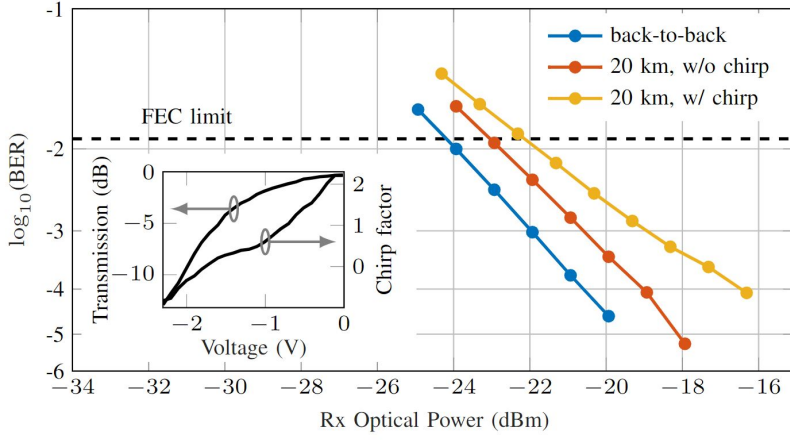


Figure 5.3: Simulation results for IM/DD PON downstream operation. The inset shows the transmission and chirp characteristics of the EAM.

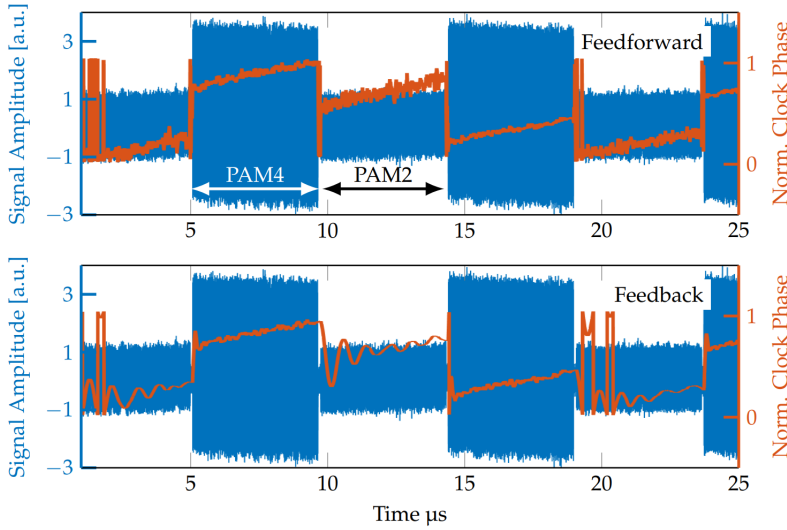


Figure 5.4: Received AC-coupled burst-mode signal after resampling in a 56 GBd IM/DD PON upstream using free-running transmitter and receiver oscillators with a nominal clock frequency offset of 1 ppm and estimated sampling offset for a representative feedback and feedforward clock recovery algorithm over time.

the split ratio from 64 to 256 results in a reduction in optical power of around 6 dB per ONU branch. In order to maintain PON fiber distances of up to 20 km, a larger loss budget is therefore required, e.g., through the use of optical amplifiers. In addition, a larger number of network subscribers has an influence on the burst duration. In order to guarantee the same latency as for 64 users, the burst duration must be shortened. Each burst consists of a preamble for identification and synchronization of the signal as well as the data. Shortening the burst duration while maintaining the same preamble length therefore results in a reduced data throughput. Consequently, in future high-speed PONs, the question arises as to what extent the preamble can be shortened using blind and digital synchronization procedures. A digital clock synchronization can be implemented either in a feedback architecture based on a phase-locked loop (PLL) or in a fully-digital feedforward architecture. Due to the relatively long acquisition time of the PLL, the latter may not meet the stringent requirements of fast synchronization in burst-switched systems. In contrast to that, feedforward clock recoveries offer instantaneous timing estimation and improved high-frequency jitter performance, especially when using low-cost oscillators. In [186, 187], we analyze a digital feedforward clock recovery and compare it to a digital feedback clock recovery in a 112-Gbit/s PON upstream in C-band using two bursts. Figure 5.4 shows the experimental results obtained for the clock synchronization for alternating 4.5812 μ s-long silent 2-PAM and loud 4-PAM bursts with a burst pause of 0.2 μ s and free-running transmitter and receiver oscillators with a nominal clock frequency offset of 1 ppm. It can be seen that instantaneous timing acquisition is achieved when using a feedforward clock recovery, which enables synchronization within nanoseconds. In this particular example, we used an additional moving average filter for the estimation, which leads to a total synchronization time of 36.57 ns. In contrast to that, the feedback loop converges more slowly for low SNR and stable synchronization starts at the end of the burst. Here, an ideal feedback-loop latency of one clock cycle was simulated. However, in reality, the loop latency can amount tens to hundreds of clock cycles, which significantly deteriorates the stability and convergence speed of the control loop [187]. For this reason, digital feedforward clock synchronization is a promising method to

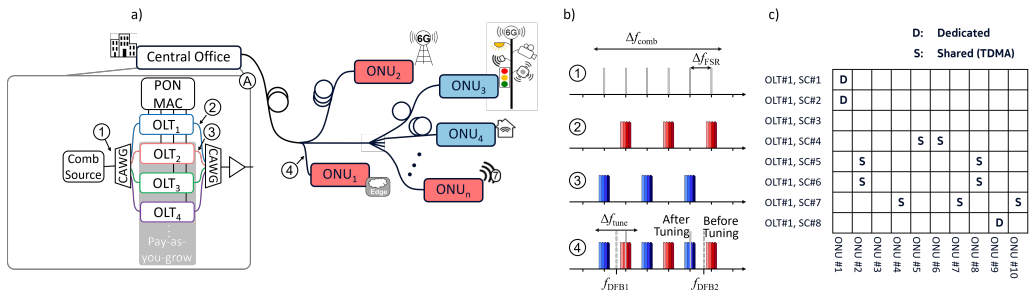


Figure 5.5: Scalable coherent PON. a) Proposed architecture based on digital subcarrier multiplexing and wavelength-division multiplexing addressing the needs of diverse smart-city services. The inset ④ shows the detailed structure of the central office. b) Optical spectra at various positions in the network as indicated by ①, ②, ③ and ④ in a). c) An example of digital subcarrier allocation for OLT₁ to different ONUs.

replace bulky analog clock and data recovery circuits in current PONs by energy-efficient, compact and ultra-fast digital circuits, that furthermore allow a reduction of the preamble length.

5.3.3 200 Gbit/s Coherent Subcarrier PON

In metro- and long-haul optical networks as well as data center interconnects, coherent systems have replaced IM/DD systems since they allow increased spectral efficiency by exploiting quadrature and polarization multiplexing of the complex optical field as well as electronic CD compensation. The latter allows to operate the PON outside the occupied O-band frequencies, e.g., in C-band. Furthermore, coherent receivers provide a higher receiver sensitivity [87]. Within the past 15 years, digital coherent transceiver technology has matured significantly in terms of footprint, power consumption, and cost. This poses the question, whether coherent transceivers have the potential to replace IM/DD also in optical-access networks. However, the complexity of coherent transceivers remains significantly higher compared to their IM/DD counterparts. Despite that, the introduction of coherent transceivers could be a potential solution for very high-speed PONs (VHSP), as they provide high sensitivity, flexibility, and a pay-as-you-grow model. The adoption of coherent technology in PON is driven

by its widespread use in the data center market and research breakthroughs that could lead to a further reduction in their cost structures [93, 188]. In recent years, several coherent PON architectures based on simplified and full coherent receivers have already been proposed [70, 189–192], like coherent ultra-dense (UD) wavelength-division multiplexing (WDM) PON in [70], digital subcarrier based P2MP network in [190], and rate-flexible time-and-frequency division multiplexing (TFDM) PON in [191]. Note that, e.g., the simplified coherent receiver based on Alamouti coding represents a trade-off between bandwidth requirements and optical front-end complexity [192].

The requirement for an external cavity laser (ECL) with wavelength tunability, which serves as a local oscillator (LO) at the ONU receiver, is one of the major cost drivers that needs to be avoided. In the KIGLIS project, we explore the scalable coherent PON architecture based on time, wavelength, and subcarrier division multiplexing. The conceptual system diagram is illustrated in Fig. 5.5 a). Note that it is of upmost importance to keep the complexity and cost of the ONU transceivers as low as possible due to the cost restriction. As mentioned above, coherent transceivers typically use ECLs with wavelength locker and temperature control. In the ONUs of a coherent PONs, such frequency stabilized narrow linewidth lasers are prohibited due to their complexity and cost [66]. In the ONU, we therefore share a single DFB laser as LO and as a transmit laser. Typically, ONUs must support a wide temperature range from -40°C to $+80^{\circ}\text{C}$, while the emission wavelength of DFB lasers shifts by about $0.12\text{ nm}/^{\circ}\text{C}$, resulting in a frequency range of 1.8 THz [66, 122]. Using a simple heater or thermo-electric cooler (TEC), it becomes possible to tune the temperature by a few tens of degrees, resulting in a residual frequency range Δf_{tune} of, e.g., 300 GHz . This leads to a wavelength alignment issue for coherent PONs. In [1], we showed that this issue can be overcome by using a frequency comb source in the OLT. As shown in Fig. 5.5 inset ①, a pair of cyclic arrayed-waveguide gratings (CAWGs) is used in the central office (CO) to divide the comb lines with free-spectral range Δf_{FSR} into multiple interleaved wavelength sets which allow scalable pay-as-you-grow WDM. The frequency comb is shared between downstream and upstream,

where it is used as LO. We consider dual-polarization (DP) inphase/quadrature modulators (IQMs) and coherent receivers (CRXs), which can be integrated either in silicon or indium phosphide (InP) as well as an application-specific integrated circuit (ASIC) for the DSP. In upstream, the CRX must support burst-mode (BM) operation. In the OLT, we consider an optical booster amplifier as well as an optical pre-amplifier. As an example, the multiplexing of two wavelength sets corresponding to two independent OLTs, is illustrated in Fig. 5.5 b). The DFB-LOs can be thermally tuned to the middle of the closest copy of the subcarriers, shown in gray vertical lines. Moreover, multiple digitally generated subcarriers are multiplexed, allowing the medium access control (MAC) to flexibly map dedicated subcarriers, e.g., for low-latency virtual point-to-point (P2P) traffic on some subcarriers while other subcarriers are shared among multiple ONUs using TDMA. Figure 5.5 c) shows an example of how the 8 subcarriers of OLT₁ can be allocated across a set of ONUs. This scheme also allows to choose different modulation formats for different sub-carriers based on the channel condition or the capacity-vs.-loss-budget trade-off [193–195].

5.3.3.1 Digital Signal Processing for Subcarrier Based PON

Figure 5.6 illustrates two DSP schemes: (a) and (b) for downstream operation, addressing two different ONU receiver bandwidths. Figure 5.7 shows the DSP chain for upstream operation. The insets display the electrical signal spectrum at various processing stages. Inset ① shows an example of the downstream optical spectrum with three digital subcarriers. Here, Δf_{Sc} and Δf_{Sig} represent the subcarrier spacing and the downstream signal bandwidth, respectively. The initial two DSP blocks are identical across all DSP schemes. Here, single lines represent real-valued signals, while double lines represent complex-valued signals. First, the real-valued electrical signals are normalized, imbalances between the four signals are corrected, and the signals are converted into two complex-valued signals. Finally, polarization skew is compensated in the frontend correction block. Insets ③ and ④ in Fig. 5.6 as well as Inset ① in Fig. 5.7 show the electrical

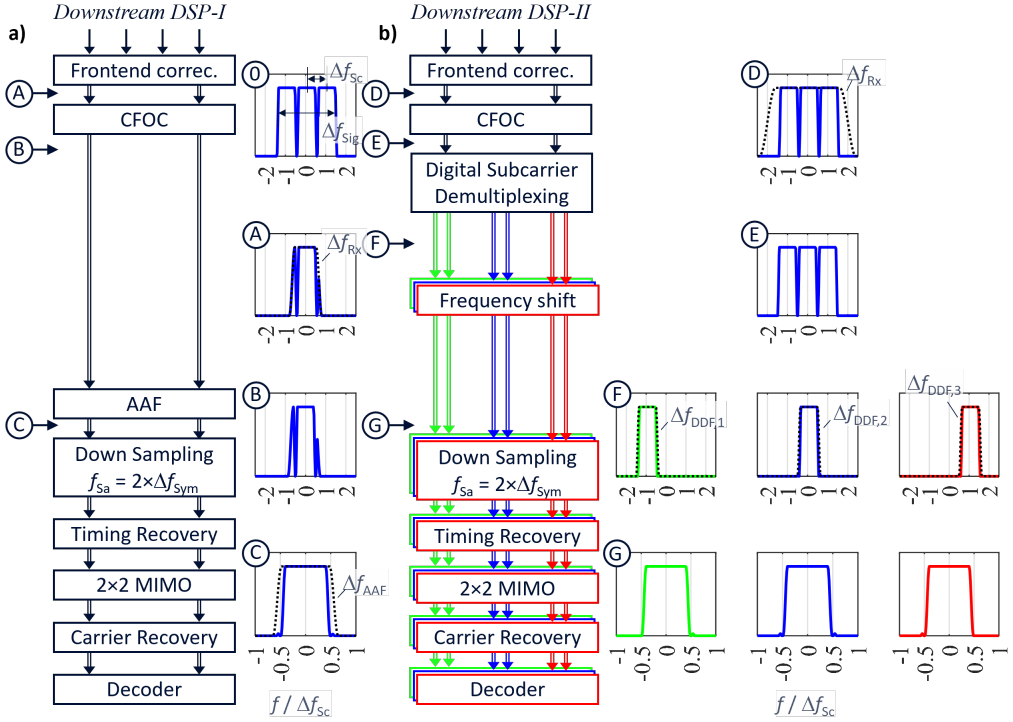


Figure 5.6: shows two different digital signal processing (DSP) schemes for downstream operation. (a) The DSP chain processes a single subcarrier and is identical to a standard coherent DSP. Inset ① illustrates an example of the downstream optical spectrum in the ONU receiver. In this example, three digital subcarriers are considered, with subcarrier spacing of Δf_{sc} . Insets ②–④ depict the electrical spectrum of the signal at various points along the *DSP-I*. The receiver bandwidth and anti-aliasing filter (AAF) bandwidth are indicated as Δf_{Rx} and Δf_{AAF} , respectively. (b) The DSP chain processes two or more downstream subcarriers simultaneously. Insets ⑤–⑫ show the electrical spectrum at different stages in the *DSP-II*. The bandwidth of the digital demultiplexing filter is denoted as Δf_{DDF} .

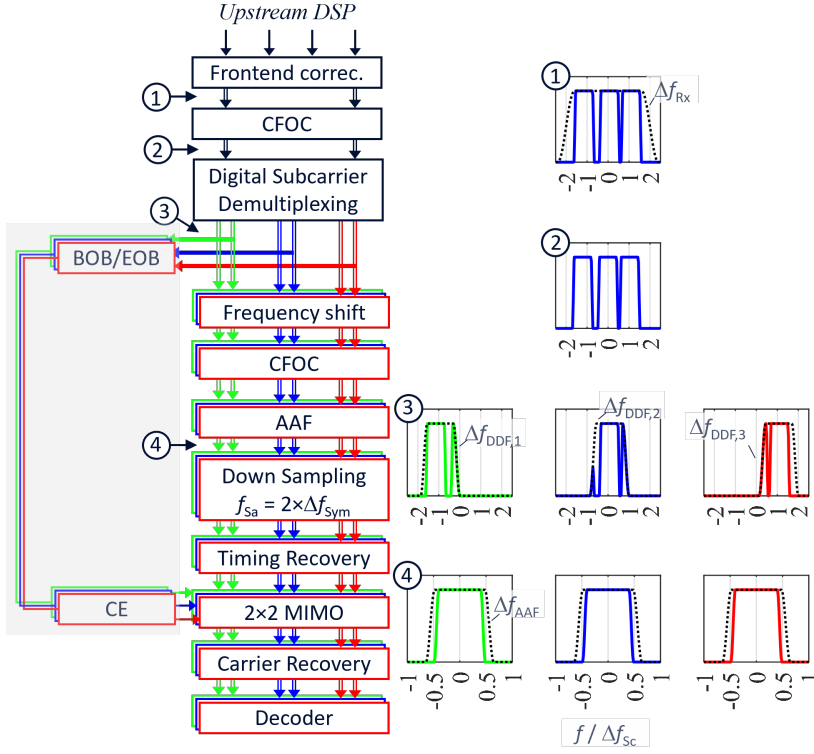


Figure 5.7: shows the DSP scheme for upstream operation. The OLT processes all upstream subcarriers simultaneously. The gray shaded regions represent supporting DSP blocks. Insets ①–④ show the electrical spectrum of the signal at specific locations within the upstream DSP chain.

spectrum after frontend correction. Here, the dashed black lines indicate the two-sided receiver bandwidth of Δf_{Rx} . Next, frequency offset is compensated coarsely in the frequency domain by using the spectral dips, in the coarse frequency offset compensation (CFOC) block [17]. Insets ③, ④ in Fig. 5.6, and ② in Fig. 5.7 illustrate the electrical spectrum after CFOC.

Downstream DSP-I:

Downstream DSP-I is designed for ONUs with a receiver bandwidth slightly greater than the subcarrier spacing ($\Delta f_{Sc} < \Delta f_{Rx} < 2\Delta f_{Sc}$), allowing the reception of at least a single downstream subcarrier. The anti-aliasing filter (AAF) removes unwanted upper and lower frequency components. Inset ㉟ shows the electrical spectrum at the AAF output, with filter bandwidth of Δf_{AAF} . The signal is then down-sampled/up-sampled (depends on the ADC sampling rate) to twice the subcarrier symbol rate of $2\Delta f_{Sym}$. Next, the timing recovery is performed in two steps: in the first step, timing error is blindly detected in the frequency domain using the Barton and Al-Jalili algorithm [131]. In the second step, the timing correction is applied using a seventh-order Lagrange interpolator [20]. Next, a blind equalizer in a 2×2 MIMO configuration compensates for ODN chromatic dispersion (CD) and polarization rotation. An adaptive constant modulus algorithm (CMA) [133] is used to update the MIMO filter coefficients. Carrier recovery is assisted by a 1% data-aided Viterbi-and-Viterbi algorithm, combined with a decision circuit to avoid cycle slips [17]. Finally, the signal is differentially decoded.

Downstream DSP-II:

Figure 5.6(b) shows *Downstream DSP-II*, designed for high-bandwidth ONU receivers ($\Delta f_{Rx} > N\Delta f_{Sc}$), which is capable of detecting N number of subcarriers ($N > 1$). In the digital subcarrier demultiplexing (DSD) block, N digital copies of the signal are created, and digital demultiplexing filters (DDFs) with bandwidths $\Delta f_{DDF,i}$ are applied, where i is the subcarrier index. Inset ㊦ shows the electrical spectrum after DSD. The dashed black lines represent the DDF bandwidths. As the DDFs suppress unwanted upper and lower frequency components effectively; therefore, no AAF is needed in this DSP chain. Each digital subcarrier is then processed in a separate DSP lane, as shown in different colors in Fig. 5.6(b). Next, the subcarriers are shifted to the baseband, as shown in Inset ㊧. The subsequent DSP blocks are identical to DSP-I in each lane. Since

all subcarriers originate from the same transmitter, they share identical timing and phase errors. Thus, these errors can be estimated from one subcarrier and corrected across all lanes, allows for further DSP simplification.

Upstream DSP:

Figure 5.7 presents the upstream DSP for subcarrier based coherent PON. Insets ① and ② show the electrical spectrum before and after CFOC, respectively. In upstream transmission, non-uniform subcarrier spacing ($\Delta f_{sc} + \Delta f_{e,i}$) may occur due to frequency misalignment $\Delta f_{e,i}$ between the ONU transmitter and the LO laser. Therefore, individual subcarrier is processed in an individual DSP lane after DSD, which is similar as *downstream DSP-II*, the details of the upstream DSP are shown in different colors in Fig. 5.7. The shaded blocks represent supporting DSP modules, similar as the DSP chain explained in Chapter 4. A modified complex Golay preamble sequence [164, 166] is used to detect the beginning (BOB) and end (EOB) of the burst. This preamble also enables filter coefficient estimation, frequency offset estimation, and DSP block resetting; check the DSP section of Chapter 4 for detail. Inset ③ shows the electrical spectrum at the DSD output. Due to possibility of having a frequency misalignment, the DDFs require redundant bandwidth. Another CFOC compensates for $\Delta f_{e,i}$ following a constant frequency shift of $-i\Delta f_{sc}$ to bring down the subcarriers to the baseband. The AAF then filters out unwanted frequency components. Inset ④ shows the spectrum at the AAF output. The remaining DSP processing steps are the same as in DSP-I and DSP-II.

5.3.3.2 Experimental Results on Subcarrier-Based Downstream

The proof-of-concept experimental setup for downstream operation is shown in Fig. 5.8. In the Central Office (CO), where OLT is located, we employ a mode-locked laser diode (MLLD)-based frequency comb laser as the transmit laser, as well as an external cavity laser (ECL) as a reference transmit laser

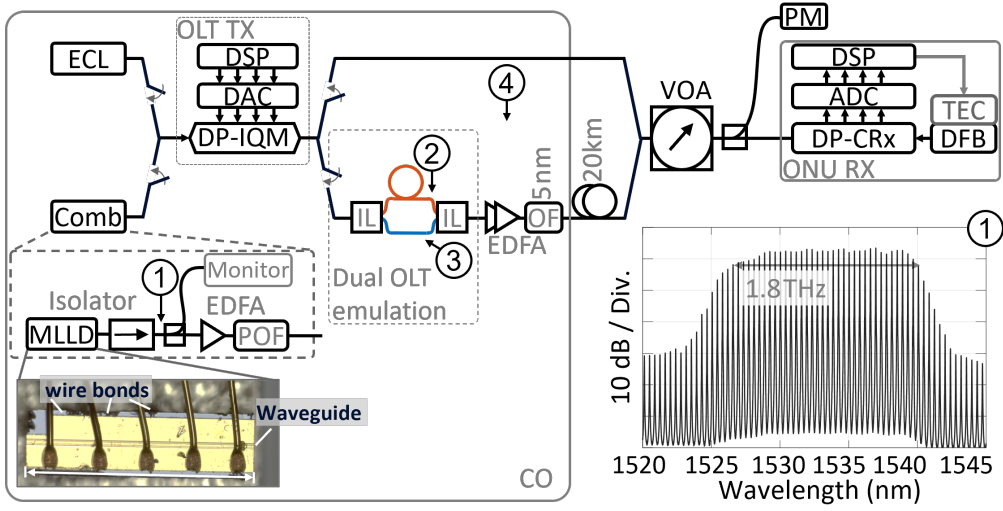


Figure 5.8: Setup of the proof-of-concept experiment for downstream operation. Inset ① shows the frequency comb spectrum emitted by the MLLD, measured at position ①.

in different experiments. A microscope image of the MLLD is shown at the bottom of Fig. 5.8. An optical isolator is used to prevent back reflections, which allows to get optimum performance of the MLLD. The measured optical power at the output of the isolator is 5 dBm with a laser drive current of 200 mA at room temperature. The measured optical spectrum at position ① in Fig. 5.8 is shown in Inset ①. It shows a 5 dB bandwidth of 1.8 THz and a line spacing of $\Delta f_{\text{FSR}} = 49.85$ GHz. A 90/10 optical splitter is used, where 10% of the signal is directed to a comb monitor, and the remaining 90% is amplified using an erbium-doped fiber amplifier (EDFA) for use in the transmission setup. A programmable optical filter (POF) is employed to equalize the EDFA gain tilt and to select desired number of comb lines, thereby emulating the wavelength multiplexing of two OLTs using a delay-and-add configuration, a similar setup also explained in Chapter- 4 as well. In the digital domain, we generate eight subcarriers on a $\Delta f_{\text{Sc}} = 3.4375$ GHz grid and modulate them with random QPSK symbols at 3.125 GBd, shaped by a root-raised cosine filter with a roll-off factor of 0.1. These digital subcarriers are modulated onto the comb lines using a dual-polarization in-phase/quadrature modulator (DP-IQM). The modulated signals

are then de-interleaved using a 50 GHz optical interleaver. A 250 m optical fiber is used in the upper arm, while the lower arm has no fiber, effectively decorrelating the signals and emulating two WDM channels corresponding to OLT_1 and OLT_2 . The measured optical spectrum of emulated OLTs are shown in Inset ② and ③ of Fig. 5.9 (a), measured at positions ② and ③ in Fig. 5.8. The zoom shows the detail of subcarriers. The two arms are recombined using another 50 GHz interleaver. The combined emulated optical-spectrum from OLT_1 and OLT_2 is shown in Inset ④ Fig. 5.9 (a), measured at positions ④ in Fig. 5.8. In back-to-back measurements, the dual OLT emulation section is bypassed. Subsequently, two cascaded EDFAs are employed to study the optical launch power. A 5 nm optical filter is used to emulate the coexistence element in the PON setup. The optical distribution network (ODN) is realized by using 20 km of standard single-mode fiber (SSMF) and a variable optical attenuator (VOA). At the ONU receiver, we use a 25 GHz dual-polarization coherent receiver (DP-CRx) followed by an analog-to-digital converter (ADC) to detect the downstream signal. A distributed feedback (DFB) laser is used as the local oscillator (LO) at the ONU side. In Fig. 5.9(b), we present a microscope image of the packaged InP DFB laser chip along with a plot of its wavelength shift versus ambient temperature, showing a linear drift of 0.12 nm/°C.

Figure 5.10 shows the downstream experimental results. As a reference, an ECL at 1535.5 nm is used as the transmit laser at the OLT side, and a second ECL is used as the LO at the ONU side. Figure 5.10(a) presents bit-error ratios (BERs) versus the average received optical power (ROP) per subcarrier in back-to-back measurements. A receiver sensitivity of -36.7 dBm per subcarrier is observed. When the LO is replaced with a DFB laser, a 1.5 dB penalty is observed due to increased phase noise. Next, the ECL transmitter is replaced with the amplified and filtered MLLD. Two wavelength-multiplexed OLTs, each with five signal copies, are emulated, showing negligible sensitivity degradation. In the next experiment, the system performance is also evaluated over 20 km of SSMF with a total ODN loss of 31.7 dB. Note that the total transmitted power is 19 dB higher due to the transmission of 80 subcarriers in total. As shown in Fig. 5.10(b), no

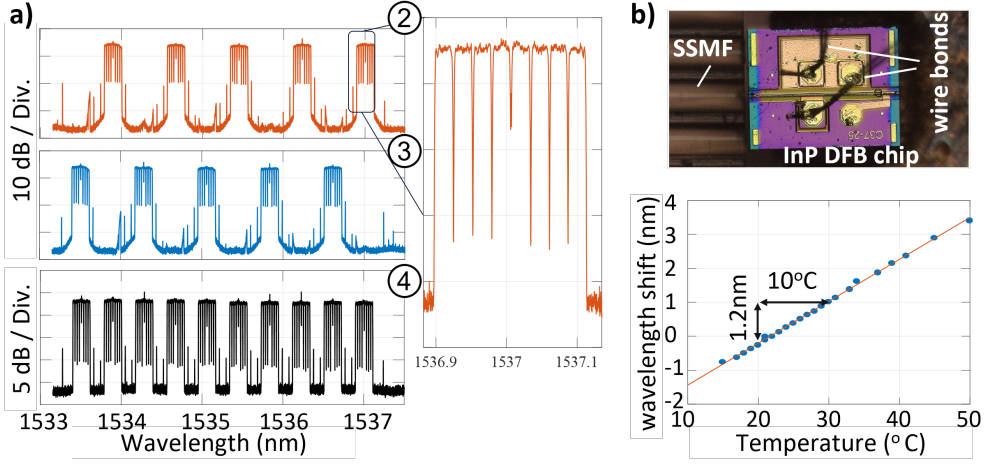


Figure 5.9: (a) Optical spectra measured at positions ②, ③, and ④ in Fig. 5.8 (b) Microscope image of a packaged InP DFB laser chip and its wavelength shift with ambient temperature.

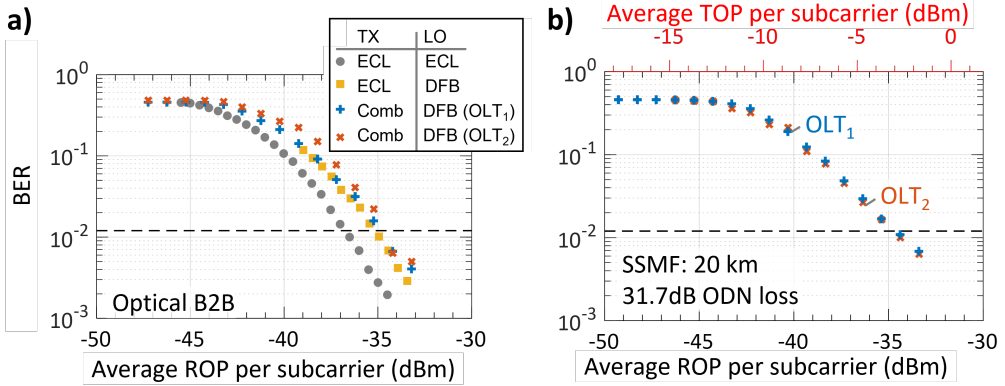


Figure 5.10: Experimental results for downstream transmission. (a) Measured BER as a function of the average received optical power (ROP) per subcarrier for different combinations of transmit and local oscillator (LO) lasers. (b) BER versus received and transmitted optical power (TOP) per subcarrier, averaged over all 8 subcarriers centered around 1535.06 nm (OLT₁) and 1535.45 nm (OLT₂).

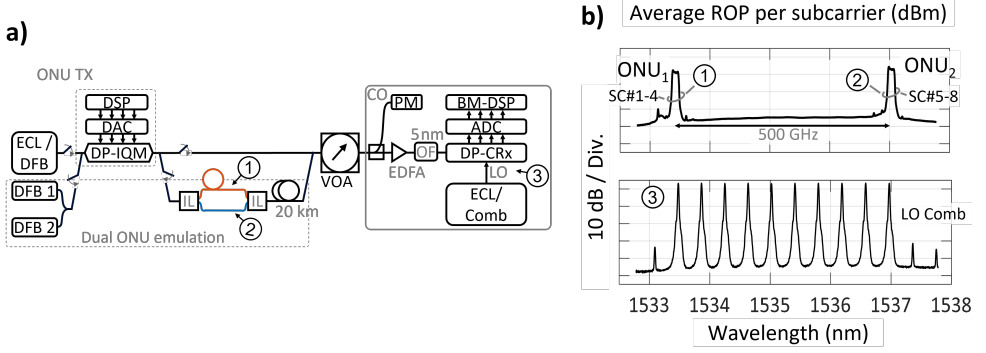


Figure 5.11: (a) Setup of the proof-of-concept experiment for upstream operation. Inset ① shows the frequency comb spectrum emitted by the MLLD, measured at position ①. (b) Top: measured optical spectrum at the OLT for upstream with two ONUs having a frequency spacing of 500 GHz, measured at position ① and ②. Bottom: optical spectrum of the filtered frequency comb used as LO in the OLT, measured at position ③.

additional penalty is observed even at high launch powers, enabling support for a 35 dB loss budget. With a total launch power of 16 dBm and assuming a forward error correction (FEC) threshold of 0.0125, successful downstream operation is demonstrated at an aggregate bit rate of 200 Gb/s.

5.3.3.3 Experimental Results on Subcarrier-Based Upstream

The proof-of-concept experimental setup for upstream transmission is shown in Fig. 5.11. At the ONU side, we employ DFB lasers as transmit laser. In this setup, two ONUs are emulated, each modulating four subcarriers using two DFB lasers operating at optical carrier frequencies approximately 500 GHz apart. Here, the frequency offset between two carrier-frequencies is an example to illustrate the emission wavelength band of DFB lasers. Next, a delay-and-add configuration is used to emulate simultaneous transmission from both ONUs. For comparison, we also evaluate system performance using an ECL as the transmit laser. No optical amplification is applied at the ONU side. Instead, an EDFA-based pre-amplifier is placed at the OLT receiver to boost the upstream signal. The resulting upstream optical spectrum is shown in Fig. 5.11(b), along with the ten comb

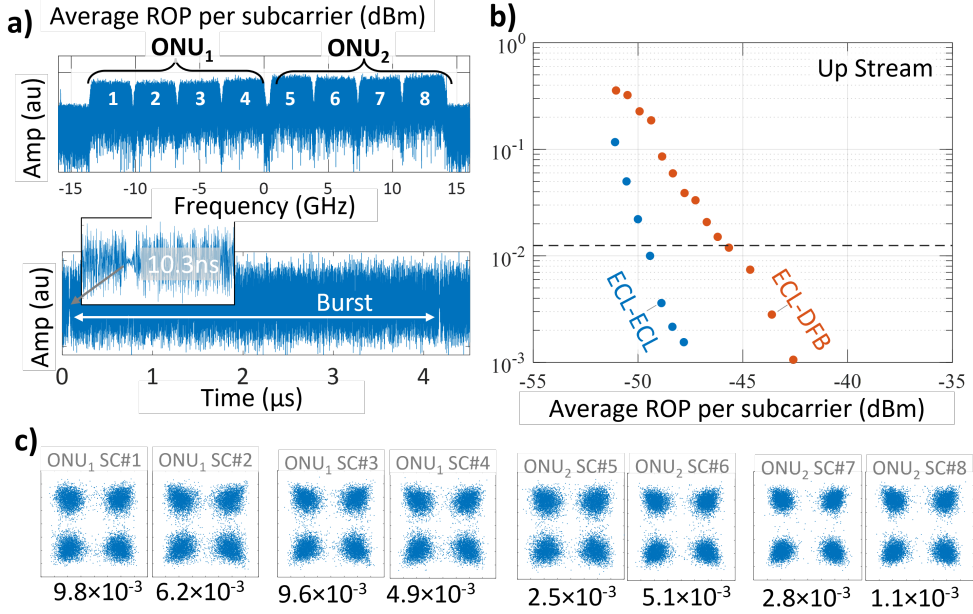


Figure 5.12: (a) Electrical spectrum of the received upstream signal including subcarriers from both ONUs. Bottom: time-domain waveform of subcarrier 1 including a 10.3 ns-long inter-burst gap. (b) Measured upstream BER as a function of the average ROP per subcarrier averaged over all 8 subcarriers for different combinations of transmit and LO lasers. (c) Constellation diagrams and corresponding BERs obtained for the different subcarriers in one of the two polarizations.

lines used as LO. As shown, subcarriers 1 to 4 are centered around 1533.5 nm, while subcarriers 5 to 8 are centered around 1537 nm, which corresponding to an optical frequency spacing of approximately 500 GHz and representing two ONUs. The corresponding electrical spectrum is shown in Fig. 5.12(a), along with an example time-domain waveform in the bottom. Here, the inter-burst gap is approximately 10.3 ns. Non-uniform frequency spacing between subcarrier 4 and 5 represents $\Delta f_{e,i}$; here, i is 2, representing ONU₂. In the first experiment, we study the receiver sensitivity. Figure 5.12(d) shows the BER performance for two different combinations of transmit and receive lasers as a function of ROP. A 4 dB degradation is observed when using the DFB laser as the transmitter, which we attribute to the increased phase noise and intensity noise associated with

DFB sources. Finally, Fig. 5.12(c) presents the received constellation diagrams and corresponding BERs for all eight subcarriers at a received optical power of -22 dBm. Here, the subcarriers 1-4 and 5-8 represents upstream signal from ONU₁ and ONU₂, respectively. We obtain BERs below the pre-FEC threshold for all subcarriers.

5.3.4 Dense Network Monitoring

With increasing connectivity in smart cities, the fiber-optic network is expanding as well. This requires PONs with up to 256 network users [185]. Monitoring and maintaining such large networks is a challenge for network providers. We envision that future sustainable smart cities will employ AI-based PON/ODN monitoring. Figure 5.13 a) shows one possible AI implementation, where different types of current data (such as: optical time-domain reflectometer (OTDR) traces, transmission convergence (TC) layer data and physical (PHY) layer data) and historical data (such as: event simulation, network simulation, deployment data, historic OTDR traces, TC layer data, PHY layer data, etc.) are used. It will employ a sense, think, and act methodology. Currently, OTDRs are often used by network operators for fiber diagnostics and trouble-shooting. Such devices emit short laser pulses into the fiber and then detect the power of back-scattered and back-reflected light. With knowledge about the deployed fiber type, a measurement of the associated time of flight can be used to generate a trace profile of the fiber. This trace comprises distinct peaks resulting from strong back-reflections at splitters, connectors, fiber breaks, and fiber endpoints, see Fig. 5.13 b). By comparing OTDR scans at different times, fiber breaks can be detected as suddenly appearing anomalies. However, straight identification of failures in the fibers connecting the ONUs to the feeder fiber (drops) are difficult to locate since light is reflected from all drops to the OLT simultaneously. Typically, this issue is cleared up by affected customers reporting a loss of Internet connection via another intact communication channel. However, such customer feedback will lack as soon as machines are connected to the ONU and no human users are

present. A second challenge is given by the fact that OTDR measurements only detect existing fiber damages, but do not provide any means for failure prediction and prevention. Machine learning (ML) algorithms are predestined to address both of these challenges. In order to determine the exact location of fiber damage behind a passive splitter, ML algorithms consider OTDR traces as well as network deployment data (e.g., fiber lengths, splitting ratio, and component location) to make predictions on which OTDR events originate from which drop. Towards this goal, we investigate the task of OTDR event classification, i.e., assigning an event class (reflection, attenuation, or no event) to each of the discrete time steps in an OTDR trace. We compare the performance of an ML model against a simple heuristic baseline. Our baseline model predicts events based on a set of heuristic rules defined on the rate of change in the OTDR trace's power level. For our ML model we use a random forest [196], a model that learns and averages over multiple classifiers to improve stability. We use an ensemble of 50 classifiers which, like the baseline, take the rate of change in power level as input. Evaluating both models on 180 OTDR traces from a 1:8 point-to-multipoint PON, we measure precision and recall scores (reported as the macro average over all classes) of 52% and 69% for the baseline and 98% and 95% for the ML model. For the ML model this tells us that, averaged over all three classes, in 98% the predicted class assignment is correct, and 95% of all time steps per event class are retrieved correctly. In [197], we report the detail about the ML approaches for OTDR diagnoses in PON. To enable permanent monitoring of the fiber-optic network with network anomalies forecasting, neural networks can be trained on large quantities of historical records comprising time series of OTDR measurements and associated network faults. By training on such data, predictions can be made to forecast future network faults and intervene before they occur.

5.4 Network Resource Allocation

High quality of experience (QoE) is of great importance in a smart city network as users demand seamless delivery of services across various network segments such

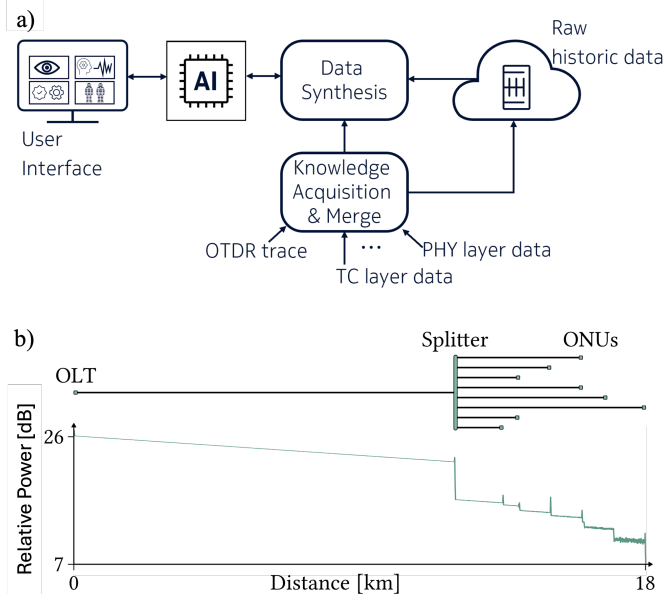


Figure 5.13: Dense network monitoring. a) Concept for AI-based PON/ODN monitoring. b) An example of an ODN with corresponding OTDR trace.

as regional data centers, wireless networks, and PONs. Smart city applications and services lead to a traffic mix with diverse demands which require optimized resource allocation schemes across fixed and wireless converged network elements. For example, the occupants of automated shuttles rely on high-capacity broadband connectivity for entertainment and business applications, while the vehicles themselves need a latency of 1 ms or even lower and a high-bandwidth connectivity to gather information about their environment. In our work on resource allocation inside the smart city network, we particularly focus on the PON upstream path that is often considered as the latency bottleneck because of associated waiting times for ONUs to acquire network access in a TDMA scheme. The ONUs have traffic bearing entities called transmission containers (T-CONT) that are the lowest granularity of service differentiation for bandwidth provisioning by a centralized dynamic bandwidth assignment (DBA) process in the OLT. T-CONTs can be assigned with different traffic descriptors related to bandwidth, delay properties, and prioritization. The DBA process in PONs is conceptually composed of two main components: the bandwidth assignment to

each T-CONT per ONU, and the bandwidth map (BWmap) generation for organizing the upstream data transport across all ONUs according to the overall bandwidth assignment [75].

In order to study the latency and bandwidth statistics, we simulated the resource allocation in a PON which provides fiber connectivity for wireless antenna sites in a fixed-wireless converged architecture. As vehicles and their wireless user entities (UEs) move inside the smart city, the UEs need to be dynamically connected and handed over from one wireless access point to another. This also implies the reconfiguration of the related wireless processing elements at the antenna site and associated optical endpoints, i.e., ONUs and T-CONTs. To enable best-in-class QoE, an efficient and proactive resource allocation for the different ONUs and T-CONTs under the dynamically changing mobility and traffic patterns is desirable. Thus, we propose to not follow the reactive measures initiated from wireless hand-overs to the PON, but to incorporate the knowledge of locomotion patterns to predict the UE mobility. From the family of process mining methods, we applied process discovery [198], to generate a Markov chain about mobility patterns. This prediction of the mobility patterns can be used to create, provision and release T-CONTs. If a user (car) is connected to an AP and this way to an ONU (associated with the 2 different service classes represented by different T-CONTs), the OLT starts the creation and provisioning of T-CONTs (ONU-AP) for the most probable path from the current ONU (+AP) for the deterministic service requirement using the same BW as allocated to the current ONU T-CONT. This follows the assumptions of a constant bandwidth demand for this deterministic and time critical service. In all other ONUs connected to APs around the currently connected AP-ONU, a handover (backoff) T-CONT were created that could be provisioned quickly if a wrong mobility path prediction were made. The pre-conditioning of the best effort traffic is assumed time uncritical and will thus follow the allocations of the remaining bandwidth of the PON link after taking into account all deterministic (assured) bandwidth of all users in the PON, the pre-provisioning and the demand of all other users on this best effort service category.

In our simulation, we consider two service types: ultra-broadband non-time critical services and medium-to-low capacity time-critical services. Furthermore, we specify three different resource allocation scenarios: a) static initialization of the T-CONTs at each ONU, b) full knowledge of mobility pattern and thus dynamic creation, provisioning, and release of T-CONTs, and c) mobility pattern prediction and thus dynamic creation, provisioning, and release of T-CONTs at ONUs along the most probable paths of the vehicles (UEs). One OLT is connected to 20 ONUs and 100 vehicles (UEs) use the two service types to generate data requests for the T-CONTs at the ONUs. The path prediction of vehicles (UEs) applied in the resource allocation simulation is obtained by monitoring the connectivity of UEs to the Wi-Fi access points within the city of Karlsruhe, Germany. Event tables are generated from which transition probabilities between wireless access points and hence connected ONUs are calculated as shown in Fig. 5.14. The simulation reveals that the static T-CONT allocation applies a large over-subscription, which leads to a high bandwidth allocation of 110%, but allows very low latencies since the requested bandwidth is permanently available. Bandwidth allocation can be improved for broadband services to 10% and 50%, and for time-critical services to 25% and 88% for the dynamic T-CONTs with known path and predicted path, respectively. For time-critical applications, the defined latency can be ensured with 0.5 ms for the known path, while it is close to the requirement with 1.4 ms for the predicted path. Broadband services even improve the latency from 7.5 ms (static T-CONT) to 6.3 ms for the known path but worsen it to 166 ms for the predicted path. The latter can be improved by further optimization of the mobility pattern prediction and therefore provide even more benefits for PON resource allocation.

5.5 Fiber Network Deployment

Future smart cities require densely-spaced small cells, sensors, and regional data centers, all of which may become fiber endpoints. However, the exact fiber demand of such cities is still uncertain, as it is not yet clear how many of these

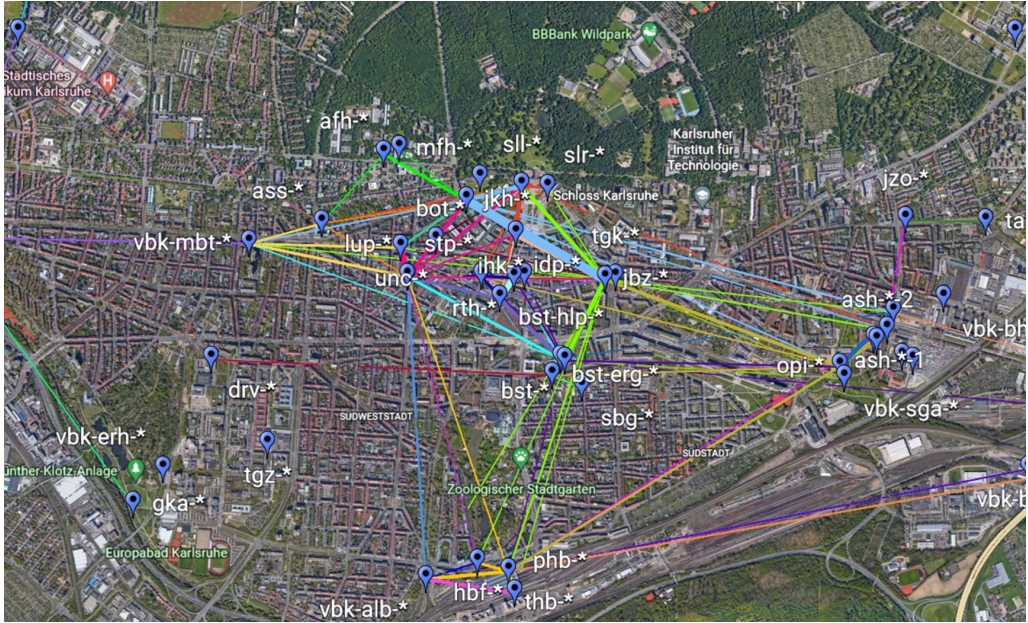


Figure 5.14: Satellite image of the city of Karlsruhe, Germany. The blue pins with name codes indicate the public Wi-Fi access points in the city center. The mobility pattern of vehicles (users) accessing the access points were observed and evaluated. The transitions between the access points are represented by lines, whereby the thickness of the lines visualizes the transition probability.

entities will have to be placed how densely in the environment. Moreover, the financial benefits and potential revenues are intangible for today's investors and public authorities. In fact, there are few, if any, network operators that would include traffic, street lights, or road intersections as fiber endpoints in their current fiber rollout plans. At the same time, the fiber rollout to connect homes, businesses, and public buildings in Europe is gaining significant momentum. While for instance countries such as Germany with only 40.3% and the UK with 57% still lag behind in the fiber-to-the-home/building (FTTH/B) coverage rates, they are now among the three fastest growing FTTH markets, both in volume and percentage [199]. Since fiber deployment involves a considerable amount of work and costs, it is crucial to sustainably consider the potential future demands on the optical network.

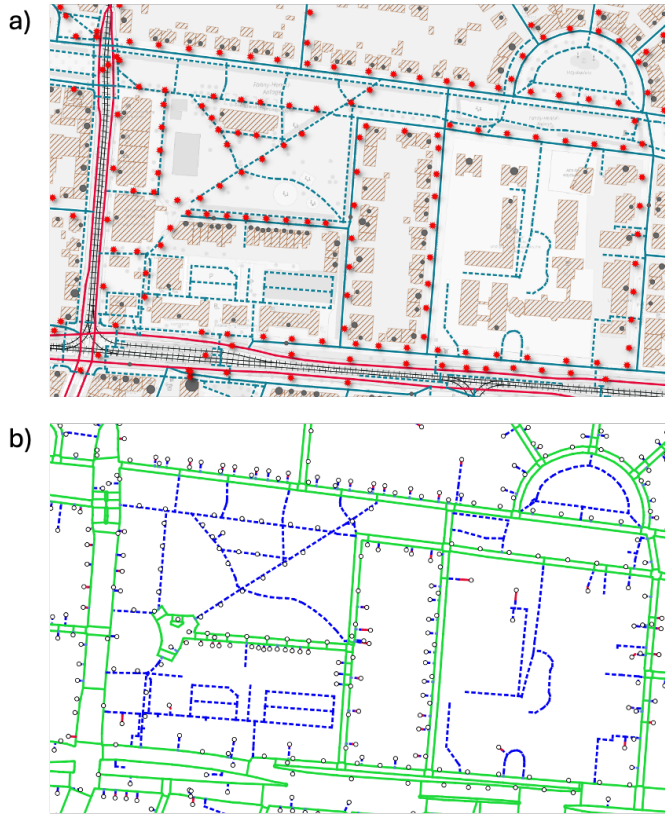


Figure 5.15: From raw data to a routable base network, Karlsruhe-Weststadt. (a) residential roads (blue), footways, paths (blue, dashed), major streets (red), railroads/tram (black), building outlines (brown), addresses (grey dots increasing in size with the number of households/businesses), street lights (red stars) (b) Generated base network of potential routes: public street sides and potential street crossings (green), drop/private routes (blue dashed), inhouse connections (red).

In the following, we present a techno-economic study, which shows that even a small increase in today’s investments for fiber access can lead to a significant expansion of future opportunities. We optimized and compared different scenarios of fiber access networks for the western part of the city of Karlsruhe, Germany (see Fig. 5.15 and Fig. 5.16). The calculations were performed using the commercially available software application *atesio-fttx-optimizer-strategic* [200], an optimization framework to compute FTTx rollout plans, which is already in productive use at several international telecommunication operators.

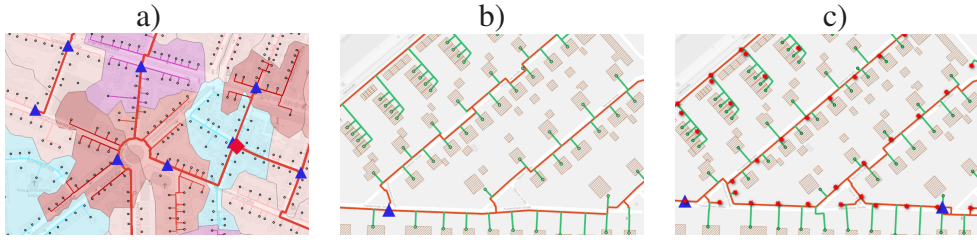


Figure 5.16: Fiber access network in Karlsruhe. (a) Feeder cables (red lines) with fiber distribution points (blue triangles) connected to the central office (red diamond) and optimized distribution clusters (colored fields). (b) FTTH: the red and green lines show the routed ducts/cables for homes-passed and homes-connected paths, respectively. (c) FTTH + street light: the red stars show the street light fiber endpoints. The increased fiber demand requires an additional distribution point and slightly different routing compared to (b).

The study is mainly based on public available information. We gathered data from 1700 addresses (Nexiga) in Karlsruhe, encompassing a certain number of households and business units each, the location of 500 street lights (public utility of Karlsruhe), and public infrastructure information from OpenStreetMap (OSM) [201], including streets, railroads, waterways, and building outlines.

In a first *infrastructure derivation step*, as depicted in Fig. 5.15, the atesio engine combines all raw data to compute a routable base network. The process entails providing two street sides starting from OSM street center-lines, introducing potential street crossings, and connecting all demand entities (addresses, street lights) with the base network. Additionally, a cost model is applied to all potential route segments, including trenching and crossing costs depending on street types, as well as railroad crossing costs, as outlined in Table 5.1.

In a second *optimization step*, an FTTH network is computed and embedded into the route network, see Fig. 5.16. We consider a greenfield scenario with typical equipment costs and a common network architecture.

That is, the distribution area is a PON, where each demand site is connected to a fiber distribution hub using 1/12/24 pipe microduct trees and 6-to-48-fiber point-to-point blown-in micro-cable routing. Each household is supposed to get one fiber while two fibers are provided to individual business units. An address

Table 5.1: Cost of considered connection entities. f: fiber.

Cable Cost euro/m	
Distribution 6f/ 12f/ 24f/ 48f	1.56/ 1.66/ 1.75/ 1.9
Feeder 48f/ 96f/ 192f/ 288f	2.72/ 2.84/ 3.5/ 4
Duct Cost euro/m	
Distribution 1×6/ 12×6/ 24×6 mm	1.8/ 4/ 6.4
Feeder 4×10/ 7×10 mm	3/ 3.75
Street Side Trenchning Cost euro/m	
Private paths, footways, tracks	60
Residential, living streets	100
Major roads (primary, secondary)	120
Street Crossing Cost euro/m	
Residential, living streets	100
Major roads (primary, secondary)	150
Railroad Crossings Cost euro/crossing	
Tram	10,000
Railway	25,000

is supported with at least one cable and hence at least 6 fibers. The scenario with connected street lights also provides each of these sites with a 6f cable. The PON splitting hierarchy depends on the demand site. Fiber connections for addresses with up to 24 households and also street lights are splitted 32:1 at the fiber distribution hub. For bigger addresses with more than 24 resident units a 4:1 splitting in the building is followed by a 8:1 splitting at the fiber distribution hub. Business units get a point-to-point connection to the central office. The fiber distribution hubs are connected in the feeder area with conventional cable trees and ducts to a an optical distribution frame (ODF) at the central office (CO). The corresponding cost-model is stated in Table 5.1 (cables, ducts, and trenching) and Table 5.2 (network equipment).

The goal of the atesio engine *atesio-fttx-optimizer-strategic* is to compute a cost-optimized network. In order to achieve this objective, the software combines

Table 5.2: Cost in euro of considered node network equipment.

Demand sites	
House connection	100
Splitter 1:4	120
Distribution sites	
Splitter 1:8/ 1:32	180/250
Fiber distribution hub	
48/ 72/ 96 ports	2,000/ 3,000/ 4,100
Central office	
ODF 2,500/ 5,000 ports	25,000/ 30,000
Infrastructure sites	
Manhole	3,000
Fiber closure	1,000
Splice	10

algorithmic intelligence and mathematical optimization solving a wide range of decision problems, from clustering (distribution areas) and routing (fibers, cables, ducts) to network design and flow problems.

The results of the study are depicted in Table 5.3 and Table 5.4 for three scenarios, a pure FTTH approach connecting addresses only (FTTH), a second scenario that connects both addresses and street lights in a common PON (FTTH + Street Lights), and a third scenario that enriches the pure FTTH scenario with additional duct pipe reserves (FTTH + Reserves). Independent of the scenario, the total cost of the fiber rollout is clearly dominated by trenching, accounting for 79%-80% of the homes-passed network (i.e., fiber deployment in public streets only, excluding dedicated connections to individual demand sites) and 73%-75% of the full FTTH deployment (homes-connected). The homes-passed deployment takes 68%-72% of the cost, compared to the full homes-connected network. Comparing the first two scenarios, it turns out that the supplementary expense of integrating street lights along with addresses amounts to a mere 3.6% in the homes-passed cost. This might seem surprisingly small but is due to the fact that street lights in a

urban areas are in close vicinity to the network that is routed along the sidewalks, see Fig 5.15 a) and Fig 5.16 b) and c). However, for the full FTTH deployment, incorporating street lights in addition to addresses results in a 9% cost increase due to the additional expense of last-meter excavation and exclusive point-to-point cabling.

In the third scenario, the street lights have been omitted in the planning but extra pipe reserve capacity has been considered. Four out of twelve duct pipes have been kept free in the distribution area, providing 850 additional and evenly distributed reserve pipes along the homes-passed architecture. Therefore, more than 50% additional sites can be connected if the need exists without additional costs in (homes-passed) deployment. Each of these 850 pipes could accommodate a fiber cable with up to 72 fibers, ensuring a highly sustainable investment with considerable flexibility in future smart sustainable cities. Such a reserve-enriched network configuration results in a homes-passed cost increase of just 3.3%, demonstrating that explicit inclusion of highly uncertain fiber endpoints, such as street lights, is not necessary in the planning process. Instead, it suffices to provide sufficient reserves in the currently built homes-passed networks. This already greatly increases the chance of supporting future smart city applications and means sustainable planning without over-investment.

Table 5.3: Cost in euro of the homes-passed share of the FTTH network.

	FTTH	FTTH+ Street Lights	FTTH+ Reserves
Locations	584,390	633,020	602,360
Cables	62,862	55,956	70,299
Ducts	150,348	168,836	165,272
Trenching	3,126,518	3,211,177	3,217,357
Sum	3,924,118	4,068,988	4,055,288

Table 5.4: Cost in euro of the all-connected FTTH network.

	FTTH	FTTH+ Street Lights	FTTH+ Reserves
Locations	827,430	927,820	845,420
Cables	357,984	440,616	359,100
Ducts	193,282	224,662	208,699
Trenching	4,082,661	4,370,627	4,210,922
Sum	5,461,357	5,962,725	5,624,141

5.6 Remote Assistance

Autonomous vehicles will occasionally require human support in challenging situations, such as traffic accidents, emergency scenarios or construction zones, as explained in Fig. 5.1. Remote assistance for autonomous driving in an emulated traffic situations has been successfully demonstrated as a use case for smart cities in the KIGLIS project [202]. The demonstration setup for remote monitoring and assistance of an autonomous vehicle using a PON-based point-to-multipoint system is shown in Fig. 5.17. In this demonstration, we employ a XGS-PON OLT in the control center and XGS-PON ONUs in the remote node. In this field demonstration setup, the XGS-PON ONUs are connected to different wireless network infrastructures and EDGE cloud. The intelligent infrastructure consists of various surveillance systems and sensors. The communication infrastructure employs public radio frequencies, such as WiFi technology, to communicate with the autonomous vehicle. A picture of the control center and the fully-connected autonomous vehicle is shown at the bottom of Fig. 5.17. A prerequisite for the remote assistance is the transmission of high volumes of sensor data from the fully-connected autonomous vehicle over the PON infrastructure, and, if applicable, from the infrastructure sensors as well. In order to ensure real-time transmission in a future smart city, which will have a high number of connected units and thus high communication traffic, we have investigated and developed various methods

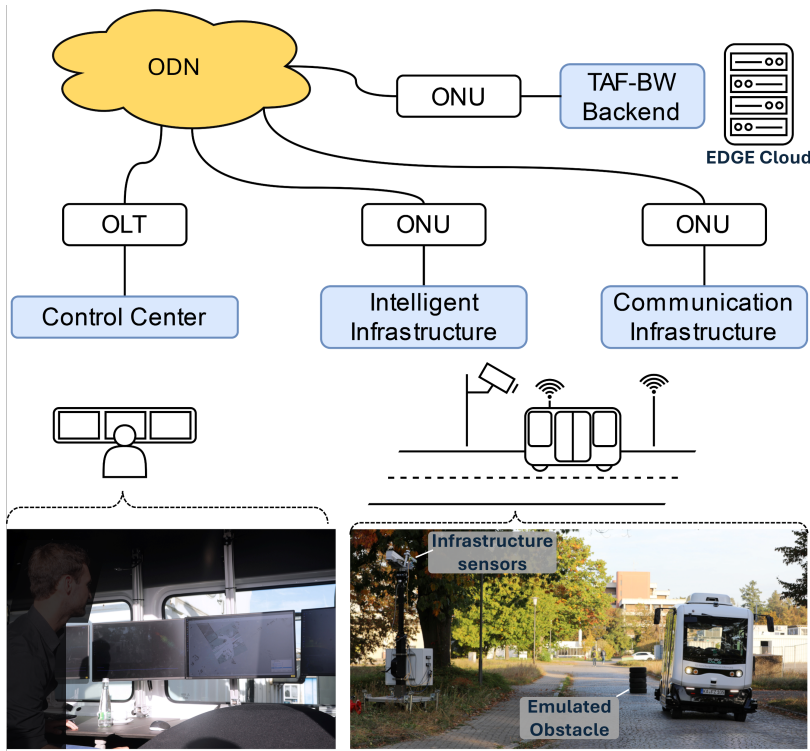


Figure 5.17: Demonstration setup of the remote assistance of an autonomous vehicle by a remote control center as a typical smart-city use case.

dedicated to autonomous driving. This includes AI-based compression methods for lidar and camera data. In [203], the project explored the use of deep generative neural networks for compressing sensor data, achieving better reconstruction quality compared to traditional methods like JPEG. Specifically, variational autoencoders (VAEs) and generative adversarial networks (GANs) were utilized to compress both lidar and image data, ensuring efficient data transmission without overloading the network infrastructure. The implemented compression methods demonstrated promising results in maintaining data integrity and quality necessary for remote assistance. In combination with the network infrastructure, it was possible to give a successful demonstration of the explored methods in the Test Area Autonomous Driving Baden-Württemberg (TAF-BW). The integration of cooperative perception, involving data from multiple sources like infrastructure

sensors and other vehicles, proved to enhance the overall reliability and efficiency of the remote assistance system.

During the field test, the setup involved an autonomous shuttle operating within the TAF-BW, a semi-private test area equipped with various infrastructural sensors. The simulated problem scenario involved placing a static obstacle in the path of the autonomous vehicle, requiring it to switch from autonomous mode to remote assistance mode to navigate around the obstacle safely, see Fig. 5.17. The remote operator, situated in a control center, used the real-time data transmitted through a PON from the vehicle's sensors and additional cooperative perception inputs to guide the vehicle around the obstacle. This setup allows to demonstrate the capability for event detection and remote monitoring over a live optical network for an autonomous traffic system.

Additionally, the scalable remote operation system outlined in [202] was utilized during the field test. This system, which integrates cooperative perception and open-source communication modules, ensures robust and efficient data exchange between the autonomous vehicle, control center, and external sensors. The communication system is based on the Robot Operating System (ROS) and utilizes a Docker container for ease of deployment and maintenance, ensuring scalable and adaptable communication across various network configurations.

In conclusion, we showcased the practical viability of remote assistance for autonomous vehicles, highlighting the importance of advanced data compression techniques and cooperative perception in maintaining robust and efficient remote operation systems.

5.7 Conclusion

Emerging smart city applications, such as connected driving, place stringent demands on the optical-access network. We demonstrate that a 100-Gbit/s IM/DD and 200-Gbit/s coherent PON can fulfill these requirements. Furthermore, we demonstrate that OTDR measurements can be augmented with ML techniques

to classify OTDR events. In future efforts, more efficient artificial intelligence methods can be used to exploit these results for network failure prediction. We have simulated that DBA, taking into account the mobility behavior of traffic participants, can increase the efficiency of bandwidth allocation and guarantee low latency. Moreover, our cost study on fiber deployment in the German city of Karlsruhe provides impetus for a sustainable fiber rollout that will also meet the future needs of our cities. Finally, we demonstrate in a field test remote operation of a fully-connected vehicle to steer the shuttle around an obstacle in real-time. The comprehensive work from fiber-access infrastructure to fiber deployment and real-world application within the KIGLIS project provides technical achievements and valuable insights on the way to a fully-connected smart and sustainable city of the future.

End of journal [3]

6 Summary

6.1 Summary

Higher-order modulation, such as dual-polarization quadrature phase-shift keying, along with coherent reception, is expected to become essential in future very high-speed PONs. For successful adoption in the cost-sensitive and user-centric access network, coherent transceivers must be simplified and optimized. Furthermore, PON is a P2MP system that allows cost asymmetry: The OLT cost is shared by all users, so designing low-cost ONUs is more crucial for successful PON adoption. It is also crucial that future coherent PONs can leverage existing component technologies from high-volume network segments to minimize NRE costs. Furthermore, future VHSPs must coexist with at least the last three PON standards, and maintaining compatibility with GPON is of particular importance, since GPON is the most widely deployed PON to date. Taking these requirements into account, coherent transceiver designs based on C-band components and simplified, uncalibrated laser-based ONUs are especially promising for PON adaptation. Note that the coherent receivers require an LO that is precisely aligned with the transmitter laser, typically necessitating narrow-linewidth, wavelength-stable sources.

Uncalibrated lasers such as DFB lasers have inherent wavelength uncertainties due to fabrication tolerances. This thesis addresses this challenge and explores the potential of a chip-scale MLLD-based frequency comb in a coherent transceiver design at the OLT. The colorless coherent TDM-PON architecture significantly relaxes the wavelength stability requirements at the ONU, where the ONU laser

can emit anywhere within the bandwidth of the comb without causing substantial performance degradation. The proposed TDM-PON architecture allows for the reception of multiple replicas of the same signal depending on the receiver bandwidth. To exploit this redundant information, we introduce a signal tripling technique combined with maximum ratio combining, implemented using a 6×2 MIMO equalizer. This approach improves the receiver sensitivity by approximately 3 dB. Conversely, receivers with limited bandwidths capture only partial copies of the signal from different comb lines. To address this, we propose a spectrum stitching method based on a 4×2 MIMO equalizer, which enables the reconstruction of partial signals with performance comparable to that of conventional coherent systems.

Future PONs are expected to support diverse applications in terms of data rate, traffic profile and latency. Colorless TDM along with wavelength-division multiplexing allows simultaneous operation of diverse services. In this work, we presented a coherent TWDM-PON using an MLLD-based frequency comb source at the OLT and thermally tuned DFB lasers at the ONUs, where each ONU tunes its DFB LO to the nearest comb line using temperature control, laser bias-current, or a combination of both. Burst-mode DSP was presented in a 200 Gbit/s coherent TWDM-PON scenario.

As mentioned, achieving flexibility at the physical layer is essential for coherent PON to support diverse requirements of future applications. Therefore, introducing flexibility across three relevant domains (time, optical wavelength, and electrical frequency/subcarriers) is of particular interest. Spatial multiplexing is not a viable solution in PON, since it primarily relies on reusing the existing ODNs. This thesis presented a system architecture that supports flexibility in all three key domains. Furthermore, this architecture offers a scalable foundation for future smart city deployments.

6.2 Outlook

The achievements presented in this thesis primarily serve as proof-of-concept demonstrations using discrete, off-the-shelf components. Future work should focus on integration, component tailoring for PON applications, and DSP optimization.

One key direction is the integration of InP-based MLLDs into coherent transceivers. This work explored the potential of frequency combs for PON applications and demonstrated that they enable simplified ONU transceivers. However, moving beyond discrete setups requires tailoring specifically for PON use cases. This includes optimizing the comb laser's output power and carefully balancing the number of comb lines with the emission wavelength or frequency range of uncalibrated DFB lasers. Additionally, integrating the comb source with other components, such as IQ modulators, SOAs, and optical filters, should be achieved through either multi-chip or monolithic integration. Furthermore, chip-scale optical filtering techniques require further investigation, particularly for TWDM and subcarrier-based coherent PON systems.

Another important focus is improving upstream sensitivity. Burst-mode coherent upstream transmission was experimentally validated using a frequency comb LO at the OLT. Since the maximum output power of a comb source is inherently limited, sensitivity at the receiver can be enhanced by employing purpose-built frequency combs with fewer lines but higher output power per line, compared to the MLLD used in the proof-of-concept setups. Additional improvements may also be realized through the use of high-sensitivity photodiodes, upstream pre-amplifiers, or booster SOAs integrated at the ONU side.

A further consideration is the use of uncalibrated DFB lasers in OLTs and ONUs. PON systems traditionally utilize uncalibrated lasers operating in a wavelength band at both ends to minimize costs, while coherent systems typically rely on fully calibrated lasers for precise wavelength matching. A potential compromise

is a leader-follower configuration, in which the OLT acts as the leader and the ONUs adjust their lasers via in-service calibration.

Finally, optimizing DSP for PON is essential. DSP is a fundamental building block of any coherent communication system. For coherent technology to be viable in the PON market, DSP must be simplified and optimized for low power consumption. Moreover, burst-mode operation in upstream transmission introduces new challenges, requiring novel DSP innovations tailored specifically to the characteristics of PON.

Acronyms and symbols

Acronyms

4-PAM	Quaternary Pulse-Amplitude Modulation
5G	Fifth Generation
6G	Sixth Generation
AAF	Anti-Aliasing Filter
ADC	Analog-to-Digital Converter
AI	Artificial Intelligence
AONs	Active Optical Networks
APON	Asynchronous Transfer Mode PON
APD	Avalanche Photodiode
ASIC	Application-Specific Integrated Circuit
ASE	Amplified Spontaneous Emission
ATM	Asynchronous Transfer Mode
AWG	Arbitrary-Waveform Generator
AWGN	Additive White Gaussian Noise
BER	Bit Error Ratio
BM	Burst-Mode

BM-CRX	Burst-Mode Coherent Receiver
BOB	Beginning of the Burst
BPON	Broadband Passive Optical Network
BWmap	Bandwidth Map
CAWG	Cyclic Arrayed Waveguide Grating
CD	Chromatic Dispersion
CF	Crest Factor
CFO	Coarse Frequency Offset
CFOC	Coarse Frequency Offset Compensation
CMOS	Complementary Metal-Oxide-Semiconductor
CO	Central Office
CR	Carrier Recovery
CRX	Coherent Receivers
CMA	Constant Modulus Algorithm
DACs	Digital-to-Analog Converters
DBA	Dynamic Bandwidth Assignment
DD	Direct Detection
DDFs	Digital Demultiplexing Filters
DFB	Distributed Feedback Laser
DPSK	Differential Phase-Shift Keying
DP – IQM	Dual-Polarization In-Phase and Quadrature Modulator
DRBS	Distributed Rayleigh Backscattering

DS	Downstream
DSD	Digital Subcarrier Demultiplexing
DSL	Digital Subscriber Line
DSP	Digital Signal Processor
DWDM	Wavelength-Division Multiplexing
EAM	Electro-Absorption Modulator
ECL	External Cavity Laser
EDFA	Erbium-Doped Fiber Amplifier
EL	Electric Field of Laser
EPON	Ethernet Passive Optical Network
EOB	End of the Burst
ERGO	Erbium Glass Oscillator
ESA	Electrical Spectrum Analyzer
EWR	Emission Wavelength Range
FEC	Forward Error Correction
FFT	Fast Fourier Transform
FO	Frequency Offset
FOE	Frequency Offset Estimation
FSR	Free Spectral Range
FTTH	Fiber to the Home
GANs	Generative Adversarial Networks
GPON	Gigabit-capable Passive Optical Network

HBW-RX	High-Bandwidth Receiver
HSP	High-Speed PON
ICR	Integrated Coherent Receiver
IEEE	Institute of Electrical and Electronics Engineers
IM/DD	Intensity Modulation and Direct Detection
InP	Indium Phosphide
IoT	Internet of Things
I/Q	Inphase/Quadrature
ISI	Inter-Symbol Interference
ITLA	Integrated Tunable Laser Assembly
ITU	International Telecommunication Union
LANs	Local Area Networks
LBW-RX	Limited-Bandwidth Receiver
LO	Local Oscillator
MAC	Medium Access Control
ML	Machine Learning
MLLD	Mode-Locked Laser Diode
MIMO	Multiple-Input Multiple-Output
MSA	Multi-Source Agreement
NG-PON2	Next Generation PON2
NRE	Non-Recurring Engineering
NRZ	Non-Return-to-Zero

OA	Optical Amplifier
OANs	Optical Access Networks
OCNR	Optical Carrier-to-Noise Power Ratio
ODF	Optical Distribution Frame
ODN	Optical Distribution Network
OE	Optical-Electrical
OEO	Optical-Electrical-Optical
OFDM	Orthogonal Frequency-Division Multiplexing
OLT	Optical Line Terminal
ONUs	Optical Network Units
OOK	On-Off Keying
OSM	OpenStreetMap
OSNR	Optical Signal-to-Noise Ratio
OTDR	Optical Time-Domain Reflectometer
P2MP	Point-to-Multipoint
P2P	Point-to-Point
PBS	Polarization Beam Splitter
PC	Polarization Controller
PDs	Photodiodes
PDM	Polarization-Division Multiplexing
PHY	Physical Layer
PLL	Phase-Locked Loop

PM	Power Meter
POF	Programmable Optical Filter
PONs	Passive Optical Networks
PR	Polarization Rotation
QPSK	Quadrature-Phase-Shift-Keying
QD	Quantum-Dash
QoE	Quality of Experience
R-EAM	Reflective Electro-Absorption Modulator
RRC	Root-Raised-Cosine
ROP	Received Optical Power
ROS	Robot Operating System
RX	Receiver
SNR	Signal-to-Noise Ratio
SOAs	Semiconductor Optical Amplifiers
SSMF	Standard Single-Mode Fiber
TAF-BW	Test Area Autonomous Driving Baden-Württemberg
TC	Transmission Convergence
T-CONT	Transmission Containers
TDMA	Time-Division Multiple Access
TDM	Time-Division-Multiplexed
TEC	Thermo-Electric Cooler
TFDM	Time-and-Frequency Division Multiplexing

TIA	Transimpedance Amplifier
TIAs	Trans-Impedance Amplifiers
TOP	Transmitted Optical Power
TWDM	Time- and Wavelength-Division Multiplexing
TWFD	Time, wavelength and frequency (via subcarrier)-division multiplexing
UD	Ultra-Dense
UEs	User Entities
US	Upstream
VAEs	Variational Autoencoders
VHSP	Very-High Speed PON
VOA	Variable Optical Attenuator

Bibliography

- [29] A. Vaswani, N. Shazeer, N. Parmar, J. Uszkoreit, L. Jones, A. N. Gomez, Ł. Kaiser, and I. Polosukhin, “Attention is all you need,” *Advances in neural information processing systems*, vol. 30, 2017.
- [30] D. Richins, D. Doshi, M. Blackmore, A. T. Nair, N. Pathapati, A. Patel, B. Daguman, D. Dobrijalowski, R. Illikkal, K. Long *et al.*, “Ai tax: The hidden cost of ai data center applications,” *ACM Transactions on Computer Systems (TOCS)*, vol. 37, no. 1-4, pp. 1–32, 2021.
- [31] P. J. Winzer, D. T. Neilson, and A. R. Chraplyvy, “Fiber-optic transmission and networking: the previous 20 and the next 20 years,” *Optics express*, vol. 26, no. 18, pp. 24 190–24 239, 2018.
- [32] F. Effenberger and T. S. El-Bawab, “Passive optical networks (pons): past, present, and future,” *Optical Switching and Networking*, vol. 6, no. 3, pp. 143–150, 2009.
- [33] G. Kramer and G. Pesavento, “Ethernet passive optical network (epon): Building a next-generation optical access network,” *IEEE Communications magazine*, vol. 40, no. 2, pp. 66–73, 2002.
- [34] I. Sector and O. ITU, “Ont management and control interface specification for atm pon,” *Recommendation G*, vol. 983.2, 2002.
- [35] I. V. D. Voorde and G. V. D. Plas, “Full service optical access networks: Atm transport on passive optical networks,” *IEEE Communications Magazine*, vol. 35, no. 4, pp. 70–75, Apr 1997.

- [36] R. G. ITU-T, “Broadband optical access systems based on passive optical networks (pon),” *International Telecommunication Union*, vol. 983.1, 2005.
- [37] —, “Ont management and control interface specification for b-pon,” *International Telecommunication Union*, vol. 983.2, 2005.
- [38] —, “A broadband optical access system with increased service capability by wavelength allocation,” *International Telecommunication Union*, vol. 983.3, 2001.
- [39] —, “A broadband optical access system with increased service capability using dynamic bandwidth assignment,” *International Telecommunication Union*, vol. 983.4, 2001.
- [40] —, “A broadband optical access system with enhanced survivability,” *International Telecommunication Union*, vol. 983.5, 2002.
- [41] —, “10 gigabit-capable passive optical networks (xg-pon): General requirements,” *International Telecommunication Union*, vol. 987.1, 2010, 2016.
- [42] —, “10 gigabit-capable passive optical networks (xg-pon): Physical media dependent (pmd) layer specification,” *International Telecommunication Union*, vol. 987.2, 2010, 2016, 2023.
- [43] —, “10 gigabit-capable passive optical networks (xg-pon): Transmission convergence (tc) layer specification,” *International Telecommunication Union*, vol. 987.3, 2010.
- [44] —, “10-gigabit-capable passive optical networks (xg-pon) systems,” *International Telecommunication Union*, vol. 987.x, 2010-2016.
- [45] —, “10-gigabit-capable symmetric passive optical network (xgs-pon),” *International Telecommunication Union*, vol. 9807.1, 2016, 2020, 2023.

-
- [46] 25GS-PON-Multi-Source-Agreement-Group, “25gs-pon specification,” 2023, version 3.0, November 2023. Available at: <https://www.25gspon-msa.org/wp-content/uploads/2023/11/25GS-PON-Specification-V3.0.pdf>.
- [47] R. G. ITU-T, “Higher speed passive optical networks – requirements,” *International Telecommunication Union*, vol. 9804.1, 2019, 2021, 2024.
- [48] —, “Higher speed passive optical networks – common transmission convergence layer specification,” *International Telecommunication Union*, vol. 9804.2, 2021.
- [49] —, “50-gigabit-capable passive optical networks (50g-pon) - physical media dependent (pmd) layer specification,” *International Telecommunication Union*, vol. 9804.3, 2021, 2023.
- [50] —, “Higher speed passive optical networks (hsp) systems,” *International Telecommunication Union*, vol. 9804.x, 2019-2023.
- [51] C. F. Lam, *Passive optical networks: principles and practice*. Elsevier, 2011.
- [52] V. Houtsma, A. Mahadevan, N. Kaneda, and D. van Veen, “Transceiver technologies for passive optical networks: past, present, and future [invited tutorial],” *Journal of Optical Communications and Networking*, vol. 13, no. 1, pp. A44–A55, 2020.
- [53] M. S. Faruk, X. Li, D. Nasset, I. N. Cano, A. Rafel, and S. J. Savory, “Coherent passive optical networks: why, when, and how,” *IEEE Communications Magazine*, vol. 59, no. 12, pp. 112–117, 2022.
- [54] P. Torres-Ferrera, F. Effenberger, M. S. Faruk, S. J. Savory, and R. Gaudino, “Overview of high-speed tdm-pon beyond 50 gbps per wavelength using digital signal processing [invited tutorial],” *Journal of Optical Communications and Networking*, vol. 14, no. 12, pp. 982–996, 2022.

- [55] J. Montalvo, J. Torrijos, D. Cortes, R. Chundury, and M. S. Peter, "Journey toward software-defined passive optical networks with multi-pon technology: an industry view," *J. Opt. Commun. Netw.*, vol. 13, no. 8, pp. D22–D31, Aug 2021. [Online]. Available: <https://opg.optica.org/jocn/abstract.cfm?URI=jocn-13-8-D22>
- [56] C.-C. Sue, "Wavelength routing with spare reconfiguration for all-optical wdm networks," *Journal of lightwave technology*, vol. 23, no. 6, p. 1991, 2005.
- [57] X. Hu, X. Chen, Z. Zhang, and J. Bei, "Dynamic wavelength and bandwidth allocation in flexible twdm optical access network," *IEEE Communications Letters*, vol. 18, no. 12, pp. 2113–2116, 2014.
- [58] D. Lavery, S. Erkilinc, P. Bayvel, and R. I. Killey, "Recent progress and outlook for coherent pon," in *2018 Optical Fiber Communications Conference and Exposition (OFC)*. IEEE, 2018, pp. 1–3.
- [59] R. Bonk, E. Harstead, R. Borkowski, V. Houtsma, Y. Lefevre, A. Mahadevan, D. van Veen, M. Verplaetse, and S. Walklin, "Perspectives on and the road towards 100 gb/s tdm pon with intensity-modulation and direct-detection," *Journal of Optical Communications and Networking*, vol. 15, no. 8, pp. 518–526, 2023.
- [60] V. Houtsma and D. Van Veen, "Higher-speed pons based on data center technology and optics," *Journal of Optical Communications and Networking*, vol. 16, no. 2, pp. A98–A104, 2024.
- [61] H. P. Yuen and V. W. S. Chan, "Optical homodyne detection," *Optics Letters*, vol. 8, no. 3, pp. 177–179, 1983.
- [62] T. Okoshi, "Coherent optical fiber communication systems," *Proceedings of the IEEE*, vol. 75, no. 11, pp. 1419–1443, 1987.

- [63] M.-H. Shih, L. Wang, F. Choa, T. Tanbun-Ek, P. Wisk, W. Tsang, and C. Burrus, "Integrated coherent transceivers for broad-band access networks," *IEEE Photonics Technology Letters*, vol. 9, no. 11, pp. 1526–1528, 1997.
- [64] T. Kobayashi, J. Cho, M. Lamponi, G. De Valicourt, and C. R. Doerr, "Coherent optical transceivers scaling and integration challenges," *Proceedings of the IEEE*, vol. 110, no. 11, pp. 1679–1698, 2022.
- [65] L. G. Kazovsky, "Linewidth requirements for coherent optical communications," *Journal of Lightwave Technology*, vol. LT-4, no. 10, pp. 1023–1034, 1986.
- [66] R. Gaudino, V. Curri, G. Bosco, G. Rizzelli, A. Nespola, D. Zeolla, S. Straullu, S. Capriata, and P. Solina, "On the use of DFB lasers for coherent PON," in *Optical Fiber Communication Conference*. Optical Society of America, 2012, pp. OTh4G–1.
- [67] I. B. Kovacs, M. S. Faruk, P. Torres-Ferrera, and S. J. Savory, "Simplified coherent optical network units for very-high-speed passive optical networks," *Journal of Optical Communications and Networking*, vol. 16, no. 7, pp. C1–C10, 2024.
- [68] R. G. ITU-T, "989.2, 40-Gigabit-capable passive optical networks 2 (NG PON2): Physical media dependent (PMD) layer specification," *International Telecommunication Union*, <https://www.itu.int/rec/T-REC-G.989.2-201902-I/en>, 2019.
- [69] —, "989.1, 40-Gigabit-capable passive optical networks (NG-PON2): General requirements," *International Telecommunication Union*, <https://www.itu.int/rec/T-REC-G.989.1-201303-I/en>, 2013.
- [70] H. Rohde, E. Gottwald, S. Rosner, E. Weis, P. Wagner, Y. Babenko, D. Fritzsche, and H. Chaouch, "Trials of a coherent UDWDM PON over

- field-deployed fiber: Real-time LTE backhauling, legacy and 100G coexistence,” *Journal of Lightwave Technology*, vol. 33, no. 8, pp. 1644–1649, 2015.
- [71] H. Rohde, S. Smolorz, E. Gottwald, and K. Kloppe, “Next generation optical access: 1 gbit/s for everyone,” in *2009 35th European Conference on Optical Communication*. IEEE, 2009, pp. 1–3.
- [72] S. Narikawa, H. Sanjoh, and N. Sakurai, “Coherent wdm-pon using heterodyne detection with transmitter-side polarization diversity,” *IEICE Electronics Express*, vol. 7, no. 16, pp. 1195–1200, 2010.
- [73] F. Derr, “Coherent optical QPSK intradyne system: Concept and digital receiver realization,” *Journal of Lightwave Technology*, vol. 10, no. 9, pp. 1290–1296, 1992.
- [74] R. E. Epworth, “Balanced coherent receiver,” Jan. 5 1988, uS Patent 4,718,121.
- [75] T. Pfeiffer, P. Dom, S. Bidkar, F. Fredricx, K. Christodoulopoulos, and R. Bonk, “PON going beyond FTTH [invited tutorial],” *Journal of Optical Communications and Networking*, vol. 14, no. 1, pp. A31–A40, 2022.
- [76] J. S. Wey, “The outlook for PON standardization: a tutorial,” *Journal of Lightwave Technology*, vol. 38, no. 1, pp. 31–42, 2020.
- [77] R. Bonk, “The future of passive optical networks,” in *International Conference on Optical Network Design and Modeling (ONDM)*. IEEE, 2021, pp. 1–3.
- [78] B. C. Thomsen, R. Maher, D. S. Millar, and S. J. Savory, “Burst mode receiver for 112 Gb/s DP-QPSK with parallel DSP,” *Optics express*, vol. 19, no. 26, pp. B770–B776, 2011.

-
- [79] J. E. Simsarian, J. Gripp, S. Chandrasekhar, and P. Mitchell, “Fast-tuning coherent burst-mode receiver for metropolitan networks,” *IEEE Photonics Technology Letters*, vol. 26, no. 8, pp. 813–816, 2014.
- [80] S. Bidkar, T. Kale, J. Ho, J. Maes, R. Bonk, and T. Pfeiffer, “Demonstration of cooperative transport interface enabled cooperative DBA for 5G fronthaul over TDM-PON,” in *European Conference on Optical Communication (ECOC)*, 2023, pp. 503–506.
- [81] J. Maes, S. Bidkar, M. Straub, T. Pfeiffer, and R. Bonk, “Efficient transport of enhanced CPRI fronthaul over PON [invited],” *J. Opt. Commun. Netw.*, vol. 16, no. 2, pp. A136–A142, Feb 2024. [Online]. Available: <https://opg.optica.org/jocn/abstract.cfm?URI=jocn-16-2-A136>
- [82] *Gigabit-capable Passive Optical Networks (GPON): Physical media dependent (PMD) layer specification*, International Telecommunication Union Std. G.984.2, 2003.
- [83] *IEEE Standard for Information technology–Telecommunications and information exchange between systems–Local and metropolitan area networks–Specific requirements–Part 3: Carrier sense multiple access with collision detection (CSMA/CD) access method and physical layer specifications–Amendment: Ethernet in the First Mile (EFM)*, IEEE Std. 802.3ah-2004, 2004. [Online]. Available: <https://standards.ieee.org/ieee/802.3/3179/>
- [84] D. van Veen and V. Houtsma, “Strategies for economical next-generation 50G and 100G passive optical networks,” *Journal of Optical Communications and Networking*, vol. 12, no. 1, pp. A95–A103, 2020.
- [85] F. S. A. N. (FSAN), “Fsan roadmap,” 2016.

- [86] ITU-T, “G.sup.vhsp draft: Passive optical access system requirements and transmission technologies above 50 Gbit/s per wavelength,” *International Telecommunication Union*, <https://www.itu.int/md/T22-SG15-230417-TD-WP1-0118>, 2023.
- [87] J. Zhang and Z. Jia, “Coherent passive optical networks for 100g/λ-and-beyond fiber access: recent progress and outlook,” *IEEE network*, vol. 36, no. 2, pp. 116–123, 2022.
- [88] R. Koma, M. Fujiwara, J.-i. Kani, and T. Yoshida, “Fast feed-forward optical and electrical gain control to extend the dynamic range of the burst-mode digital coherent receiver for high-speed tdm-pon systems,” *Journal of Lightwave Technology*, vol. 40, no. 3, pp. 647–654, 2021.
- [89] R. Koma, M. Fujiwara, J. Kani, K. Suzuki, and A. Otaka, “Burst-mode digital signal processing that pre-calculates FIR filter coefficients for digital coherent PON upstream,” *IEEE/OSA Journal of Optical Communications and Networking*, vol. 10, no. 5, pp. 461–470, 2018.
- [90] R. K. Staubli and P. Gysel, “Crosstalk penalties due to coherent rayleigh noise in bidirectional optical communication systems,” *Journal of light-wave technology*, vol. 9, no. 3, pp. 375–380, 2002.
- [91] H. Rohde, E. Gottwald, A. Teixeira, J. D. Reis, A. Shahpari, K. Pulverer, and J. S. Wey, “Coherent ultra dense wdm technology for next generation optical metro and access networks,” *Journal of Lightwave Technology*, vol. 32, no. 10, pp. 2041–2052, 2014.
- [92] S. Shibita, D. Hisano, K. Maruta, Y. Nakayama, K. Mishina, and A. Maruta, “Optical reflection interference equalization for single-wavelength bidirectional wdm-pon transmission system,” *IEEE Photonics Journal*, vol. 13, no. 1, pp. 1–15, 2020.
- [93] V. Houtsma and D. van Veen, “Reusing data center optics and solutions for beyond 25gb/s PON: Is the gap really bridged?” in *Optical Fiber*

- Communication Conference (OFC)*, 2023, p. W1I.1. [Online]. Available: <https://opg.optica.org/abstract.cfm?URI=OFC-2023-W1I.1>
- [94] T. Verolet, A. Horth, H. Shoman, P. F. de la Horie, D. Dogaroiu, J. K. Jang, A. Lim, J. Naik, M. Teimourpour, K. Padmaraju *et al.*, “Athermally controlled iii-v/silicon c-band tunable lasers fabricated at scale,” in *ECOC 2024; 50th European Conference on Optical Communication*. VDE, 2024, pp. 611–614.
- [95] R. Bonk, “The future of passive optical networks,” in *2021 International Conference on Optical Network Design and Modeling (ONDM)*. IEEE, 2021, pp. 1–3.
- [96] P. Torres-Ferrera, F. Effenberger, M. S. Faruk, S. J. Savory, and R. Gaudino, “Overview of high-speed TDM-PON beyond 50 gbps per wavelength using digital signal processing [invited tutorial],” *Journal of Optical Communications and Networking*, vol. 14, no. 12, pp. 982–996, 2022.
- [97] I. Ogura, K. Kurata, and R. Pitwon, “Silicon photonics economic feasibility for automotive applications,” https://ieee802.org/3/cz/public/sep_2021/ogura_3cz_01_0921_SiPh_EconomicFeasibility.pdf, Sep. 2021, presented at IEEE 802.3cz Task Force Meeting.
- [98] CommScope, “Pon coexistence specification guide,” available at: <https://www.commscope.com/globalassets/digizuite/921585-995600.pdf>.
- [99] Corning-Optical-Communications, “Coexistence elements solutions guide,” available at: <https://www.corning.com/content/dam/corning/catalog/coc/documents/selection-guides/CRR-1836-AEN.pdf>.
- [100] X. Liu and F. Effenberger, “Emerging optical access network technologies for 5G wireless,” *IEEE/OSA Journal of Optical Communications and Networking*, vol. 8, no. 12, pp. B70–B79, 2016.

- [101] B. Skubic, J. Chen, J. Ahmed, L. Wosinska, and B. Mukherjee, "A comparison of dynamic bandwidth allocation for EPON, GPON, and next-generation TDM PON," *IEEE Communications Magazine*, vol. 47, no. 3, pp. S40–S48, 2009.
- [102] E. Harstead, D. van Veen, V. Houtsma, and P. Dom, "Technology roadmap for time-division multiplexed passive optical networks (TDM PONs)," *Journal of Lightwave Technology*, vol. 37, no. 2, pp. 657–664, 2018.
- [103] K. Hara, H. Nakamura, S. Kimura, M. Yoshino, S. Nishihara, S. Tamaki, J.-i. Kani, N. Yoshimoto, and H. Hadama, "Flexible load balancing technique using dynamic wavelength bandwidth allocation (DWBA) toward 100Gbit/s-class-WDM/TDM-PON," in *36th European Conference and Exhibition on Optical Communication (ECOC)*. Torino, Italy, September, 2010, paper Tu.3.B.2.
- [104] N. Suzuki, S. Yoshima, H. Miura, and K. Motoshima, "Demonstration of 100-Gb/s/ λ -based coherent WDM-PON system using new AGC EDFA based upstream preamplifier and optically superimposed AMCC function," *Journal of Lightwave Technology*, vol. 35, no. 8, pp. 1415–1421, 2016.
- [105] Y. Luo, X. Zhou, F. Effenberger, X. Yan, G. Peng, Y. Qian, and Y. Ma, "Time-and wavelength-division multiplexed passive optical network (TWDM-PON) for next-generation pon stage 2 (NG-PON2)," *Journal of lightwave technology*, vol. 31, no. 4, pp. 587–593, 2012.
- [106] D. Lavery, R. Maher, D. S. Millar, B. C. Thomsen, P. Bayvel, and S. J. Savory, "Digital coherent receivers for long-reach optical access networks," *Journal of Lightwave Technology*, vol. 31, no. 4, pp. 609–620, 2012.
- [107] M. S. Erkılınç, D. Lavery, K. Shi, B. C. Thomsen, P. Bayvel, R. I. Killey, and S. J. Savory, "Polarization-insensitive single-balanced photodiode coherent receiver for long-reach WDM-PONs," *Journal of Lightwave Technology*, vol. 34, no. 8, pp. 2034–2041, 2016.

- [108] S. J. Savory, M. S. Faruk, and X. Li, “Low complexity coherent for access networks,” in *Signal Processing in Photonic Communications*. Optical Society of America, 2020, pp. SpW1I–3.
- [109] Y. Zhu, L. Yi, B. Yang, X. Huang, J. S. Wey, Z. Ma, and W. Hu, “Comparative study of cost-effective coherent and direct detection schemes for 100 Gb/s/ λ PON,” *Journal of Optical Communications and Networking*, vol. 12, no. 9, pp. D36–D47, 2020.
- [110] M. S. Erkılınç, D. Lavery, K. Shi, B. C. Thomsen, R. I. Killey, S. J. Savory, and P. Bayvel, “Comparison of low complexity coherent receivers for UDWDM-PONs (λ -to-the-user),” *Journal of Lightwave Technology*, vol. 36, no. 16, pp. 3453–3464, 2018.
- [111] N. Iiyama, J.-i. Kani, K.-i. Suzuki, and A. Ootaka, “Advanced DSP for optical access networks: Challenges and opportunities,” in *2015 Optical Fiber Communications Conference and Exhibition (OFC)*. San Francisco, CA, USA, March, 2015, paper M3J.3.
- [112] N. Iiyama, M. Fujiwara, T. Kanai, J.-i. Kani, and J. Terada, “The approaches of coherent technology for TDM-PON,” in *2019 European Conference on Optical Communication (ECOC)*. Dublin, Ireland, September 2019, paper M.1.F.1.
- [113] J. Zhang, J. Yu, X. Li, K. Wang, W. Zhou, J. Xiao, L. Zhao, X. Pan, B. Liu, and X. Xin, “200 Gbit/s/ λ PDM-PAM-4 PON system based on intensity modulation and coherent detection,” *Journal of Optical Communications and Networking*, vol. 12, no. 1, pp. A1–A8, 2020.
- [114] M. Erkılınç, R. Emmerich, K. Habel, V. Jungnickel, C. Schmidt-Langhorst, C. Schubert, and R. Freund, “PON transceiver technologies for ≥ 50 Gbits/s per λ : Alamouti coding and heterodyne detection,” *Journal of Optical Communications and Networking*, vol. 12, no. 2, pp. A162–A170, 2020.

- [115] J. Zhang, Z. Jia, M. Xu, H. Zhang, L. A. Campos, and C. Knittle, “High-performance preamble design and upstream burst mode detection in 100-Gb/s/ λ TDM Coherent-PON,” in *2020 Optical Fiber Communications Conference (OFC)*. San-Diego, USA, March 2020, paper W1E.1.
- [116] D. van Veen and V. Houtsma, “Transceiver technologies for next-generation PON,” in *2020 Optical Fiber Communications Conference (OFC)*. San-Diego, USA, March 2020, paper W1E.2.
- [117] Q. Zhuge, “Cost-efficient architectures and signal processing for coherent PON systems,” in *2019 European Conference on Optical Communication (ECOC)*. Dublin, Ireland, September 2019.
- [118] S. Gudyriev, C. Kress, H. Zwickel, J. N. Kemal, S. Lischke, L. Zimmermann, C. Koos, and J. C. Scheytt, “Coherent ePIC receiver for 64 GBaud QPSK in 0.25 μ m photonic BiCMOS technology,” *Journal of Lightwave Technology*, vol. 37, no. 1, pp. 103–109, 2019.
- [119] S. Lange, N. Wolf, M. Gruner, L. Yan, R. Kaiser, K.-O. Velthaus, J. H. Choi, and M. Schell, “Low power InP-based monolithic DFB-laser IQ modulator with SiGe differential driver for 32-GBd QPSK modulation,” *Journal of lightwave technology*, vol. 34, no. 8, pp. 1678–1682, 2016.
- [120] M. S. Faruk and S. J. Savory, “Coherent access: Status and opportunities,” in *2020 IEEE Photonics Society Summer Topicals Meeting Series (SUM)*, 2020, pp. 1–2.
- [121] Y. Kotaki, S. Ogita, M. Matsude, Y. Kuwahara, and H. Ishikawa, “Tunable, narrow-linewidth and high-power lambda/4-shifted DFB laser,” *Electronics Letters*, vol. 25, no. 15, pp. 990–992, 1989.
- [122] G. Yoffe, S. Zou, S. Rishton, R. Olson, M. Emanuel, and B. Pezeshki, “Widely-tunable 30mW laser source with sub-500kHz linewidth using DFB array,” in *LEOS 2008-21st Annual Meeting of the IEEE Lasers and*

- Electro-Optics Society*. Newport Beach, CA, USA, November 2008, pp. 892–893.
- [123] V. Sales, J. Segarra, V. Polo, J. C. Velásquez, and J. Prat, “UDWDM-PON using low-cost coherent transceivers with limited tunability and heuristic DWA,” *IEEE/OSA Journal of Optical Communications and Networking*, vol. 8, no. 8, pp. 582–599, 2016.
- [124] D. Lavery, T. Gerard, S. Erkilingç, Z. Liu, L. Galdino, P. Bayvel, and R. I. Killey, “Opportunities for optical access network transceivers beyond OOK,” *IEEE/OSA Journal of Optical Communications and Networking*, vol. 11, no. 2, pp. A186–A195, 2019.
- [125] S. Sakano, T. Tsuchiya, M. Suzuki, S. Kitajima, and N. Chinone, “Tunable DFB laser with a striped thin-film heater,” *IEEE Photonics Technology Letters*, vol. 4, no. 4, pp. 321–323, 1992.
- [126] Z. Xu, Y. J. Wen, W.-D. Zhong, C.-J. Chae, X.-F. Cheng, Y. Wang, C. Lu, and J. Shankar, “High-speed WDM-PON using CW injection-locked fabry-pérot laser diodes,” *Optics express*, vol. 15, no. 6, pp. 2953–2962, 2007.
- [127] P. Healey, P. Townsend, C. Ford, L. Johnston, P. Townley, I. Lealman, L. Rivers, S. Perrin, and R. Moore, “Spectral slicing WDM-PON using wavelength-seeded reflective SOAs,” *Electronics Letters*, vol. 37, no. 19, pp. 1181–1182, 2001.
- [128] J. Simsarian and L. Zhang, “Wavelength locking a fast-switching tunable laser,” *IEEE Photonics Technology Letters*, vol. 16, no. 7, pp. 1745–1747, 2004.
- [129] X. Zeng, H. Ren, M. Fu, H. Jiang, L. Yi, W. Hu, and Q. Zhuge, “Frequency-offset-tolerant optical frequency comb-based coherent transmission for intra-datacenter interconnections,” *Optics Express*, vol. 29, no. 11, pp. 17 522–17 533, 2021.

- [130] M. Yamada, H. Ono, T. Kanamori, S. Sudo, and Y. Ohishi, "Broadband and gain-flattened amplifier composed of a 1.55 μm -band and a 1.58 μm -band Er³⁺-doped fibre amplifier in a parallel configuration," *Electronics letters*, vol. 33, no. 8, pp. 710–711, 1997.
- [131] S. Barton and Y. Al-Jalili, "A symbol timing recovery scheme based on spectral redundancy," in *IEE Colloquium on Advanced Modulation and Coding Techniques for Satellite Communications*. IET, 1992, pp. 3–1.
- [132] P. Matalla, M. S. Mahmud, C. Füllner, C. Koos, W. Freude, and S. Randel, "Hardware comparison of feed-forward clock recovery algorithms for optical communications," in *2021 Optical Fiber Communications Conference and Exhibition (OFC)*. IEEE, 2021, paper Th1A.10.
- [133] D. Godard, "Self-recovering equalization and carrier tracking in two-dimensional data communication systems," *IEEE transactions on communications*, vol. 28, no. 11, pp. 1867–1875, 1980.
- [134] S. J. Savory, "Digital filters for coherent optical receivers," *Optics express*, vol. 16, no. 2, pp. 804–817, 2008.
- [135] A. Viterbi, "Nonlinear estimation of PSK-modulated carrier phase with application to burst digital transmission," *IEEE Transactions on Information theory*, vol. 29, no. 4, pp. 543–551, 1983.
- [136] S. Song, K. Aizawa, and M. Hatori, "A blind adaptive array based on CMA and LMS," *Electronics and Communications in Japan (Part III: Fundamental Electronic Science)*, vol. 81, no. 7, pp. 37–44, 1998.
- [137] G.-H. Duan, A. Shen, A. Akrouf, F. Van Dijk, F. Lelarge, F. Pommereau, O. LeGouezigou, J.-G. Provost, H. Gariah, F. Blache *et al.*, "High performance InP-based quantum dash semiconductor mode-locked lasers for optical communications," *Bell Labs Technical Journal*, vol. 14, no. 3, pp. 63–84, 2009.

- [138] S. Tanaka, S.-H. Jeong, S. Sekiguchi, T. Kurahashi, Y. Tanaka, and K. Morito, “High-output-power, single-wavelength silicon hybrid laser using precise flip-chip bonding technology,” *Optics express*, vol. 20, no. 27, pp. 28 057–28 069, 2012.
- [139] B. Song, C. Stagarescu, S. Ristic, A. Behfar, and J. Klamkin, “3D integrated hybrid silicon laser,” *Optics Express*, vol. 24, no. 10, pp. 10 435–10 444, 2016.
- [140] P.-I. Dietrich, M. Blaicher, I. Reuter, M. Billah, T. Hoose, A. Hofmann, C. Caer, R. Dangel, B. Offrein, U. Troppenz *et al.*, “In situ 3D nanoprinting of free-form coupling elements for hybrid photonic integration,” *Nature Photonics*, vol. 12, no. 4, pp. 241–247, 2018.
- [141] B. Smith, I. Lyubomirsky, and S. Bhoja, “Leveraging 400g ZR FEC technology,” in *IEEE 802.3 Beyond 10 km Optical PHYs Study Group*, 2017. [Online]. Available: http://www.ieee802.org/3/B10K/public/17_11/lyubomirsky_b10k_01_1117.pdf
- [142] K. Grobe and J.-P. Elbers, “PON in adolescence: from TDMA to WDM-PON,” *IEEE Communications Magazine*, vol. 46, no. 1, pp. 26–34, 2008.
- [143] W.-p. ITU-T, “G.hsp.twdmpmd, Higher Speed Passive Optical Networks: TWDM PMD,” *International Telecommunication Union*, https://www.itu.int/ITU-T/workprog/wp_item.aspx?isn=18206, 2024.
- [144] R. G. ITU-T, “9804.1, Higher speed passive optical networks – Requirements,” *International Telecommunication Union*, <https://www.itu.int/rec/T-REC-G.9804.1-201911-I/en>, 2019.
- [145] S. Straullu, F. Forghieri, G. Bosco, V. Ferrero, and R. Gaudino, “Extended TWDM-PON demonstration up to 100 km and 35 dB ODN loss on burst-mode coherent reflective PON,” in *2014 Optical Fiber Communications Conference and Exhibition (OFC)*. San Francisco, CA, USA, March 2014, p. Tu2F.2.

- [146] L. Scholtz, D. Korček, L. Ladányi, and J. Müllerová, “Tunable thin film filters for the next generation PON stage 2 (NG-PON2),” in *2014 ELEKTRO*. IEEE, 2014, pp. 98–102.
- [147] N. Suzuki, H. Miura, K. Matsuda, R. Matsumoto, and K. Motoshima, “100 Gb/s to 1 Tb/s based coherent passive optical network technology,” *Journal of Lightwave Technology*, vol. 36, no. 8, pp. 1485–1491, 2018.
- [148] V. Houtsma, D. van Veen, and E. Harstead, “Recent progress on standardization of next-generation 25, 50, and 100G EPON,” *Journal of Lightwave Technology*, vol. 35, no. 6, pp. 1228–1234, 2016.
- [149] K. Matsuda and N. Suzuki, “Hardware-efficient signal processing technologies for coherent PON systems,” *Journal of Lightwave Technology*, vol. 37, no. 6, pp. 1614–1620, 2019.
- [150] N. Suzuki, S. Yoshima, H. Miura, and K. Motoshima, “Demonstration of 100-Gb/s/ λ -based coherent WDM-PON system using new AGC EDFA based upstream preamplifier and optically superimposed AMCC function,” *Journal of Lightwave Technology*, vol. 35, no. 8, pp. 1415–1421, 2016.
- [151] S. Straullu, J. Chang, G. Bosco, V. Ferrero, S. Abrate, F. Forghieri, and R. Gaudino, “TWDM-PON-compatible 10 Gbps burst-mode coherent reflective ONU achieving 31 dB ODN loss using DFB lasers,” in *2014 The European Conference on Optical Communication (ECOC)*. IEEE, 2014, pp. 1–3.
- [152] R. Urata, H. Liu, K. Yasumura, E. Mao, J. Berger, X. Zhou, C. Lam, R. Bannon, D. Hutchinson, D. Nelson *et al.*, “Mission apollo: Landing optical circuit switching at datacenter scale,” *arXiv preprint arXiv:2208.10041*, 2022.
- [153] M. Faugeron, M. Tran, O. Parillaud, M. Chtioui, Y. Robert, E. Vinet, A. Enard, J. Jacquet, and F. Van Dijk, “High-power tunable dilute mode

- DFB laser with low RIN and narrow linewidth,” *IEEE Photonics Technology Letters*, vol. 25, no. 1, pp. 7–10, 2013.
- [154] A. Schliesser, N. Picqué, and T. W. Hänsch, “Mid-infrared frequency combs,” *Nature photonics*, vol. 6, no. 7, pp. 440–449, 2012.
- [155] M. Zhang, B. Buscaino, C. Wang, A. Shams-Ansari, C. Reimer, R. Zhu, J. M. Kahn, and M. Lončar, “Broadband electro-optic frequency comb generation in a lithium niobate microring resonator,” *Nature*, vol. 568, no. 7752, pp. 373–377, 2019.
- [156] P. Del’Haye, A. Schliesser, O. Arcizet, T. Wilken, R. Holzwarth, and T. J. Kippenberg, “Optical frequency comb generation from a monolithic microresonator,” *Nature*, vol. 450, no. 7173, pp. 1214–1217, 2007.
- [157] G.-H. Duan, A. Shen, A. Akrout, F. Van Dijk, F. Lelarge, F. Pommereau, O. LeGouezigou, J.-G. Provost, H. Gariah, F. Blache *et al.*, “High performance InP-based quantum dash semiconductor mode-locked lasers for optical communications,” *Bell Labs Technical Journal*, vol. 14, no. 3, pp. 63–84, 2009.
- [158] J. N. Kemal, P. Marin-Palomo, M. Karpov, M. H. Anderson, W. Freude, T. J. Kippenberg, and C. Koos, “Chip-based frequency combs for wavelength-division multiplexing applications,” in *Optical Fiber Telecommunications VII*. Elsevier, 2020, pp. 51–102.
- [159] M. Seimetz, “Laser linewidth limitations for optical systems with high-order modulation employing feed forward digital carrier phase estimation,” in *Optical Fiber Communication Conference/National Fiber Optic Engineers Conference*, 2008, p. OTuM2. [Online]. Available: <http://opg.optica.org/abstract.cfm?URI=OFC-2008-OTuM2>
- [160] T. Schmidl and D. Cox, “Robust frequency and timing synchronization for OFDM,” *IEEE Transactions on Communications*, vol. 45, no. 12, pp. 1613–1621, 1997.

- [161] H. Minn, M. Zeng, and V. Bhargava, "On timing offset estimation for OFDM systems," *IEEE Communications Letters*, vol. 4, no. 7, pp. 242–244, 2000.
- [162] B. Park, H. Cheon, C. Kang, and D. Hong, "A novel timing estimation method for OFDM systems," *IEEE Communications Letters*, vol. 7, no. 5, pp. 239–241, 2003.
- [163] J. Zhang, Z. Jia, M. Xu, H. Zhang, and L. A. Campos, "Efficient preamble design and digital signal processing in upstream burst-mode detection of 100G TDM coherent-PON," *J. Opt. Commun. Netw.*, vol. 13, no. 2, pp. A135–A143, Feb 2021. [Online]. Available: <https://opg.optica.org/jocn/abstract.cfm?URI=jocn-13-2-A135>
- [164] M. Golay, "Complementary series," *IRE transactions on information theory*, vol. 7, no. 2, pp. 82–87, 1961.
- [165] ———, "Sieves for low autocorrelation binary sequences," *IEEE Transactions on Information Theory*, vol. 23, no. 1, pp. 43–51, 1977.
- [166] A. V. Tran, C. Zhu, C. C. Do, S. Chen, T. Anderson, D. Hewitt, and E. Skafidas, " 8×40 -Gb/s optical coherent Pol-Mux single carrier system with frequency domain equalization and training sequences," *IEEE Photonics Technology Letters*, vol. 24, no. 11, pp. 885–887, 2012.
- [167] C. Zhu, A. V. Tran, C. C. Do, S. Chen, T. Anderson, and E. Skafidas, "Digital signal processing for training-aided coherent optical single-carrier frequency-domain equalization systems," *Journal of Lightwave Technology*, vol. 32, no. 24, pp. 4712–4722, 2014.
- [168] M. Morelli and U. Mengali, "Feedforward frequency estimation for PSK: A tutorial review," *European Transactions on Telecommunications*, vol. 9, no. 2, pp. 103–116, 1998.
- [169] "IMT traffic estimates for the years 2020 to 2030," *Report ITU-R M.2370-0*, 2015.

-
- [170] W. Jiang, B. Han, M. A. Habibi, and H. D. Schotten, "The road towards 6G: A comprehensive survey," *IEEE Open Journal of the Communications Society*, vol. 2, pp. 334–366, 2021.
- [171] D. Bogdoll, P. Matalla, C. Füllner, C. Raack, S. Li, T. Käfer, S. Orf, M. R. Zofka, F. Sartoris, C. Schweikert *et al.*, "KIGLIS: Smart networks for smart cities," in *IEEE International Smart Cities Conference (ISC2)*. IEEE, 2021, pp. 1–4.
- [172] "Artificial Intelligence for the Optimization of Fiber Optic Networks in a Smart City, in German: Künstliche Intelligenz zur Optimierung von Glasfasernetzen in einer intelligenten Stadt," <https://www.forschung-it-sicherheit-kommunikationssysteme.de/projekte/kiglis>, 2020.
- [173] "Smart sustainable cities: An analysis of definitions," *ITU-T, FG-SSC*, 2015.
- [174] B. N. Silva, M. Khan, and K. Han, "Towards sustainable smart cities: A review of trends, architectures, components, and open challenges in smart cities," *Sustainable cities and society*, vol. 38, pp. 697–713, 2018.
- [175] P. J. Basford, F. M. J. Bulot, M. Apetroaie-Cristea, S. J. Cox, and S. J. Ossont, "LoRaWAN for smart city IoT deployments: A long term evaluation," *Sensors*, vol. 20, no. 3, 2020. [Online]. Available: <https://www.mdpi.com/1424-8220/20/3/648>
- [176] E. Harstead, "25G based PON technology," in *Optical Fiber Communication Conference (OFC)*. Optica Publishing Group, 2018, p. Tu2B.5. [Online]. Available: <https://opg.optica.org/abstract.cfm?URI=OFC-2018-Tu2B.5>
- [177] R. Borkowski, Y. Lefevre, A. Mahadevan, D. Van Veen, M. Straub, R. Kaptur, B. Czerwinski, B. Cornaglia, V. Houtsma, W. Coomans *et al.*, "FLCS-PON - an opportunistic 100 gbit/s flexible PON prototype with probabilistic shaping and soft-input FEC: operator trial and ODN case studies," *Journal*

- of Optical Communications and Networking*, vol. 14, no. 6, pp. C82–C91, 2022.
- [178] N. Dubrovina, E. Durán-Valdeiglesias, H. Debrégeas, R. Rosales, F. Lelarge, and R. Brenot, “Record high power 13dBm electro-absorption modulated laser for 50G-PON,” in *European Conference on Optical Communication (ECOC)*. IEEE, 2022, p. paper Th1E.6.
- [179] VPIphotonics GmbH, “<https://www.vpiphotonics.com>.”
- [180] B. Smith, I. Lyubomirsky, and S. Bhoja, “Leveraging 400G ZR FEC technology,” in *IEEE 802.3 Beyond 10 km Optical PHYs Study Group*, 2017. [Online]. Available: http://www.ieee802.org/3/B10K/public/17_11/lyubomirsky_b10k_01_1117.pdf
- [181] V. Lauinger, P. Matalla, J. Ney, N. Wehn, S. Randel, and L. Schmalen, “Fully-blind neural network based equalization for severe nonlinear distortions in 112 Gbit/s passive optical networks,” in *Optical Fiber Communications Conference (OFC)*, 2024, p. Th3J.5.
- [182] C. Shao, E. Giacomidis, S. Li, J. Li, M. Färber, T. Käfer, and A. Richter, “A novel machine learning-based equalizer for a downstream 100G PAM-4 PON,” in *Optical Fiber Communications Conference (OFC)*, 2024, p. W1H.1.
- [183] C. Shao, E. Giacomidis, P. Matalla, J. Li, S. Li, S. Randel, A. Richter, M. Färber, and T. Käfer, “Advanced equalization in 112 Gb/s upstream PON using a novel fourier convolution-based network,” in *European Conference on Optical Communication (ECOC)*, 2024, p. W3D.2.
- [184] R. Fischer, P. Matalla, S. Randel, and L. Schmalen, “Non-linear equalization in 112 Gb/s PONs using kolmogorov-arnold networks,” in *arXiv, eprint 2411.19631*, 2024. [Online]. Available: <https://arxiv.org/abs/2411.19631>

-
- [185] S. Miladić-Tešić, G. Marković, D. Peraković, and I. Cvitić, “A review of optical networking technologies supporting 5G communication infrastructure,” *Wireless Networks*, vol. 28, no. 1, pp. 459–467, 2022.
- [186] P. Matalla, M. S. Mahmud, C. Füllner, W. Freude, C. Koos, and S. Randel, “Real-time feedforward clock recovery for optical burst-mode transmission,” in *Optical Fiber Communication Conference (OFC)*, 2022, p. M2H.2. [Online]. Available: <https://opg.optica.org/abstract.cfm?URI=OFC-2022-M2H.2>
- [187] P. Matalla, C. Koos, and S. Randel, “Comparison of feedback and feed-forward clock recoveries for ultra-fast synchronization in passive optical networks,” in *Optical Fiber Communication Conference (OFC)*, 2024, p. W2A.36.
- [188] A. Hraghi, G. Rizzelli, A. Pagano, V. Ferrero, and R. Gaudino, “Analysis and experiments on C band 200G coherent PON based on alamouti polarization-insensitive receivers,” *Opt. Express*, vol. 30, no. 26, pp. 46 782–46 797, Dec 2022. [Online]. Available: <https://opg.optica.org/oe/abstract.cfm?URI=oe-30-26-46782>
- [189] I. B. Kovacs, M. S. Faruk, and S. J. Savory, “A minimal coherent receiver for 200 Gb/s/λ PON downstream with measured 29 dB power budget,” *IEEE Photonics Technology Letters*, vol. 35, no. 5, pp. 257–260, 2023.
- [190] A. Rashidinejad, A. Yekani, T. A. Eriksson, A. Napoli, R. Maher, A. Kakkar, V. Dominic, T. Duthel, M. Missey, P. Samra, D. Pavinski, P. Evans, W. Sande, M. Torbatian, C. Fludger, H. Sun, M. Ziari, F. Masoud, A. Somani, and D. Welch, “Real-time point-to-multipoint for coherent optical broadcast and aggregation – enabled by digital subcarrier multiplexing,” in *Optical Fiber Communication Conference (OFC)*, 2023, p. W3H.1. [Online]. Available: <https://opg.optica.org/abstract.cfm?URI=OFC-2023-W3H.1>

- [191] D. Zhang, D. Liu, X. Wu, and D. Nessim, “Progress of it-t higher speed passive optical network (50g-pon) standardization,” *J. Opt. Commun. Netw.*, vol. 12, no. 10, pp. D99–D108, Oct 2020.
- [192] Z. Xing, K. Zhang, X. Chen, Q. Feng, K. Zheng, Y. Zhao, Z. Dong, J. Zhou, T. Gui, Z. Ye, and L. Li, “First real-time demonstration of 200G TFDMA coherent PON using ultra-simple ONUs,” in *Optical Fiber Communication Conference (OFC)*, 2023, p. Th4C.4. [Online]. Available: <https://opg.optica.org/abstract.cfm?URI=OFC-2023-Th4C.4>
- [193] J. Zhang, G. Li, S. Xing, and N. Chi, “Flexible and adaptive coherent PON for next-generation optical access network,” *Optical Fiber Technology*, vol. 75, p. 103190, 2023.
- [194] J. Zhou, Z. Xing, H. Wang, K. Zhang, X. Chen, Q. Feng, K. Zheng, Y. Zhao, Z. Dong, T. Gui *et al.*, “Flexible coherent optical access: Architectures, algorithms, and demonstrations,” *Journal of Lightwave Technology*, 2024.
- [195] R. Borkowski, M. Straub, Y. Ou, Y. Lefevre, Ž. L. Jelić, W. Lanneer, N. Kaneda, A. Mahadevan, V. Hückstädt, D. van Veen *et al.*, “FLCS-PON—A 100 Gbit/s flexible passive optical network: Concepts and field trial,” *Journal of Lightwave Technology*, vol. 39, no. 16, pp. 5314–5324, 2021.
- [196] T. Hastie, R. Tibshirani, J. Friedman, T. Hastie, R. Tibshirani, and J. Friedman, “Random forests,” *The elements of statistical learning: Data mining, inference, and prediction*, pp. 587–604, 2009.
- [197] M. Straub, J. Reber, T. Saier, R. Borkowski, S. Li, D. Khomchenko, A. Richter, M. Farber, T. Kafer, and R. Bonk, “ML approaches for OTDR diagnoses in passive optical networks—event detection and classification: ways for ODN branch assignment,” *Journal of Optical Communications and Networking*, vol. 16, no. 7, pp. C43–C50, 2024.

-
- [198] W. M. P. van der Aalst, *Foundations of Process Discovery*. Cham: Springer International Publishing, 2022, pp. 37–75. [Online]. Available: https://doi.org/10.1007/978-3-031-08848-3_2
- [199] FTTH council Europe, “European FTTH/B market panorama 2024,” Sep. 2023.
- [200] atesio GmbH, “<http://www.atesio.de>.”
- [201] OpenStreetMap, “<https://www.openstreetmap.org>.”
- [202] M. Gontscharow, J. Doll, A. Schotschneider, D. Bogdoll, S. Orf, J. Jestram, M. R. Zofka, and J. Marius Zollner, “Scalable remote operation for autonomous vehicles: Integration of cooperative perception and open source communication,” in *IEEE Intelligent Vehicles Symposium (IV)*, 2024, pp. 43–50.
- [203] D. Bogdoll, J. Jestram, J. Rauch, C. Scheib, M. Wittig, and J. M. Zöllner, “Compressing sensor data for remote assistance of autonomous vehicles using deep generative models,” in *Conference on Neural Information Processing Systems Workshop on Machine Learning for Autonomous Driving (NeurIPS)*, 2021, p. ML4AD.
- [204] D. Welch, A. Napoli, J. Bäck, S. Buggaveeti, C. Castro, A. Chase, X. Chen, V. Dominic, T. Duthel, T. A. Eriksson *et al.*, “Digital subcarrier multiplexing: Enabling software-configurable optical networks,” *Journal of Lightwave Technology*, vol. 41, no. 4, pp. 1175–1191, 2023.
- [205] A. Banerjee, Y. Park, F. Clarke, H. Song, S. Yang, G. Kramer, K. Kim, and B. Mukherjee, “Wavelength-division-multiplexed passive optical network (WDM-PON) technologies for broadband access: a review,” *Journal of optical networking*, vol. 4, no. 11, pp. 737–758, 2005.
- [206] V. Houtsma and D. van Veen, “Optical strategies for economical next generation 50 and 100G PON,” in *Optical Fiber Communication Conference*. Optical Society of America, 2019, pp. M2B–1.

- [207] K. Matsuda, R. Matsumoto, and N. Suzuki, “Hardware-efficient adaptive equalization and carrier phase recovery for 100-Gb/s/ λ -based coherent WDM-PON systems,” *Journal of Lightwave Technology*, vol. 36, no. 8, pp. 1492–1497, 2017.
- [208] D. Lavery, M. Ionescu, S. Makovejs, E. Torrenco, and S. J. Savory, “A long-reach ultra-dense 10 Gbit/s WDM-PON using a digital coherent receiver,” *Optics express*, vol. 18, no. 25, pp. 25 855–25 860, 2010.
- [209] D. van Veen and V. Houtsma, “50 Gbps low complex burst mode coherent detection for time-division multiplexed passive optical networks,” in *2018 European Conference on Optical Communication (ECOC)*. Rome, Italy, September 2018, paper Tu1B.2.
- [210] Y. Zhu, B. Yang, Y. Zhong, Z. Liu, Y. Guo, J. S. Wey, X. Huang, and Z. Ma, “Performance comparison of coherent and direct detection schemes for 50G PON,” in *2020 Optical Fiber Communications Conference (OFC)*. San-Diego, USA, March 2020, paper W1E.3.
- [211] T. L. Koch and U. Koren, “Semiconductor lasers for coherent optical fiber communications,” *Journal of lightwave technology*, vol. 8, no. 3, pp. 274–293, 1990.
- [212] R. Maher, D. S. Millar, S. J. Savory, and B. C. Thomsen, “Widely tunable burst mode digital coherent receiver with fast reconfiguration time for 112 Gb/s DP-QPSK WDM networks,” *Journal of lightwave technology*, vol. 30, no. 24, pp. 3924–3930, 2012.
- [213] D. Godard, “Passband timing recovery in an all-digital modem receiver,” *IEEE Transactions on Communications*, vol. 26, no. 5, pp. 517–523, 1978.
- [214] M. Yan, Z. Tao, L. Dou, L. Li, Y. Zhao, T. Hoshida, and J. C. Rasmussen, “Digital clock recovery algorithm for nyquist signal,” in *2013 Conference on Optical Fiber Communication (OFC)*. Anaheim, CA, USA, March 2013, paper OTu2I.7.

- [215] A. Benveniste and M. Goursat, "Blind equalizers," *IEEE Transactions on communications*, vol. 32, no. 8, pp. 871–883, 1984.
- [216] F. Lelarge, B. Dagens, J. Renaudier, R. Brenot, A. Accard, F. van Dijk, D. Make, O. Le Gouezigou, J.-G. Provost, F. Poingt *et al.*, "Recent advances on InAs/InP quantum dash based semiconductor lasers and optical amplifiers operating at $1.55\mu\text{m}$," *IEEE Journal of Selected Topics in Quantum Electronics*, vol. 13, no. 1, pp. 111–124, 2007.
- [217] K. Merghem, C. Calò, R. Rosales, X. Lafosse, G. Aubin, A. Martinez, F. Lelarge, and A. Ramdane, "Stability of optical frequency comb generated with InAs/InP Quantum-Dash-Based Passive Mode-Locked Lasers," *IEEE Journal of Quantum Electronics*, vol. 50, no. 4, pp. 275–280, 2014.
- [218] M. S. Erkiling, D. Lavery, P. Bayvel, R. I. Killey, S. J. Savory, and C. Schubert, "Coherent ONU designs for 50 Gb/s/ λ PON," in *2019 Optical Fiber Communications Conference and Exhibition (OFC)*, 2019, pp. 1–3.
- [219] T.-P. Lee, C. E. Zah, R. Bhat, W. Young, B. Pathak, F. Favire, P. S. Lin, N. Andreadakis, C. Caneau, A. W. Rahjel *et al.*, "Multiwavelength DFB laser array transmitters for ONTC reconfigurable optical network testbed," *Journal of lightwave technology*, vol. 14, no. 6, pp. 967–976, 1996.
- [220] C. Calò, V. Vujicic, R. Watts, C. Browning, K. Merghem, V. Panapakkam, F. Lelarge, A. Martinez, B.-E. Benkelfat, A. Ramdane *et al.*, "Single-section quantum well mode-locked laser for 400 Gb/s SSB-OFDM transmission," *Optics express*, vol. 23, no. 20, pp. 26 442–26 449, 2015.
- [221] N. Kaneda, D. van Veen, A. Mahadevan, and V. Houtsma, "DSP for 50g/100G hybrid modulated TDM-PON," in *2020 European Conference on Optical Communications (ECOC)*. IEEE, 2020, pp. 1–4.
- [222] J. Buus and E. J. Murphy, "Tunable lasers in optical networks," *Journal of Lightwave Technology*, vol. 24, no. 1, pp. 5–11, 2006.

- [223] “Higher speed passive optical networks: requirements,” *ITU-T Recommendation G.9804.1*, 2019. [Online]. Available: <https://www.itu.int/rec/T-REC^G.9804.1-201911-I/en>
- [224] D. Lee, “C-band wavelength plan for 10g epon downstream,” *IEEE 802.3av 10Gb/s EPON TF Atlanta, Georgia USA*, 2007. [Online]. Available: <https://www.itu.int/rec/T-REC^G.9804.1-201911-I/en>
- [225] R. Nagarajan, I. Lyubomirsky, and O. Agazzi, “Low power dsp-based transceivers for data center optical fiber communications (invited tutorial),” *Journal of Lightwave Technology*, vol. 39, no. 16, pp. 5221–5231, 2021.
- [226] D. Bogdoll, P. Matalla, C. Füllner, C. Raack, S. Li, T. Käfer, S. Orf, M. R. Zofka, F. Sartoris, C. Schweikert, T. Pfeiffer, A. Richter, S. Randel, and R. Bonk, “Kiglis: Smart networks for smart cities,” in *2021 IEEE International Smart Cities Conference (ISC2)*. Manchester, United Kingdom, October 2021.
- [227] L. G. Kazovsky, W.-T. Shaw, D. Gutierrez, N. Cheng, and S.-W. Wong, “Next-generation optical access networks,” *Journal of lightwave technology*, vol. 25, no. 11, pp. 3428–3442, 2007.
- [228] D. Welch, A. Napoli, J. Bäck, W. Sande, J. Pedro, F. Masoud, C. Fludger, T. Duthel, H. Sun, S. J. Hand, T.-K. Chiang, A. Chase, A. Mathur, T. A. Eriksson, M. Plantare, M. Olson, S. Voll, and K.-T. Wu, “Point-to-multipoint optical networks using coherent digital subcarriers,” *Journal of Lightwave Technology*, vol. 39, no. 16, pp. 5232–5247, 2021.
- [229] D. Nessel, “NG-PON2 technology and standards,” *Journal of Lightwave Technology*, vol. 33, no. 5, pp. 1136–1143, 2015.
- [230] M. Magarini, L. Barletta, A. Spalvieri, F. Vacondio, T. Pfau, M. Pepe, M. Bertolini, and G. Gavioli, “Pilot-symbols-aided carrier-phase recovery for 100-G PM-QPSK digital coherent receivers,” *IEEE Photonics Technology Letters*, vol. 24, no. 9, pp. 739–741, 2012.

-
- [231] S. Straullu, F. Forghieri, G. Bosco, V. Ferrero, and R. Gaudino, “Compatibility between coherent reflective burst-mode PON and TWDM-PON physical layers,” *Optics Express*, vol. 22, no. 1, pp. 9–14, 2014.
- [232] C. Zhang, S. Liang, H. Zhu, and W. Wang, “Tunable dfb lasers integrated with ti thin film heaters fabricated with a simple procedure,” *Optics & Laser Technology*, vol. 54, pp. 148–150, 2013.
- [233] D. Chitimalla, K. Kondepudi, L. Valcarengi, M. Tornatore, and B. Mukherjee, “5g fronthaul–latency and jitter studies of cpri over ethernet,” *J. Opt. Commun. Netw.*, vol. 9, no. 2, pp. 172–182, Feb 2017. [Online]. Available: <http://jocn.osa.org/abstract.cfm?URI=jocn-9-2-172>
- [234] Y.-H. Wen, J.-W. Ho, and K.-M. Feng, “Simultaneous all-optical transparent phase multiplexing/de-multiplexing based on fwm in a hnlf,” in *Optical Fiber Communication Conference*. Optica, 2022, p. W4D.1. [Online]. Available: <http://www.opg.optica.org/abstract.cfm?URI=OFC-2016-W4D.1>
- [235] FTTH council Europe, “European FTTH/B market panorama 2021,” May 2021.